

České vysoké učení technické v Praze  
Fakulta jaderná a fyzikálně inženýrská

Katedra fyziky  
Obor: Experimentální jaderná a částicová fyzika



Studium produkce mezonu D ve  
srážkách  $Au+Au$  200 GeV na  
experimentu STAR

DIPLOMOVÁ PRÁCE

Vypracoval: Bc. Robert Líčeník  
Vedoucí práce: Mgr. Jaroslav Bielčík, Ph.D.  
Konzultant: Ing. Lukáš Kramárik  
Rok: 2019

Czech Technical University in Prague  
Faculty of Nuclear Sciences and Physical Engineering

Department of Physics  
Specialization: Experimental Nuclear and Particle Physics



Study of D meson production in 200  
GeV Au+Au collisions at the STAR  
experiment

MASTER'S THESIS

Author: Bc. Robert Líčeník  
Supervisor: Mgr. Jaroslav Bielčík, Ph.D.  
Consultant: Ing. Lukáš Kramárik  
Year: 2019

Před svázáním místo téhle stránky 

vložíte zadání práce
----------------------

 s podpisem děkana (bude to jediný oboustranný list ve Vaší práci) !!!!



## **Prohlášení**

Prohlašuji, že jsem svou diplomovou práci vypracoval samostatně a použil jsem pouze podklady (literaturu, projekty, SW atd.) uvedené v příloženém seznamu.

Nemám závažný důvod proti použití tohoto školního díla ve smyslu § 60 Zákona č. 121/2000 Sb., o právech souvisejících s právem autorským a o změně některých zákonů (autorský zákon).

V Praze dne .....

.....  
Bc. Robert Líčeník

## **Acknowledgments**

I would like to thank the supervisor of my thesis, Dr. Jaroslav Bielčík, for his guidance throughout the course of this work. I would also like to thank Ing. Lukáš Kramárik, Ing. Jan Vaněk and other colleagues who have helped me with the completion of this thesis by providing valuable advice and comments.

Bc. Robert Líčeník

*Název práce:*

**Studium produkce mezonu D ve srážkách Au+Au 200 GeV na experimentu STAR**

*Autor:* Bc. Robert Líčeník

*Obor:* Experimentální jaderná a částicová fyzika

*Druh práce:* Diplomová práce

*Vedoucí práce:* Mgr. Jaroslav Bielčík, Ph.D.  
Katedra fyziky,  
Fakulta jaderná a fyzikálně inženýrská,  
České vysoké učení technické v Praze

*Konzultant:* Ing. Lukáš Kramárik  
Katedra fyziky,  
Fakulta jaderná a fyzikálně inženýrská,  
České vysoké učení technické v Praze

*Abstrakt:* Hlavním cílem této práce je studium produkce půvabných mezonů ve vysokoenergetických srážkách těžkých iontů, během nichž vzniká kvark-gluonové plazma. Půvabné mezony jsou vytvářeny na počátku srážky, procházejí celým vývojem systému a slouží jako sonda ke zjišťování vlastností vzniklého média. Detektor Heavy Flavor Tracker na experimentu STAR umožnil díky svému vynikajícímu rozlišení rekonstruovat sekundární vrcholy srážky z rozpadů půvabných mezonů. V jádro-jaderných srážkách dochází k potlačení produkce D mezonů,  $R_{AA} \leq 0.5$  pro částice s  $p_T > 4.5$  GeV/c v centralitě 0-10 %, v důsledku ztráty energie v kvark-gluonovém plazmatu. Signifikanci signálu mezonu  $D^\pm$  lze výrazně zvýšit, z 4.0 na 19.8 pro částice s  $2.0 < p_T < 2.5$  GeV/c v centralitě 0-10 %, aplikací metod strojového učení. S jejich pomocí můžeme lépe rozlišovat mezi signálem a pozadím a otevírají nám tedy prostor pro analýzu v oblasti nízkých příčných hybností.

*Klíčová slova:* půvabné mezony, srážky těžkých iontů, kvark-gluonové plazma, experiment STAR

*Title:*

**Study of D meson production in 200 GeV Au+Au collisions at the STAR experiment**

*Author:* Bc. Robert Líčeník

*Specialization:* Experimental Nuclear and Particle Physics

*Sort of Thesis:* Master's Thesis

*Supervisor:* Mgr. Jaroslav Bielčík, Ph.D.  
Department of Physics,  
Faculty of Nuclear Sciences and Physical Engineering,  
Czech Technical University in Prague

*Consultant:* Ing. Lukáš Kramárik  
Department of Physics,  
Faculty of Nuclear Sciences and Physical Engineering,  
Czech Technical University in Prague

*Abstract:* The main topic of this thesis is the production of charmed mesons in high-energy heavy-ion collisions, during which the Quark-Gluon Plasma is formed. Charmed mesons are created at the beginning of the collisions, experience the entire evolution of the system and serve as a probe inside the medium. Heavy Flavor Tracker at STAR allowed the reconstruction of secondary vertices from charmed-meson decays, thanks to its excellent resolution. The D meson production is significantly suppressed in nucleus-nucleus collisions,  $R_{AA} \leq 0.5$  for particles with  $p_T > 4.5$  GeV/c in 0-10 % centrality, as a consequence of energy loss inside the Quark-Gluon Plasma.  $D^\pm$  signal significance can be substantially improved, from 4.0 to 19.8 for particles with  $2.0 < p_T < 2.5$  GeV/c in 0-10 % centrality, by applying machine-learning techniques. They increase our signal and background distinction capabilities and open the door for analysis in the low- $p_T$  region.

*Key words:* charmed mesons, heavy-ion collisions, Quark-Gluon Plasma, STAR experiment

# Contents

<b>Introduction</b>	<b>16</b>
<b>1 Physics of Heavy-Ion Collisions</b>	<b>18</b>
1.1 QCD Phase Diagram . . . . .	18
1.2 Variables in Heavy-Ion Collisions . . . . .	20
1.2.1 Spatial Coordinates . . . . .	20
1.2.2 Transverse Momentum . . . . .	20
1.2.3 Rapidity . . . . .	20
1.2.4 Pseudorapidity . . . . .	21
1.3 Collision Centrality . . . . .	21
1.4 Collision Space-Time Evolution . . . . .	22
1.5 Quark-Gluon Plasma . . . . .	23
1.5.1 Parton Energy Loss . . . . .	26
1.5.2 Nuclear Modification Factor . . . . .	27
1.5.3 Jet Quenching . . . . .	29
1.5.4 Quarkonia Production Suppression . . . . .	30
1.5.5 Flow . . . . .	31
<b>2 Recent RHIC and LHC Results</b>	<b>34</b>
2.1 D Mesons in p+p Collisions . . . . .	34
2.2 D Mesons in p+A Collisions . . . . .	37
2.3 D Mesons in A+A Collisions . . . . .	37
<b>3 STAR Experiment</b>	<b>46</b>
3.1 BNL Accelerator Complex . . . . .	46
3.1.1 Pre-Accelerators . . . . .	46

3.1.2	RHIC . . . . .	47
3.1.3	RHIC Future Plans . . . . .	49
3.2	STAR Detector . . . . .	50
3.2.1	Time-Projection Chamber . . . . .	51
3.2.2	Time-of-Flight Detector . . . . .	52
3.2.3	Barrel Electromagnetic Calorimeter . . . . .	53
3.2.4	Vertex Position Detector . . . . .	55
3.2.5	Heavy Flavor Tracker . . . . .	56
3.2.6	Recent and Planned Upgrades . . . . .	60
<b>4</b>	<b>Reconstruction of Charmed Mesons in Heavy-Ion Collisions</b>	<b>62</b>
4.1	Dataset . . . . .	62
4.2	Candidates Selection . . . . .	63
4.3	Raw Yield Extraction . . . . .	65
<b>5</b>	<b>Yield Correction &amp; Results</b>	<b>71</b>
5.1	Detector Acceptance×Efficiency . . . . .	71
5.2	Transverse Momentum Correction . . . . .	73
5.3	Systematic Errors . . . . .	74
5.4	D <sup>±</sup> Spectra . . . . .	76
5.5	D <sup>±</sup> Nuclear Modification Factor . . . . .	81
<b>6</b>	<b>Application of Machine-Learning Techniques</b>	<b>84</b>
6.1	Machine Learning in High-Energy Physics . . . . .	84
6.2	Reconstruction of D <sup>±</sup> Meson Using TMVA . . . . .	86
6.2.1	BDT Training . . . . .	86
6.2.2	BDT Application and Results . . . . .	88
	<b>Summary</b>	<b>94</b>
	<b>References</b>	<b>96</b>
	<b>Appendices</b>	<b>103</b>
<b>A</b>	<b>Variables Distributions</b>	<b>104</b>



# List of Figures

1.1	QCD phase diagram . . . . .	19
1.2	Nucleus-nucleus collision illustration . . . . .	22
1.3	ALICE centrality measurement . . . . .	23
1.4	Heavy-ion collision time evolution . . . . .	24
1.5	Strong coupling constant dependence on momentum . . . . .	25
1.6	Bethe-Bloch formula for muon . . . . .	26
1.7	Energy loss of several identified particle speices in the QGP . . . . .	28
1.8	STAR jet quenching measurement . . . . .	29
1.9	STAR $J/\psi$ suppression measurement . . . . .	30
1.10	Directed flow at STAR . . . . .	32
1.11	Collision zone, initial anisotropy and flow development in the collision .	33
1.12	STAR $v_2$ and $v_3$ . . . . .	33
2.1	$D^0$ in p+p collisions at STAR . . . . .	35
2.2	ALICE results of $D^0$ and $D^+$ cross-section in p+p . . . . .	36
2.3	ATLAS results of $D^\pm$ cross-section in p+p . . . . .	36
2.4	CMS $D^0$ in p+p . . . . .	37
2.5	ALICE D meson results in p+Pb . . . . .	38
2.6	ATLAS results of $D^0$ meson in p+Pb . . . . .	39
2.7	STAR $R_{AA}$ results in 2016 data . . . . .	39
2.8	STAR $D^0$ $R_{AA}$ and $R_{CP}$ . . . . .	40
2.9	ALICE $R_{AA}$ for centralities 0-10 and 30-50 % . . . . .	41
2.10	CMS $D^0$ in Pb+Pb . . . . .	42
2.11	$D^0$ directed flow . . . . .	43
2.12	STAR elliptic flow mesurement . . . . .	43

2.13	STAR triangular flow measurement . . . . .	44
2.14	ALICE D meson elliptic flow . . . . .	44
2.15	D <sup>0</sup> flow in CMS Pb+Pb . . . . .	45
3.1	BNL accelerator complex . . . . .	47
3.2	RF cavity . . . . .	48
3.3	RHIC nucleon pair luminosity for various systems . . . . .	49
3.4	STAR experiment schematic view . . . . .	51
3.5	STAR TPC energy loss measurement . . . . .	52
3.6	STAR TPC schematic view . . . . .	53
3.7	STAR event example . . . . .	54
3.8	STAR TOF detector module . . . . .	54
3.9	STAR TOF detector performance . . . . .	55
3.10	STAR BEMC illustration . . . . .	56
3.11	STAR BEMC module . . . . .	57
3.12	STAR VPD assembly . . . . .	57
3.13	STAR HFT schematic view . . . . .	58
3.14	STAR HFT PXL . . . . .	58
3.15	STAR HFT IST . . . . .	59
3.16	STAR HFT SSD . . . . .	59
3.17	STAR HFT resolution . . . . .	60
4.1	Event cuts . . . . .	63
4.2	Three-body D <sup>±</sup> decay illustration . . . . .	65
4.3	Raw Yield extraction . . . . .	67
4.4	D <sup>±</sup> mass obtained from fit . . . . .	69
4.5	D <sup>±</sup> mass resolution . . . . .	69
5.1	Efficiency simulation points . . . . .	73
5.2	Levy fit $p_T$ points correction . . . . .	75
5.3	D <sup>±</sup> spectrum, 0-10 % . . . . .	77
5.4	D <sup>±</sup> spectrum, 10-40 % . . . . .	78
5.5	D <sup>±</sup> spectrum, 40-80 % . . . . .	79

5.6	D <sup>±</sup> spectrum, 0-80 % . . . . .	80
5.7	D <sup>±</sup> R <sub>AA</sub> , 0-10 % . . . . .	82
5.8	D <sup>±</sup> R <sub>AA</sub> , 10-40 % . . . . .	82
5.9	D <sup>±</sup> R <sub>AA</sub> , 40-80 % . . . . .	83
6.1	Decision tree . . . . .	85
6.2	Distributions of training variables . . . . .	87
6.3	Correlation matrix for signal and background . . . . .	88
6.4	BDT overtraining check . . . . .	89
6.5	Significance vs. BDT response, different S:B ratios . . . . .	90
6.6	Significance vs. BDT response, 2.0 < p <sub>T</sub> < 2.5 GeV/c, 0-10 % . . . . .	91
6.7	BDT consistency check . . . . .	92
6.8	Invariant mass - rectangular vs. BDT . . . . .	92
6.9	Significance comparison - rectangular vs. BDT . . . . .	93
A.1	Daughter particles pseudorapidity distribution and cut . . . . .	105
A.2	Daughter particles transverse momentum distribution and cut . . . . .	106
A.3	Daughter particles TPC energy loss deviation distribution and cut . . . . .	107
A.4	Daughter particles ToF inverse velocity distribution and cut . . . . .	108
A.5	Daughter pairs maximum DCA distribution and cut . . . . .	109
A.6	D <sup>±</sup> meson decay length distribution and cut . . . . .	109
A.7	Vertex triangle longest side distribution and cut . . . . .	110
A.8	Cosine of the pointing angle with cut . . . . .	110
A.9	Daughter particles DCA to primary vertex distribution and cut . . . . .	111
B.1	Invariant mass before and after background subtraction, 0-80 %, p <sub>T</sub> bins: 1-2, 2-2.5, 2.5-3 and 3-3.5 GeV/c . . . . .	113
B.2	Invariant mass before and after background subtraction, 0-80 %, p <sub>T</sub> bins: 3.5-4, 4-4.5, 4.5-5 and 5-5.5 GeV/c . . . . .	114
B.3	Invariant mass before and after background subtraction, 0-80 %, p <sub>T</sub> bins: 5.5-6, 6-7, 7-8 and 8-10 GeV/c . . . . .	115
B.4	Invariant mass before and after background subtraction, 0-10 %, p <sub>T</sub> bins: 1-2, 2-2.5, 2.5-3 and 3-3.5 GeV/c . . . . .	116
B.5	Invariant mass before and after background subtraction, 0-10 %, p <sub>T</sub> bins: 3.5-4, 4-4.5, 4.5-5 and 5-5.5 GeV/c . . . . .	117

B.6	Invariant mass before and after background subtraction, 0-10 %, $p_T$ bins: 5.5-6, 6-7, 7-8 and 8-10 GeV/ $c$ . . . . .	118
B.7	Invariant mass before and after background subtraction, 10-40 %, $p_T$ bins: 1-2, 2-2.5, 2.5-3 and 3-3.5 GeV/ $c$ . . . . .	119
B.8	Invariant mass before and after background subtraction, 10-40 %, $p_T$ bins: 3.5-4, 4-4.5, 4.5-5 and 5-5.5 GeV/ $c$ . . . . .	120
B.9	Invariant mass before and after background subtraction, 10-40 %, $p_T$ bins: 5.5-6, 6-7, 7-8 and 8-10 GeV/ $c$ . . . . .	121
B.10	Invariant mass before and after background subtraction, 40-80 %, $p_T$ bins: 1-2, 2-2.5, 2.5-3 and 3-3.5 GeV/ $c$ . . . . .	122
B.11	Invariant mass before and after background subtraction, 40-80 %, $p_T$ bins: 3.5-4, 4-4.5, 4.5-5 and 5-5.5 GeV/ $c$ . . . . .	123
B.12	Invariant mass before and after background subtraction, 40-80 %, $p_T$ bins: 5.5-6, 6-7, 7-8 and 8-10 GeV/ $c$ . . . . .	124

# Introduction

At the very beginning of the Universe, about one microsecond after the Big Bang, the Universe was extremely hot, dense and rapidly expanding. It could be described as a "soup" of quasi-free quarks and gluons that we call the Quark-Gluon Plasma (QGP). This exotic state of matter is very interesting because of its extreme nature and we naturally want to learn as much as possible about it. However, the Universe is much cooler today and we are not aware of any place where we could observe the QGP directly (except maybe the very centers of massive neutron stars). Fortunately, we found a way to recreate these rather extreme conditions. When we accelerate heavy atomic nuclei to large kinetic energies (100 GeV per nucleon at the Relativistic Heavy Ion Collider (RHIC) and 2.51 TeV per nucleon at the Large Hadron Collider (LHC)) and then collide them head-on, we fill a tiny space with large amounts of energy and thus achieve the phase transition. There are hundreds of particles and antiparticles created during each heavy-ion collision. In general we would like to detect and analyze all of those particles. However, since this is practically impossible, we are often interested only in particular rare physical processes. In order to detect them, we use large and complex particle detectors, such as the STAR (Solenoidal Tracker At RHIC) experiment, which is composed of many sub-detectors and has a great ability to distinguish among different particle species and to trace them back to the point of their origin. One of the most interesting ones are charmed mesons. They are created during the fragmentation of the charm quarks, which are created during the first moments after ultrarelativistic heavy-ion collisions and can serve as a probe inside the QGP. Because they are formed during the hard part of the collision (before the QGP forms), they experience the entire evolution of the system and provide us with valuable information about the interaction of heavy quarks within the QGP. Many charmed mesons have been observed, but the most frequently occurring are the neutral  $D^0$ , the charged  $D^\pm$ , the strange  $D_s^\pm$  and excited states  $D^*$ . The production of  $D^\pm$  in heavy-ion collisions is the main topic of this work. It is the second lightest particle containing the c quark and decays only via the weak interaction which results in a relatively long mean lifetime ( $\tau \simeq 1.040 \pm 0.007 \cdot 10^{-12}$  s) with corresponding mean decay length  $\lambda = c\tau = 312 \pm 2$   $\mu\text{m}$ . The most experimentally intriguing decay channel is the  $D^\pm \rightarrow K^\mp \pi^\pm \pi^\pm$ , because it is a fully hadronic decay channel with the highest branching ratio of  $(8.98 \pm 0.28)$  % (all values from [1]).

The first chapter of this work contains a brief theoretical introduction to the physics of heavy-ion collisions and the QGP. The second chapter provides an overview of recent results in the charmed-meson research, achieved by the LHC in the European Organization for Nuclear Research (CERN) complex near Geneva and RHIC located on Long

Island in the Brookhaven National Laboratory (BNL). The following chapter focuses on the RHIC accelerator complex and the STAR experiment and its sub-detectors. The main practical objective of this work is the measurement of the  $D^\pm$  meson production in Au+Au collisions at center-of-mass energy  $\sqrt{s_{\text{NN}}} = 200$  GeV extracted from a dataset collected by the STAR experiment during the year 2014. This run was significant because it was the first run which featured the Heavy Flavor Tracker (HFT), a silicon detector that can achieve much higher pointing resolution than ever before. The HFT was designed specifically for improving the identification of heavy flavor hadrons with the use of secondary vertex reconstruction. This analysis partially follows the work started by Jakub Kvapil [2], [3] and the main motivation is to improve the signal significance and the reconstruction techniques in order to finalize the analysis and publish the results. The current state of the analysis is described in chapters 4, 5 and 6, which also includes a short introduction to machine-learning techniques used in high-energy physics.

# Chapter 1

## Physics of Heavy-Ion Collisions

Relativistic heavy-ion collisions are interactions of two heavy atomic nuclei traveling at high velocities, close to the speed of light in vacuum ( $\gamma \sim 107$  for a gold ion at the top RHIC energy). The choices of nuclei for the heavy-ion collisions are based on several nuclear properties, such as their shape, nucleon density and the number of (specific) nucleons. The most common type of collisions currently studied are symmetric collisions where both beams consist of the same type of nuclei at the same energy. However, it is also interesting to study asymmetric collisions, such as Cu+Au (STAR, 2012) or fixed-target Au+Au, which is planned by the STAR collaboration in 2019 to explore a specific part of the QCD matter phase diagram (Sec. 1.1). Currently collided are gold nuclei at RHIC and lead nuclei at the LHC. Uranium, copper, aluminum, helium, zirconium and rubidium nuclei were also collided during the operation of RHIC, while xenon nuclei were recently collided by the LHC. The choice of the collided system and the center-of-mass energy is crucial to the measurement since some configurations can yield very interesting and/or surprising results (presence of a critical point, for example). To describe the physics of heavy-ion collisions, several field-specific variables are introduced (Sec. 1.2). Geometry of a heavy-ion collision is characterized by its centrality (Sec. 1.3), which is important for the description of the initial conditions and for the entire evolution of the system (Sec. 1.4). When the energy density of the system reaches about  $1 \text{ GeV}/\text{fm}^3$ , the QGP (Sec. 1.5) is formed. Hundreds to thousands of particles (and antiparticles) are produced in central heavy-ion collisions from the kinetic energy of the incident nuclei, which is roughly two orders of magnitude more than what is produced during proton-proton collisions at the same energy (see Ref. [4] and Ref. [5]).

### 1.1 QCD Phase Diagram

The completion of a phase diagram of the strongly interacting matter is one of the main objectives of today's heavy-ion experiments. It is known that QCD matter can exist in several phases. These phases are distinguished by the temperature  $T$  and the baryon chemical potential  $\mu_B$  at which they occur. The baryon chemical potential is related to the excess of baryons over antibaryons. At "normal" conditions (low  $T$  and

intermediate  $\mu_B$ ) the quarks and gluons are confined inside hadrons - phase known as the hadronic gas. At high temperature the system undergoes a phase transition and becomes the QGP. A neutron star - system observable in the present day Universe - has a near-zero temperature (on the MeV scale) and a large  $\mu_B$ . At even higher values of  $\mu_B$  the system is expected to undergo a phase transition into an exotic phase called a color superconductor. Another interesting feature of the phase diagram is the critical point. At this point the phase transition could be of second order instead of the first order (expected before the critical point) and smooth crossover (observed beyond the CP) phase transition. Finding the location of the critical point in the QCD phase diagram and thus proving its existence is an ongoing task, although some significant progress has been made [6, 7]. A major project aimed at improving our knowledge of the QCD phase diagram has been conducted at STAR (RHIC Beam Energy Scan - Phase I, see Sec. 3.1.2, [8]) with the second part of this project (BES-II) starting in 2019. The QCD phase diagram is illustrated in Fig. 1.1, including the (expected) critical point position, the phase transition lines and the positions of RHIC BES-I and BES-II.

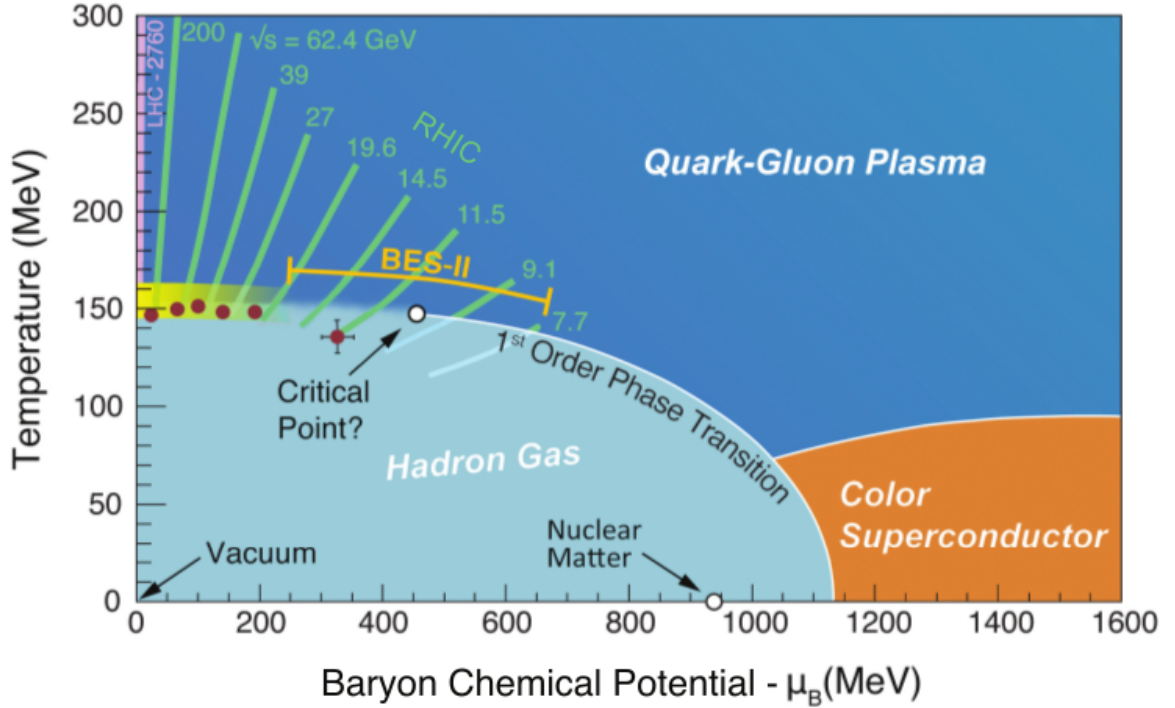


Figure 1.1: An illustration of the QCD phase diagram. The phase transition lines, as well as the critical point, different phases of matter and position of the RHIC Beam Energy Scan measurements can be seen. Taken from Ref. [9].

Some of the probes, that are used as evidence of the QGP formation and to determine the thermodynamical variables essential for the completion of the QCD phase diagram, are discussed in Sec. 1.5.

## 1.2 Variables in Heavy-Ion Collisions

### 1.2.1 Spatial Coordinates

Because of the geometry of the detector, which is usually cylindrical, the common practice is to use cylindrical coordinates to describe general position during heavy-ion collisions. The  $z$  axis is running through the middle of the beam pipe and the origin  $z = 0$  is placed at the interaction point which is the spot in the exact center of the detector, where the beams should intersect (the collisions do not occur precisely in this one spot but rather are distributed along the  $z$  axis). The  $x$  and  $y$  axes can be chosen arbitrarily as long as they are both perpendicular to the  $z$  axis and to each other, therefore defining a plane perpendicular to the  $z$  axis (for example,  $x$  can be horizontal and  $y$  vertical with respect to the ground). Therefore, most vector variables are projected onto the  $z$  axis (referred to as longitudinal projection) and the plane perpendicular to this axis (transverse). For example, the components of the momentum  $\vec{p}$  are usually expressed as longitudinal momentum  $p_z$  and transverse momentum  $p_T$ . The azimuthal angle - usually denoted  $\phi$  - is measured in the perpendicular plane. The polar angle, usually called  $\theta$ , can be used to measure in which direction the products of the collision move away from the origin with respect to the  $z$  axis. However, rapidity  $y$  and pseudorapidity  $\eta$  are used more often because of their simple Lorentz transformation.

### 1.2.2 Transverse Momentum

Transverse momentum  $p_T$  is a projection of the particle momentum into the plane perpendicular to the  $z$  axis. It is defined by the relation

$$p_T = \sqrt{p_x^2 + p_y^2} \quad (1.1)$$

and is independent of the choice of the  $x$  and  $y$  axes (see Subsec. 1.2.1). The transverse momentum is Lorentz-invariant to longitudinal boosts and therefore very useful in describing particles at mid-rapidity during heavy-ion collisions, where the products are traced back to their vertices. The transverse momentum of the approaching projectile is (almost) equal to zero before the collision and is a conserved quantity. This means that when we observe particles with non-zero  $p_T$ , we know that they gained this part of their total momentum during some physical process.

### 1.2.3 Rapidity

The rapidity of particles in heavy-ion collisions is defined by the relation

$$y = \frac{1}{2} \ln \frac{E + p_z}{E - p_z}, \quad (1.2)$$

where  $E$  is the energy of the particle. During longitudinal boosts, the rapidity changes only by an additive constant. Since rapidity incorporates the  $p_z$  component, it can

be used together with  $p_T$  to describe the particle momentum. The regions of detector with high values of  $|y|$  are referred to as the forward sector (or backward if  $y < 0$ ) and the regions with low  $|y|$  as the mid-rapidity sector.

### 1.2.4 Pseudorapidity

Pseudorapidity  $\eta$  is often used instead of the polar angle  $\theta$ , because - same as with rapidity - the differences in pseudorapidity are Lorentz-invariant during longitudinal boosts. It is defined by the following equation:

$$\eta = -\ln \tan \frac{\theta}{2}. \quad (1.3)$$

With the introduction of pseudorapidity, one can express the longitudinal momentum as:

$$p_z = p_T \sinh \eta \quad (1.4)$$

and rapidity as

$$y = \ln \left( \frac{\sqrt{m^2 + p_T^2} \cosh^2 \eta + p_T \sinh \eta}{m^2 + p_T^2} \right), \quad (1.5)$$

which can be simplified to

$$y = \eta - \frac{\tanh \eta}{2} \left( \frac{m}{p_T} \right)^2, \quad (1.6)$$

from where it is easy to see, that pseudorapidity converges to rapidity in the ultrarelativistic limit ( $m \ll p_T$ ). The reason why  $\eta$  is often preferred to  $y$  to describe the position of the particles is that the only unknown that needs to be measured is the polar angle.

## 1.3 Collision Centrality

The nuclei rarely collide "head-on" during heavy-ion collisions. Instead, they overlap by a generally random portion. Nucleons, that are in the overlapping region are referred to as participants, the remaining nucleons are called spectators and do not participate in the collision. The overlapping part of the two nuclei can be characterized by an impact parameter  $b$ . The impact parameter is defined as the distance between the centers of both nuclei at the point of the collision (Fig. 1.2).

There are three broad categories of collisions based on the value of  $b$ . If  $b \simeq 0$ , the collision is classified as central. For  $0 < b < R_A + R_B$ , where  $R_A$  and  $R_B$  are the radii of the two colliding nuclei, we are talking about (mid)peripheral collisions and a special case are the ultra-peripheral collisions ( $b > R_A + R_B$ ) where the nuclei don't actually hit each other, but still interact via the electromagnetic interaction.

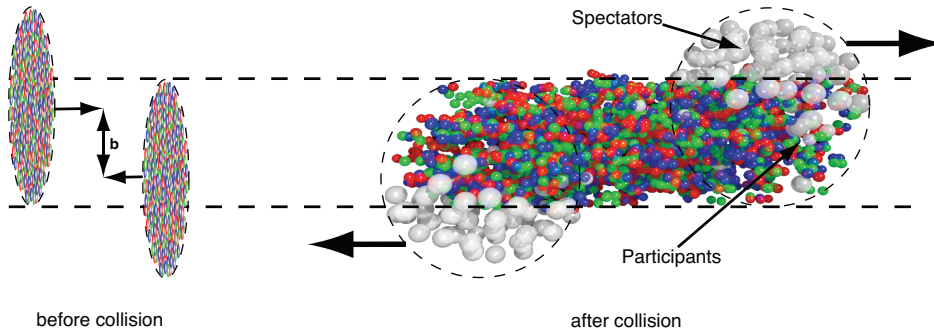


Figure 1.2: Illustration of a nucleus-nucleus collision. Participants, spectators and the impact parameter  $b$  are shown. Taken from Ref. [10].

The impact parameter cannot be measured directly, but one way to estimate  $b$  is to measure the particle multiplicity. Multiplicity is the number of tracks created during the event. More central collisions should create more tracks, later detected in the Time-Projection Chamber (TPC). Then for example the 10 % of the events with the highest multiplicity are defined as events within centrality range 0 – 10 %. An example of an ALICE centrality measurement can be seen in Fig. 1.3.

The Monte Carlo Glauber (MC-Glauber) model [12] is the most frequently used theoretical model describing the centrality of the collision and its relation to the impact parameter. The basis of this model is the geometry of the incident nuclei. The position of the individual nucleons is modeled by the Woods-Saxon potential and uses an optical-limit approximation, which assumes, that the nucleons pass through each other essentially undeflected at high energies. The nucleons also move independently inside the nucleus and the range of the nucleon-nucleon interaction is small compared to the size of the nucleus in this model.

## 1.4 Collision Space-Time Evolution

It can be assumed, that during the heavy-ion collisions the nucleons in the overlapping region participate in a sequence of one or more binary collisions. New particle - antiparticle pairs are being created from the vacuum and the system is not in a thermal equilibrium. A very hot and dense fireball is formed and the partons (quarks and gluons), which are not bound inside hadrons in this stage, can interact with large momentum transfers (hard scattering). This is the stage during which almost all the heavy ( $c$  and  $b$ ) quarks are created (at RHIC energies), which means that their number is conserved until they have formed heavy hadrons which we then reconstruct from their weak decays. When a thermal equilibrium is reached ( $\tau \sim 1 \text{ fm}/c$ ), the system is following hydrodynamic laws similarly to a superfluid that cools down and expands in time and space. After the temperature has decreased below the critical temperature  $T_c \sim 175 \text{ MeV}$ , the system enters a new phase - the hadronization. The system further cools down and expands during this stage, but the quarks and gluons cannot be free anymore and become confined in baryons and mesons, held together by the strong

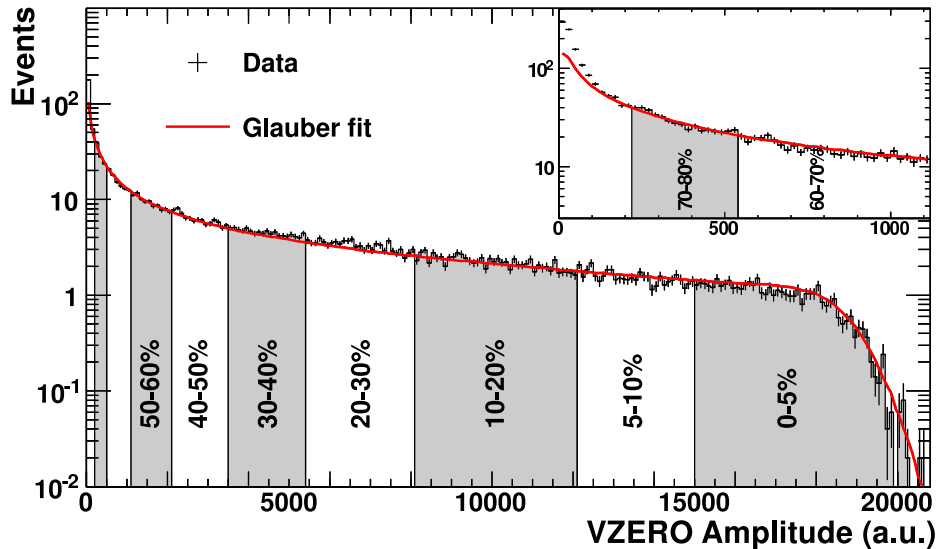


Figure 1.3: ALICE measurement of centrality in 2.76 TeV Pb+Pb collisions. Event count is plotted against the ALICE V0 detector signal amplitude, proportional to particle multiplicity. Data are fitted by the MC-Glauber model prediction. Taken from Ref. [11].

interaction. The hadronization period can be further divided into two stages. During the first stage, new particles can still be created, until the temperature decreases below a certain threshold and a chemical freeze-out occurs. During the second stage, remaining hadrons still elastically collide among themselves, as the temperature decreases further, until the mutual interactions stop entirely. This point in space-time is called the kinetic freeze-out ( $\tau \sim 10$  fm/c). Hadrons that live long enough (pions, kaons and protons) can be then captured in a detector along with charged leptons and photons. This entire evolution of the relativistic heavy-ion collision is illustrated in Fig. 1.4.

## 1.5 Quark-Gluon Plasma

The Quark-Gluon Plasma is a state of matter, where quarks and gluons are quasi-free, unlike in hadronic matter, where they are confined inside hadrons by the strong force. The existence of the QGP was just a speculation for a long time before it has been confirmed experimentally by RHIC experiments in 2004 [14, 15, 16, 17]. The QGP is an interesting medium to study, since the early Universe is thought to be in this state between the end of the inflation period and hadronization,  $t \sim 10^{-6}$  s after the Big Bang. The QGP is known to be extremely hot, dense and moving with low viscosity ( $\eta/s \sim 0.1$ ), therefore its behavior can be compared to the behavior of nearly ideal liquids. The QGP is also the most vortical fluid ever observed ( $\omega \approx (9 \pm 1) \times 10^{21}$  s $^{-1}$ ) as reported by the STAR collaboration in 2017 [18].

The physics of the QGP is governed by the strong interaction between color charged partons. The theory describing the strong interaction is the quantum chromodynamics

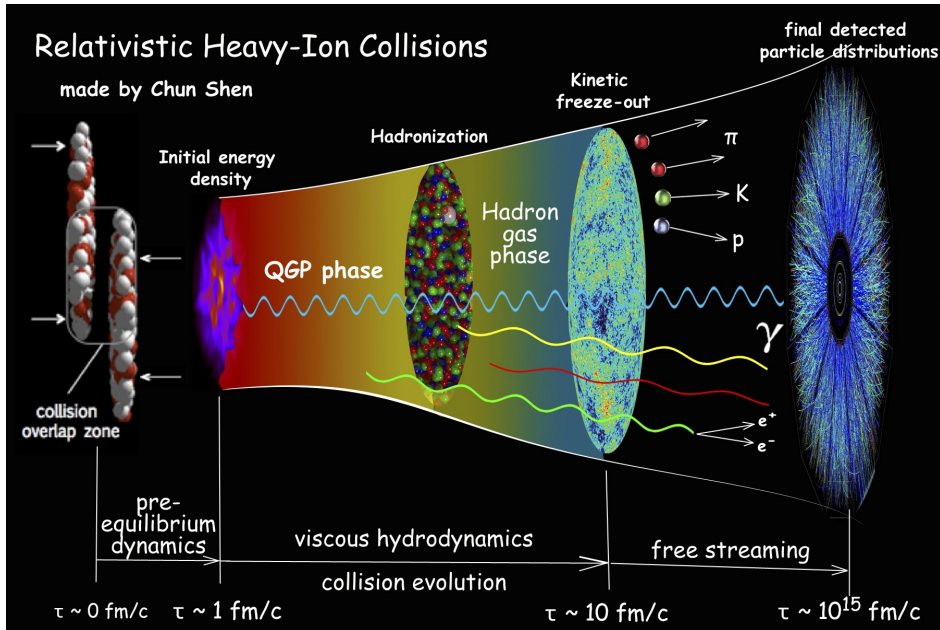


Figure 1.4: The illustration of the evolution of a relativistic heavy-ion collision with important stages marked. Taken from Ref. [13].

(QCD). Color charge is a quantum number similar to the electric charge, but there are 6 possible color states (red, green, blue and corresponding anticolors called antired, antigreen and antiblue), instead of just 2 electric charges (positive, negative). Quarks carry one unit of a color charge, while gluons carry a combination of one color and one anticolor and bind quarks together to form hadrons. This is a major difference from the electromagnetic force, because the EM force gauge bosons (photons) are not charged and cannot interact with each other, while gluons often do interact among themselves. One property of the strong interaction is, that all hadrons must be color-neutral objects. This means that baryons are composed of 3 quarks, one of each color (antibaryons are composed of 3 antiquarks, one of each anticolor), while mesons are composed of a colored quark and an antiquark of the corresponding anticolor. The characteristic time of the strong interaction, approximated as the time in which a gluon traveling at the speed of light  $c$  overcomes a distance comparable to the size of a nucleon (1 fm) is  $\tau \sim 10^{-23}$  s. The parameter describing the effective strength of this interaction is the strong interaction coupling constant,

$$\alpha_s(Q) = \frac{12\pi}{(33 - 2N_f) \ln \frac{Q^2}{\lambda_{\text{QCD}}}}, \quad (1.7)$$

where  $N_f$  is the number of quark flavors,  $Q^2$  is the four momentum transfer and  $\lambda_{\text{QCD}} \simeq 0.2$  GeV is the typical QCD scale, obtained experimentally [19]. Despite its name, the  $\alpha_s$  is not a true constant. The dependence on momentum transfer (therefore on energy and temperature as well) can be seen in Fig. 1.5.

Simple reasoning then shows that four momentum transfer  $Q^2$  is correlated with the energy available in the system which can be parametrized by the temperature  $T$ , while

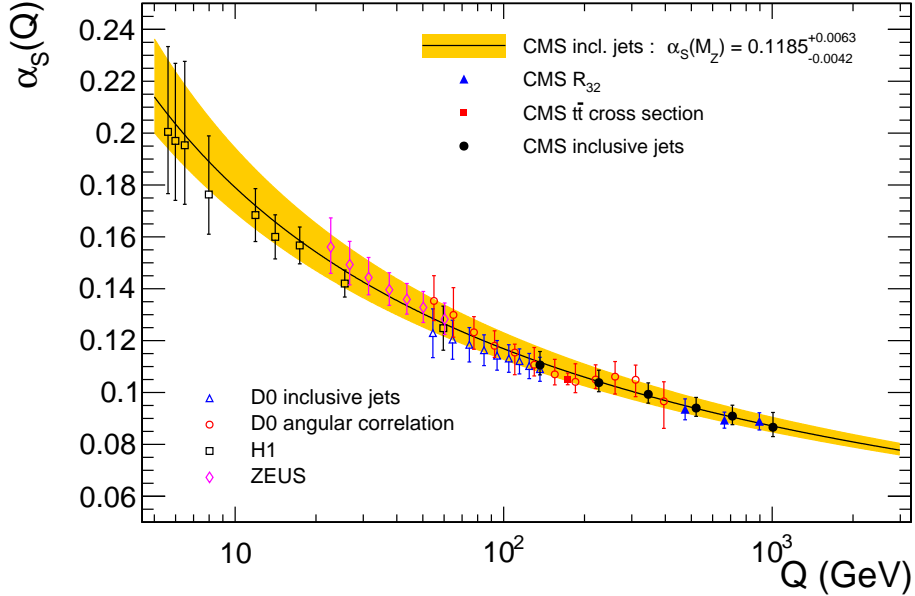


Figure 1.5: CMS measurement of the strong interaction coupling constant  $\alpha_s$  dependence on momentum  $Q$ . Data compared to pQCD calculation and results from other experiments (D0, H1 and Zeus).  $\alpha_s(M_Z)$  is the value at the mass of  $Z^0$  boson. Taken from Ref. [20].

it is anticorrelated with the distance  $r$ , over which the interaction acts. When the two partons move apart,  $\alpha_s$  increases to the point, where it is more energetically favorable to create a new quark-antiquark pair from the vacuum rather than to allow any further separation (confinement). This can be illustrated by an example with a string. Suppose we have a string and pull the ends apart, at some point, the string will snap, creating two shorter strings and reducing the tension. On the other hand, at short distances ( $r < r_c \sim 0.5$  fm), the partons are allowed to move almost freely (asymptotic freedom). From another point of view, when the temperature of the system is high, the strong interaction is not strong enough to hold the quarks and gluons together and allows them to move freely. The critical temperature for the deconfinement is  $T_c = 140 - 200$  MeV, depending on calculation [21, 22, 23].

When a highly energetic parton moves through the QGP, it might interact with the other partons and lose energy (see Subsec. 1.5.1). This has a direct effect on the yield particles at particular  $p_T$  that we observe in A+A collisions with respect to the properly scaled p+p collisions. The modification of the yield can be parametrized by a variable called the nuclear modification factor, which is introduced in Subsec. 1.5.2. Since it is impossible to observe and study the QGP directly because of its very short lifetime and rather extreme nature, the only way to obtain desired variables of the QGP, such as its temperature, density and viscosity, is using probes. Charmed quarks are an example of a hard probe. They are created before the QGP and therefore experience the entire evolution of the system, while the number of these quarks is conserved. Some other hard processes frequently used as probes are jet quenching and quarkonium production suppression, which are discussed briefly in subsections 1.5.3

and 1.5.4. Soft probes, such as the flow of the particles in the system (Subsec. 1.5.5), do not rely on highly energetic processes, but rather utilize the collective behavior of the system after the QGP has formed.

### 1.5.1 Parton Energy Loss

When a parton moves through a strongly-interacting medium, such as the QGP, it might interact with the free color charges in the medium and lose energy. Similar situation occurs in everyday situations, for example: an electron traveling through a material will interact with the atoms via the electromagnetic force and lose energy. The more energetic the electron is, the further it will travel through the material until it stops. The EM energy losses for heavy particles follow the well-known Bethe-Bloch formula:

$$-\left\langle \frac{dE}{dx} \right\rangle = 4\pi N_A r_e^2 m_e c^2 \frac{Z}{A} \frac{1}{\beta^2} \left[ \frac{1}{2} \ln \frac{2m_e c^2 \beta^2 \gamma^2 T_{\max}}{I^2} - \beta^2 - \frac{\delta(\beta\gamma)}{2} \right], \quad (1.8)$$

where  $N_A$  is the Avogadro number,  $r_e$  and  $m_e$  are the electron classical radius and mass respectively,  $Z$  and  $A$  are proton and atomic numbers of the material,  $\beta = \frac{v}{c}$ ,  $\gamma = \frac{1}{\sqrt{1-\beta^2}}$ ,  $T_{\max}$  is the maximum energy transfer of one interaction,  $I$  is the mean excitation energy and  $\delta(\beta\gamma)$  is the density correction term. An example of the formula for muon passing through copper can be seen plotted in Fig. 1.6.

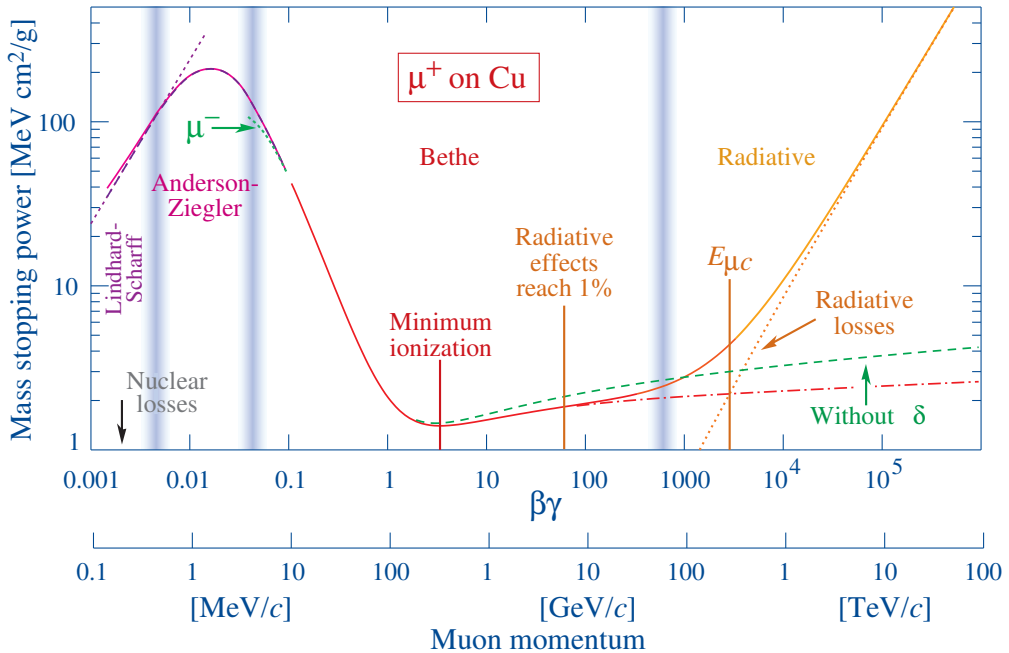


Figure 1.6: The mean energy loss dependence on momentum for muon passing through copper. For lower energies, the behavior is described by the Bethe-Bloch formula (eq. 1.8, while at higher energies the radiation dominates. Taken from Ref. [1].

The difference between energy losses in a bulk of copper and the QGP is that the QGP is much denser and that even the mediators of the strong interaction - gluons

- are charged and therefore the energy loss is much more intense to the point that even partons with high momentum will not travel very far in this medium. There are two principal means of energy loss inside the QGP - elastic collisions and radiative losses. Collisions dominate at lower energies while radiation (of gluons) dominates at high energies. For the energy loss of a heavy quark (with a mass  $M$  and energy  $E$ ) via elastic collisions while traversing a distance  $l$  in medium of temperature  $T$ , the following formula

$$-\frac{dE}{dl} = \frac{1}{4}C_R\alpha_s(ET)m_D^2 \ln\left(\frac{ET}{m_D^2}\right) - \frac{2}{9}C_R\pi T^2 \left[ \alpha_s(M^2)\alpha_s(ET) \ln\left(\frac{ET}{M^2}\right) \right], \quad (1.9)$$

where  $C_R = 4/3$  is the color charge factor of the quark and  $m_D^2 \simeq 4\pi\alpha_s T^2(1 + N_f/6)$  is the Debye mass squared, holds [24]. The radiative losses are achieved via "gluonstrahlung" - the emission of gluons. They can be calculated in two limiting cases, based on the thickness  $L$  of the medium compared to the radiation length  $\lambda$ . For the thin medium case ( $L \ll \lambda$ ), the energy loss can be calculated via eq. 1.10.

$$\Delta E_{\text{rad}} \approx \alpha_s C_R \hat{q} L^2 \ln\left(\frac{E}{m_D^2 L}\right), \quad (1.10)$$

where  $\hat{q}$  is the transport coefficient of the medium. In the thick medium case ( $L \gg \lambda$ ) we have to further differentiate between the soft and hard gluon emissions. These cases are based on the characteristic gluon energy  $\omega_c = \frac{1}{2}\hat{q}L^2$ . The equations for the energy loss are then:

$$\Delta E_{\text{rad}} \approx \alpha_s C_R \begin{cases} \hat{q}L^2, & \omega < \omega_c \\ \hat{q}L^2 \ln(E/(\hat{q}L^2)), & \omega > \omega_c. \end{cases} \quad (1.11)$$

More details about the ways partons lose energy in strongly interacting medium can be found in Ref. [24] and [25].

## 1.5.2 Nuclear Modification Factor

Because of the parton energy loss mechanisms described in Subsec. 1.5.1 and because of the Cold Nuclear Matter (CNM) effects, such as shadowing or anti-shadowing, the Cronin effect, nuclear absorption and others, the particle yields measured in A+A collisions will be different than the properly scaled yields measured in p+p collisions. To measure the effect that the medium has on the production, it is common to introduce a variable called the nuclear modification factor  $R_{AA}$ . It is the ratio of the measured A+A yield and the measured p+p yield scaled by the mean number of binary collisions:

$$R_{AA} = \frac{\frac{d^2 N_{AA}}{dp_T dy}}{\langle N_{\text{coll}} \rangle \times \frac{d^2 N_{pp}}{dp_T dy}}. \quad (1.12)$$

This factor then includes all effects of the nuclear matter. Additional measurements are required to separate effects caused by the QGP from the CNM effects. To determine

these effects, caused by the mere presence of a nucleus, results from p/d+A collisions (characterized by a factor  $R_{pA}/R_{dA}$ , defined similarly as  $R_{AA}$ , 1.12) are studied. In these systems, the above-mentioned CNM effects are present, but the QGP is not expected to be created (at RHIC energies).

The effect that a strongly interacting medium has on the particles can be seen in Fig. 1.7. At high  $p_T$ , all particles are suppressed with the exception of direct photons (orange, they are unaffected by the medium, because they carry no color charge). The protons (purple) appear enhanced at  $p_T \simeq 2$  GeV/c as a result of the Cronin effect [26] and the baryon anomaly [27]. The electrons in question (grey) come from heavy flavor (b, c) decays and are suppressed as a result of heavy flavor quark suppression, while directly produced electrons would be unaffected by the medium the same way as the direct photons. Another way to compare the effects of the hot, strongly interacting medium is to calculate the central-to-peripheral modification factor  $R_{CP}$ , which compares the yields in the two different centrality bins and is normalized by the corresponding mean numbers of binary collisions:

$$R_{CP} = \frac{\langle N_{coll}^P \rangle}{\langle N_{coll}^C \rangle} \times \frac{\frac{d^2 N_{AA}^C}{dp_T dy}}{\frac{d^2 N_{AA}^P}{dp_T dy}}. \quad (1.13)$$

Results from charmed meson production measurements - which usually include the measurement of  $R_{AA}$  and/or  $R_{CP}$  - are summarized in Ch. 2.

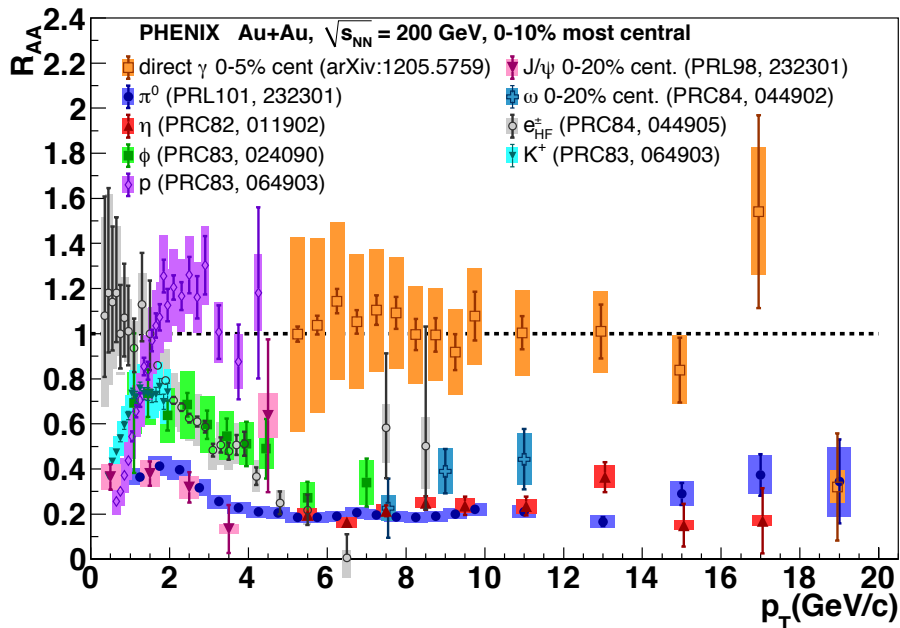


Figure 1.7: The PHENIX collaboration results of  $R_{AA}$  measurements for several identified particle species in 0-10 % most central Au+Au collisions at  $\sqrt{s_{NN}} = 200$  GeV. Taken from Ref. [25] + references in the figure.

### 1.5.3 Jet Quenching

A jet is defined as a narrow collimated bunch of particles. It is the final product of a fragmentation and hadronization of a hard parton. When this hard parton moves, it radiates gluons which can create new particles and these products then move in the general direction of the original parton. A pair of opposite-going partons is usually created during hard scattering, leading to back-to-back dijets. Interesting dijets are those, which form on the edge of the fireball and one of these jets goes straight to the vacuum (and then the products will enter the detector), while the other jet traverses the medium created after the collision. This jet will then interact in the QGP and its energy will be "quenched" - not detected - while the jet that traveled through the vacuum will be visible. Observations of single jets, with quenched jet on the other side are now interpreted as one of the most significant indications of a QGP formation. It is difficult to identify jets in Au+Au collisions due to the large background consisting of low- $p_T$  particles. However, some interesting features might be visible in dihadron azimuthal correlations. The measurement of dihadron azimuthal correlations can be seen in Fig. 1.8, where the peak at  $\phi \sim 0$  corresponds to two particles from a single jet and is visible in p+p, central d+Au and central Au+Au collisions at STAR. The peak at  $\phi \sim \pi$ , observed in p+p and d+Au collisions, corresponds to an enhancement in dihadron correlations due to the back-to-back dijet formation. However, there is no such structure observed in central Au+Au collisions, which means, that if we can indeed link the azimuthal correlations to the jet fragmentation, we observe a significant quenching of jets in the medium created in central Au+Au collisions. It is important to note that this phenomenon is only visible for high- $p_T$  particles. The requirement for the trigger particle was  $p_T > 4$  GeV/c and for the associated particle  $p_T > 2$  GeV/c. For a more detailed information about jets and jet quenching see for example Ref. [24] or [28].

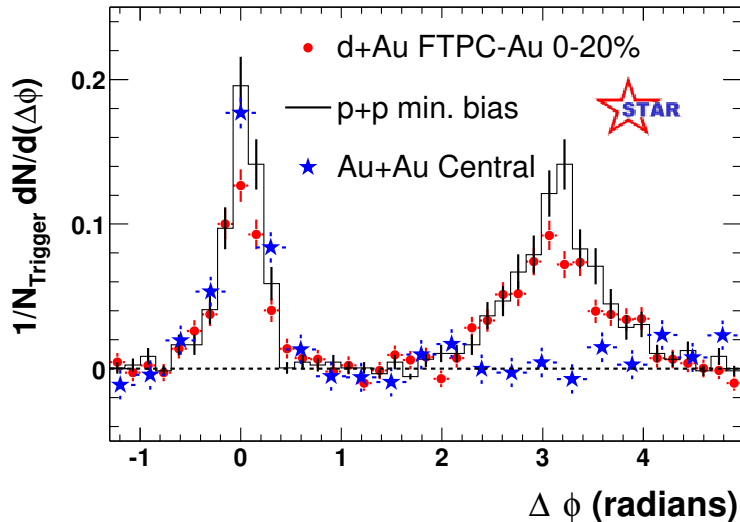


Figure 1.8: STAR measurement of dihadron azimuthal correlations at high  $p_T$  for p+p (black line), central d+Au (red circles) and central Au+Au (blue stars) collisions at  $\sqrt{s_{NN}} = 200$  GeV. Taken from Ref. [14].

## 1.5.4 Quarkonia Production Suppression

Quarkonia (such as  $J/\psi$  or  $\Upsilon$ ) are bound states of heavy quark-antiquark pairs, which are predominantly created during the hard part of the collision, before the QGP has formed. The suppression observed in quarkonia production, first predicted by Matsui and Satz in 1986 [29], is a strong indication of a QGP formation. The suppression of their production is caused by a phenomenon called the Debye screening. The presence of free color charges in the QGP causes the Debye radius - the distance over which the two quarks can still "feel" each other - to decrease below the actual radius of the quarkonium, causing it to dissolve.  $J/\psi$  production shows high level of suppression in central A+A collisions, as seen in Fig. 1.9 for Au+Au collisions at  $\sqrt{s_{NN}} = 39, 64$  and 200 GeV and U+U collisions at  $\sqrt{s_{NN}} = 193$  GeV.

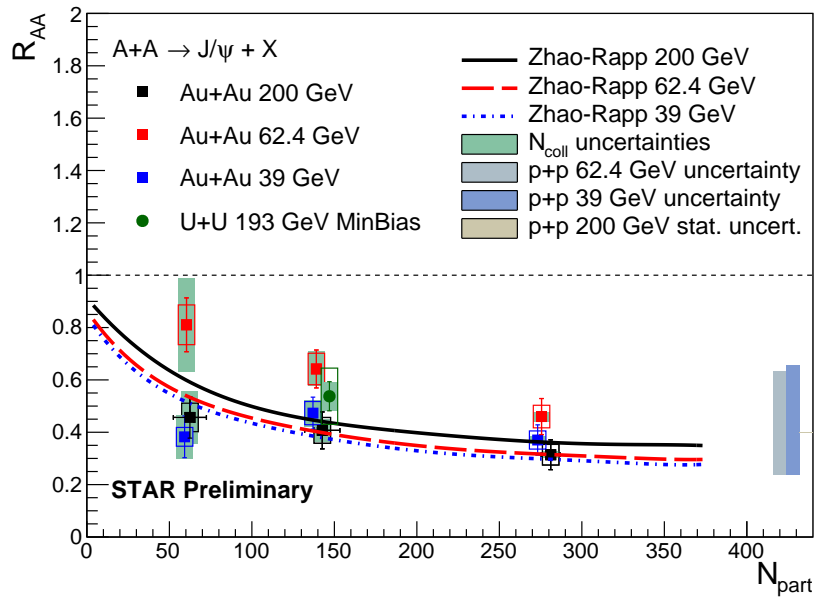


Figure 1.9: Preliminary STAR results of the  $J/\psi$  nuclear modification factor  $R_{AA}$  in Au+Au ( $\sqrt{s_{NN}} = 39, 62.4$  and 200 GeV) collisions and U+U ( $\sqrt{s_{NN}} = 193$  GeV) collisions as a function of the number of participants  $N_{part}$  along with theoretical predictions [30]. Taken from Ref. [31].

Different quarkonia types have different binding energies. The more energetic the bound between the two heavy quarks is, the smaller is the radius of the quarkonium. For example,  $\Delta E = 0.64$  GeV and  $r_0 = 0.50$  fm for  $J/\psi$ , while  $\Delta E = 1.10$  GeV and  $r_0 = 0.28$  fm for  $\Upsilon(1S)$  [32]. Therefore, when we increase the temperature of the system (thus decreasing the Debye screening radius), we will observe the suppression of more and more quarkonium states (sequential melting). One can then determine the approximate temperature of the system by measuring the production of different quarkonia and observe, which quarkonium states "survive" in the QGP, therefore effectively creating a quarkonium thermometer. For more details about quarkonia and their suppression, please refer to Ref. [23], [32] or [33].

### 1.5.5 Flow

Flow of the particles is the result of an initial anisotropy of the system. Because most of the heavy-ion collisions are not head-on (see Sec. 1.3), the participant distribution is not uniform. As a result, there is a pressure gradient, which in turn leads to a collective motion of the particles inside the medium, which is a process governed by hydrodynamic laws. We observe this behavior as an asymmetry in the azimuthal distribution of particles. This asymmetry is parametrized by flow coefficients  $v_n = \langle \cos[n(\phi - \Psi_{\text{RP}})] \rangle$ , where  $\Psi_{\text{RP}}$  is the reaction plane angle, defined by the beam line and the line connecting the centers of both nuclei. These coefficients are present in the Fourier series expansion of the particle momentum distribution function (see Ref. [34] or [35] for details):

$$E \frac{d^3N}{d^3p} = \frac{1}{2\pi} \frac{d^2N}{p_T dp_T d\eta} \left( 1 + 2 \sum_{n=1}^{\infty} v_n \cos[n(\phi - \Psi_{\text{RP}})] \right), \quad (1.14)$$

where  $E$  is the energy of the particle. The momentum anisotropy then translates into the anisotropy of the particle production in the azimuthal angle. The most important flow coefficients are the  $v_1$ ,  $v_2$  and  $v_3$ , describing directed, elliptic and triangular flow, although even higher flow coefficients were measured [35]. The directed flow has two components, one is even in rapidity and is a result of event-by-event fluctuations in the initial nuclei and is unrelated to the reaction plane. The rapidity-odd component describes the collective side-ward motion of particles emitted from the collision point which is caused by the large magnetic field created by the moving spectators. This is the traditional definition of  $v_1$ . The STAR collaboration has recently published new results from the  $v_1$  measurements (see Fig. 1.10) indicating a non-zero flow for both charged pions and (anti)protons for various beam energies. The changes in the slope of the directed flow and the presence of the minimum in net proton slope are thought to be indications of a first-order phase transition between the QGP and the hadronic gas phase at this energy scale. However, the UrQMD hadronic cascade model does not describe the data correctly.

The elliptic flow  $v_2$  has long been thought as a strong indication of the QGP formation. It arises from the initial state anisotropy, where for mid-peripheral collisions the collision zone has the typical almond shape which leads to a pressure gradient as illustrated in Fig. 1.11 - left. The third flow coefficient  $v_3$  represents triangular flow. This flow arises from event-by-event fluctuations of the nucleon distributions of the colliding nuclei. Because the nuclei cannot be treated as balls (or Lorentz-contracted pancakes), the overlapping portions of the two nuclei do not always form a perfect almond shape which gives rise to another type of anisotropy. This situation is illustrated in Fig. 1.11 - right.

The STAR experiment has measured both elliptic and triangular flow of charged particles and the results can be seen in Fig. 1.12, showing significant elliptic and triangular flow with the elliptic flow increasing with centrality and  $p_T$  and the triangular flow remaining nearly constant, because the fluctuations that cause  $v_3$  should not be affected much by the centrality. The viscous hydrodynamic calculation with shear viscosity per unit entropy density  $\eta/s = 0.08$  seems to describe the data very well, while calculation with  $\eta/s = 0.16$  tends to underestimate the data and the ideal hydrody-

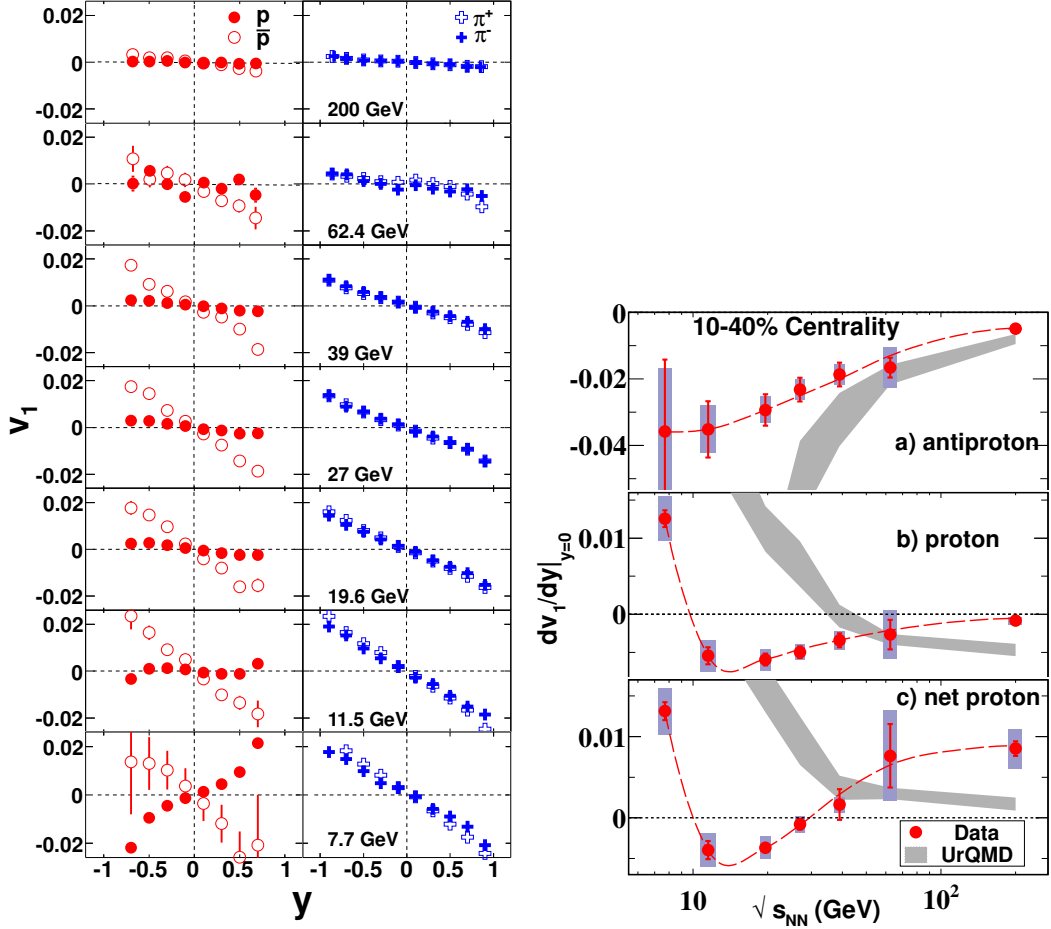


Figure 1.10: Left: STAR measurement of the directed flow of charged pions and (anti)protons for various beam energies at mid-rapidity. Right: The slope of the directed flow for antiprotons, protons and net protons as a function of the beam energy compared to UrQMD prediction. Taken from Ref. [36].

dynamic calculation overestimates both  $v_2$  and  $v_3$ . The PHSD model describes the  $v_3$  data well in the 30-40 % range, while the AMPT and NeXSPheRIO models tend to overestimate the data at higher  $p_T$ .

Flow, or more broadly particle collectivity, is one of the most active fields of research in the QGP physics and there are indications that there is measurable particle collectivity in smaller systems, such as p+A or even p+p collisions. The D-meson-related flow measurements are presented in Ch. 2.

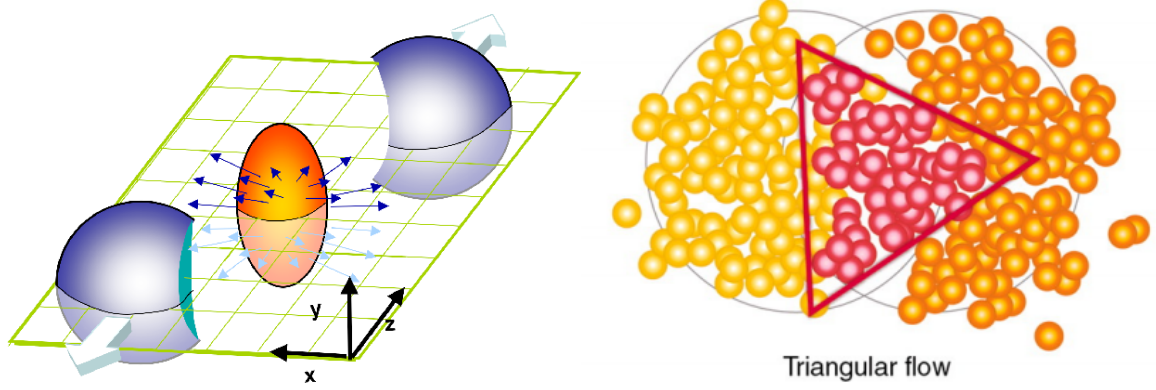


Figure 1.11: Left: The typical almond shape of the collision zone between two nuclei leading to elliptic flow development. Taken from Ref. [37]. Right: An illustration of the fluctuations within both colliding nuclei that give rise to the triangular flow. The red spots indicate participants. Taken from Ref. [38].

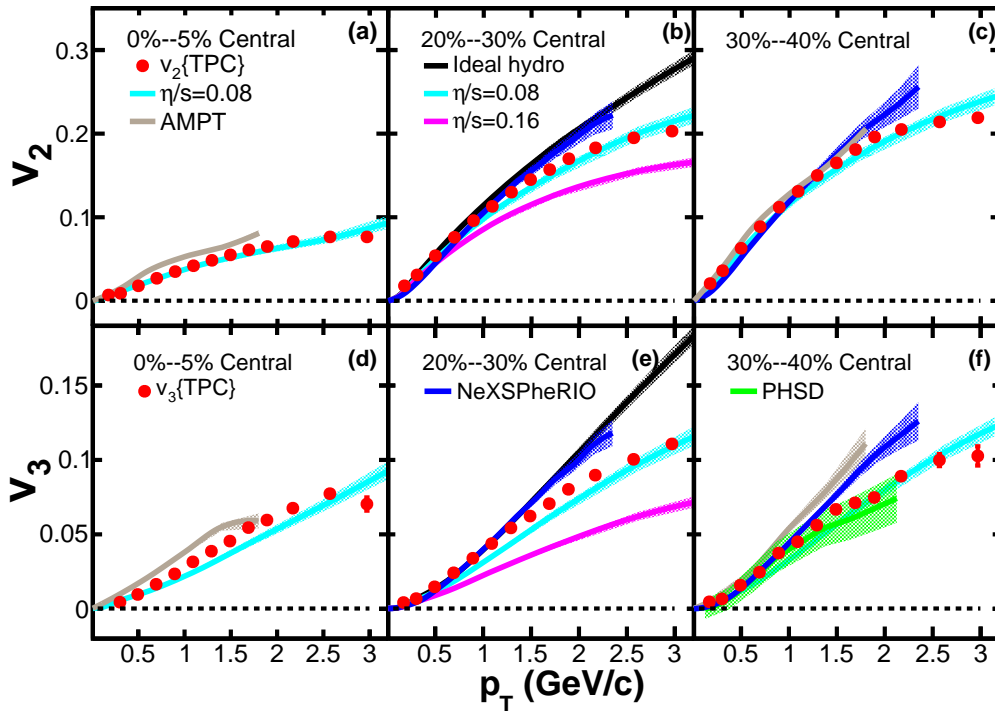


Figure 1.12: Elliptic and triangular flow coefficients  $v_2$  (top) and  $v_3$  (bottom) as a function of  $p_T$  for charged particles in different centralities (0-5 % - left, 20-30 % - middle, 30-40 % - right) as measured by the STAR experiment in Au+Au collisions at  $\sqrt{s_{NN}} = 200$  GeV. The results are compared to ideal (b),(e) and viscous hydrodynamic calculation (all) [39] and the AMPT transport (a),(c),(d),(f) [40], NeXSPheRIO (b),(c),(e),(f) [41], and Parton Hadron String Dynamics (f) [42] models. Taken from Ref. [43],  $v_2$  values taken from Ref. [44].

# Chapter 2

## Recent RHIC and LHC Results

Because of the high mass of the  $c$  quark, its energy loss inside the hot and strongly interacting medium is expected to be lower than for light quarks and gluons due to the dead cone effect [45]. The main motivation behind the open-charmed  $D^\pm$  measurements, is to confirm the results obtained from previous  $D^0$  measurements that - at high  $p_T$  - there is a significant suppression in  $D$  meson production as a consequence of large energy loss of the  $c$  quarks in the QGP. The  $D^\pm$  results in A+A collisions are usually compared to the results from p+p collisions and to previous  $D^0$  results, since the behavior is expected to be roughly the same for both particles. The  $D$  meson production at mid-rapidity is currently measured by four experiments at two particle accelerators. The STAR experiment is located at the Relativistic Heavy Ion Collider (RHIC) in Brookhaven National Laboratory (BNL) in the USA and the ALICE, ATLAS and CMS experiments are currently operating at the Large Hadron Collider (LHC) run by the European Organization for Nuclear Research (CERN) under the Swiss/French border. The results from these experiments are summarized in this chapter. The  $D^\pm$  is usually reconstructed from a three-body decay channel  $D^\pm \rightarrow K^\mp + \pi^\pm + \pi^\pm$ , while  $D^0$  is usually reconstructed from a two-body decay channel  $D^0 \rightarrow K^- + \pi^+$  (and vice versa for  $\bar{D}^0$ ) as these are the hadronic channels with the highest branching ratios  $BR_\pm = 8.98 \pm 0.28 \%$  and  $BR_0 = 3.89 \pm 0.04 \%$  [1]. The values of the  $c$  quark fragmentation function, effectively the probability that the  $c$  quark will form a given  $D$  meson, are  $f(c \rightarrow D^+) = 0.246 \pm 0.020$  and  $f(c \rightarrow D^0) = 0.565 \pm 0.032$  [1].

### 2.1 D Mesons in p+p Collisions

The baseline reference used to calculate the nuclear modification factors at STAR comes from the measurement of combined  $D^0$  and  $D^*$  cross-section in  $\sqrt{s_{NN}} = 200$  GeV p+p collisions taken during the year 2009, which can be seen in Fig. 2.1. The data points are compared to the Fixed Order + Next-to-Leading Logarithms (FONLL) pQCD calculation [46] and - as is the case with similar data points from LHC experiments - lie on the upper bound of the prediction. It can be seen that the points do not cover sufficient  $p_T$  range and therefore it would be very beneficial to take new data from p+p collisions with higher statistics and quality.

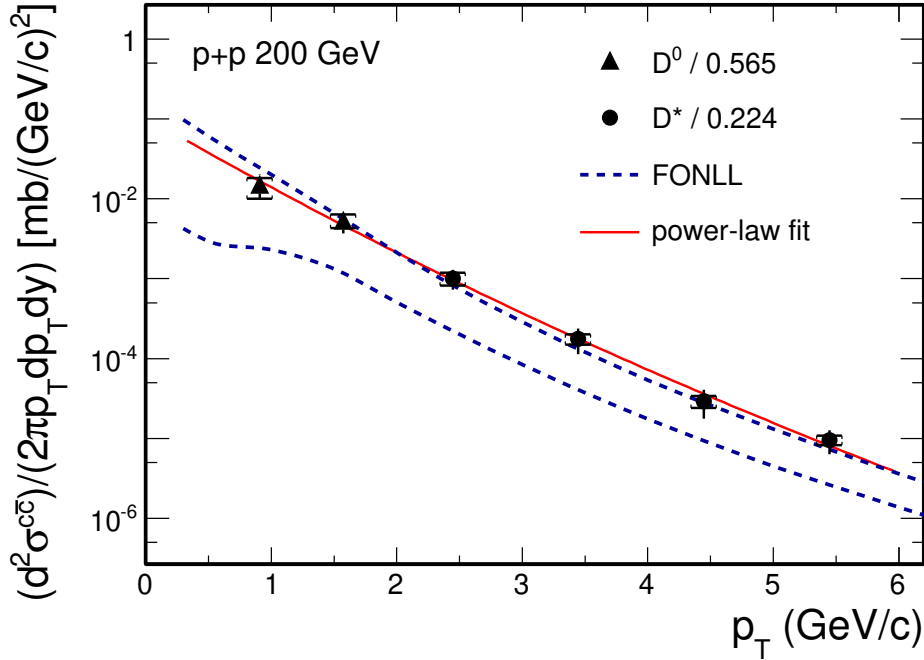


Figure 2.1: STAR measurement of  $D^0$  and  $D^*$  cross-section in proton-proton collisions at  $\sqrt{s} = 200$  GeV. Data points are scaled by the respective charm fragmentation ratio, fitted by a power-law function and compared to FONLL prediction. Taken from Ref. [47].

The ALICE collaboration presented their preliminary results of  $D^0$  and  $D^+$  cross-section from p+p collisions at  $\sqrt{s} = 5.02$  TeV to be used as a reference for the results from Pb+Pb collisions. The cross-section dependence on transverse momentum at mid-rapidity within the  $0 < p_T < 35$  GeV/ $c$  range can be seen in Fig. 2.2 and shows behavior consistent with the FONLL prediction and with the results of other experiments - data points near the upper bound of the prediction.

The ATLAS collaboration published results of their measurement of the  $D^\pm$  production cross-section in p+p collisions at  $\sqrt{s} = 7$  TeV in 2016 [49]. The  $D^\pm$  cross-section measurement as a function of transverse momentum in the  $3.5 < p_T < 100$  GeV/ $c$  range at mid-rapidity is shown in Fig. 2.3. The results are consistent with FONLL prediction and, similarly to other experiments, the data points lie near the upper bounds of the predictions. The general-mass variable-flavor-number scheme (GM-VFNS) prediction seems to describe the data fairly well and the Monte Carlo (MC) simulations (POWHEG, MC@NLO) tend to underestimate the data points.

The CMS collaboration has also measured the  $p_T$  spectrum ( $2 < p_T < 100$  GeV/ $c$ ) of prompt  $D^0$  mesons at mid-rapidity in p+p and Pb+Pb collisions at 5.02 TeV [53]. The results from p+p collisions are shown in Fig. 2.4. The spectrum follows the same trend as in STAR, ALICE and ATLAS measurements - data points lying at the upper bound of the FONLL prediction while the GM-VFNS prediction seems to slightly overestimate the data.

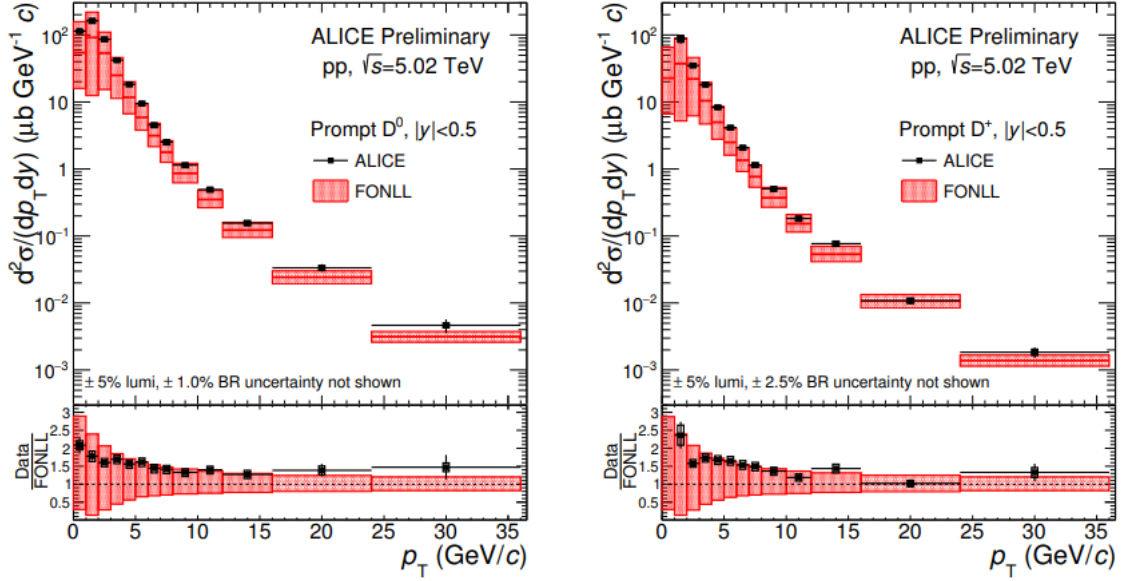


Figure 2.2: Preliminary results of prompt  $D^0$  and  $D^+$  cross-section dependence on  $p_T$  at mid-rapidity in p+p collisions at  $\sqrt{s} = 5.02$  TeV as measured by the ALICE experiment. Data are compared to the FONLL prediction. Taken from Ref. [48].

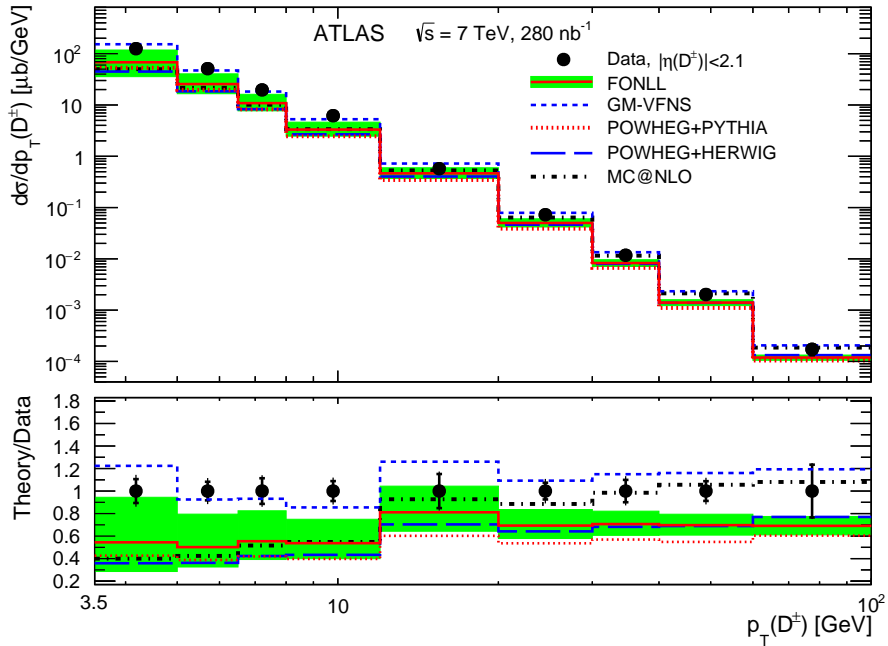


Figure 2.3: The ATLAS collaboration results of  $D^\pm$  production cross section as a function of  $p_T$  at mid-rapidity and  $3.5 < p_T < 100$  GeV/c range. Compared to FONLL, GM-VFNS [50], POWHEG ([51], with both PYTHIA and HERWIG) and MC@NLO [52] predictions. Taken from Ref. [49].

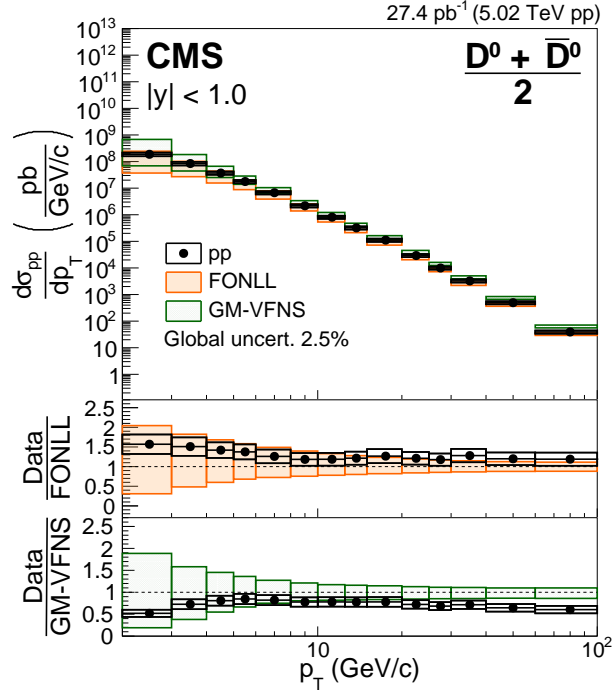


Figure 2.4: The  $D^0$  and  $\bar{D}^0$  production cross section at mid-rapidity in 5.02 TeV p+p collisions as measured by the CMS collaboration. Data comparison to FONLL and GM-VFNS predictions is also shown. Taken from Ref. [53].

## 2.2 D Mesons in p+A Collisions

ALICE preliminary results from p+Pb collisions at backward rapidity (direction of the nucleus) show the  $R_{pPb}$  consistent with unity across the entire transverse momentum range ( $0 < p_T < 35$  GeV/c) range (Fig. 2.5). This behavior seems to disfavor the incoherent multiple scattering model [55] while other models are being consistent with the data points within uncertainties.

Fig. 2.6 shows the preliminary results from p+Pb collisions at  $\sqrt{s_{NN}} = 8.16$  TeV which were presented at the 2018 Quark Matter conference by the ATLAS collaboration. These results show that the Forward/Backward ratio  $R_{FB}$  is consistent with unity within uncertainties which means that even in high-energy p+Pb collisions, there is no significant difference between the production of the D mesons in the direction of the nucleus compared to the direction of the proton.

## 2.3 D Mesons in A+A Collisions

The installation of the Heavy Flavor Tracker into the STAR detector allowed for precise reconstruction of charmed meson decays in  $\sqrt{s_{NN}} = 200$  GeV Au+Au collisions, thanks to its unprecedented spatial resolution, and thus enabling the first reconstruction of  $D^\pm$  meson signal at STAR. The preliminary results were presented at the 2018 Quark

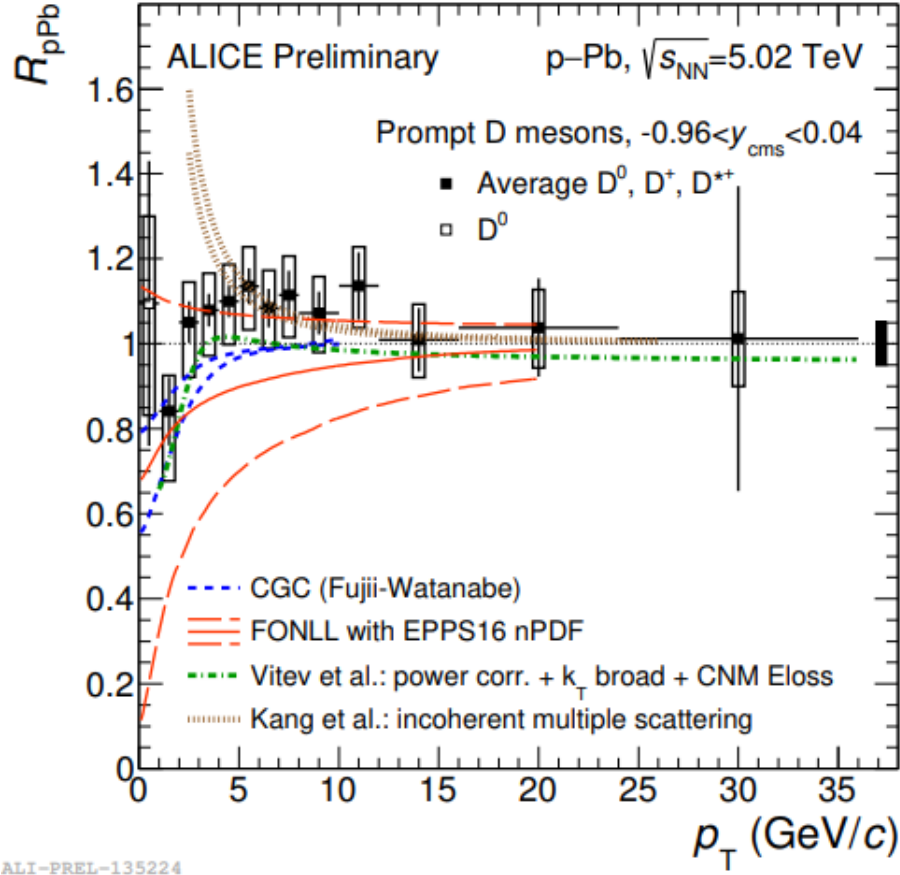


Figure 2.5: ALICE preliminary results of prompt D meson modification factor  $R_{pPb}$  in p+Pb collisions at  $\sqrt{s_{NN}} = 5.02$  TeV compared to 4 theoretical predictions. Taken from Ref. [54].

Matter conference [57]. The nuclear modification factor  $R_{AA}$  dependence on  $p_T$  for the 0-10 % most central collisions can be seen in Fig. 2.7. The results appear to be consistent with the STAR  $D^0$  results (also Fig. 2.8) throughout the measured range with the data showing increasing suppression towards higher  $p_T$  and a hint of a maximal  $R_{AA} \sim 0.7$  around  $p_T = 3$  GeV/c.

Figure 2.8 shows the STAR collaboration results from the measurement of  $D^0$  modification factors  $R_{AA}$  (left) and  $R_{CP}$  (right) as a function of  $p_T$  in Au+Au collisions at  $\sqrt{s_{NN}} = 200$  GeV. The results indicate increasing suppression with increasing centrality of the collision and (in central collisions) with increasing  $p_T$ . The comparison between  $D^0$  and light hadrons indicate lower suppression of charmed-meson production than light mesons - a behavior which is also predicted by the Duke model, which is based on quasielastic scatterings and the medium-induced gluon radiation [59] and the Linear Boltzmann Transport (LBT, [60]) model, which includes perturbative QCD calculations of elastic and inelastic medium interactions of jet shower partons and thermal partons. However, the level of suppression is similar at higher  $p_T$ .

The ALICE results of  $R_{AA}$  as seen in Fig. 2.9 indicate strong D meson production suppression in both central ( $R_{AA}$  reaching as low as 0.2) and mid-peripheral ( $R_{AA}$  as

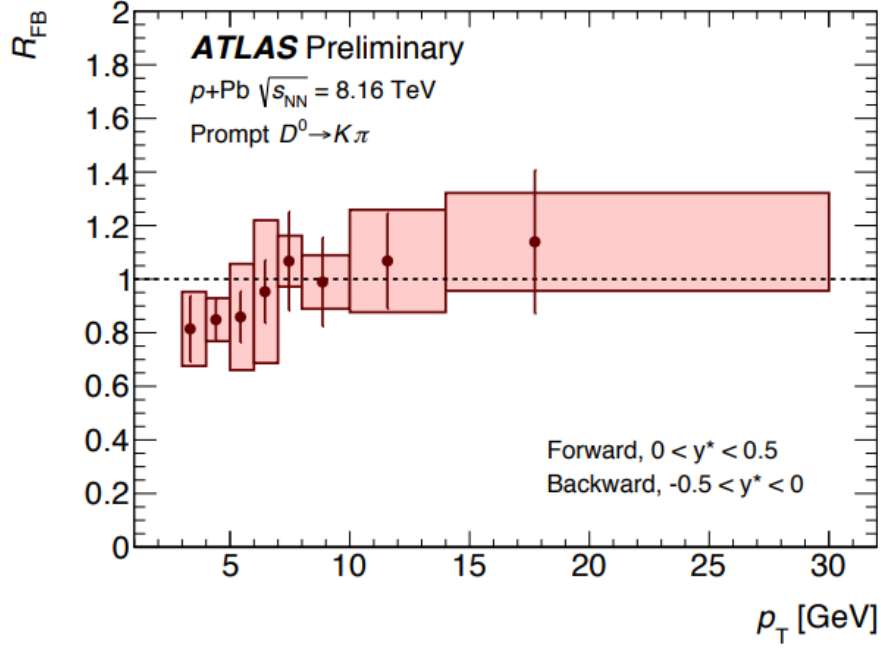


Figure 2.6: The  $R_{\text{FB}}$  for prompt  $D^0$  production as a function of  $p_{\text{T}}$  in  $2.5 < p_{\text{T}} < 30$   $\text{GeV}/c$  range as measured by the ATLAS collaboration. The forward region is in the direction of the proton while backward is in the direction of the nucleus after the collision. Taken from Ref. [56].

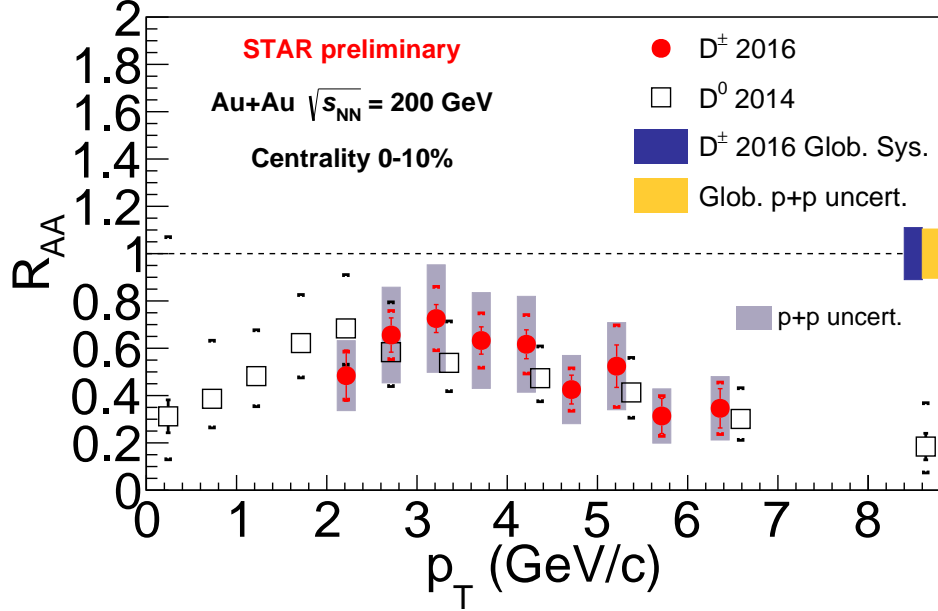


Figure 2.7: Preliminary results of  $D^\pm R_{\text{AA}}$  in 2016 Au+Au collisions at  $\sqrt{s_{\text{NN}}} = 200$   $\text{GeV}$  for centralities 0-10 % along with the results from  $D^0$  measurements conducted by the STAR collaboration. Taken from Ref. [57].

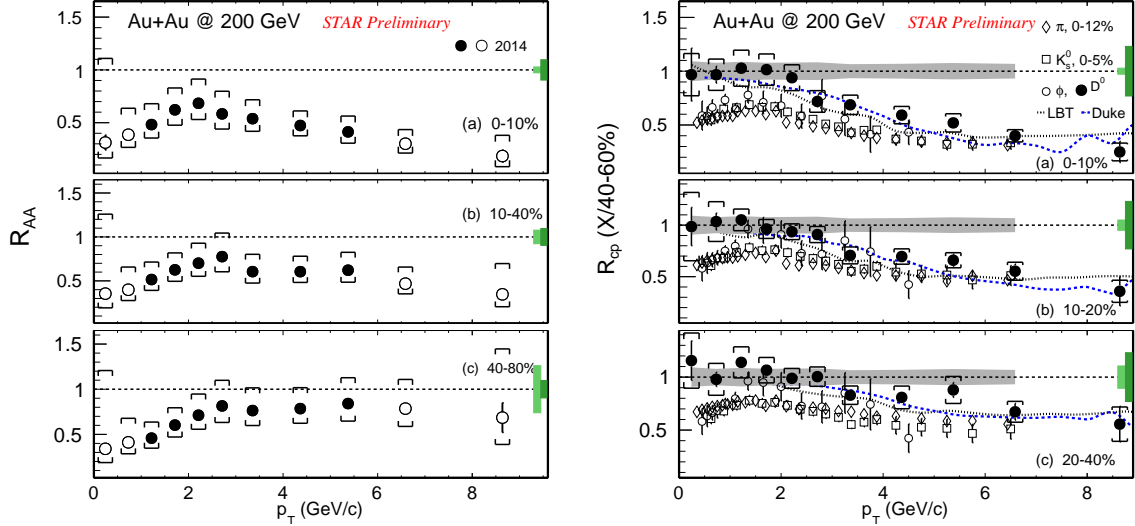


Figure 2.8: Left:  $D^0$  nuclear modification factor  $R_{AA}$  for central (a), mid-peripheral (b) and peripheral collisions (c) as a function of  $p_T$  as measured by the STAR experiment in 200 GeV Au+Au collisions. Right:  $D^0$  nuclear modification factor  $R_{CP}$  for three centrality bins: 0-10 % (a), 10-20 % (b) and 20-40 % (c) as a function of  $p_T$  as measured by the STAR experiment in 200 GeV Au+Au collisions, also shown are the results for light hadrons and the predictions of LBT and Duke models. Also shown is the systematic uncertainty of the Glauber model calculation of  $\langle N_{coll} \rangle$ . Taken from Ref. [58].

low as 0.4) Pb+Pb collisions at  $\sqrt{s_{NN}} = 2.76$  TeV. The maximal suppression occurs at approximately  $p_T = 10$  GeV/c in both cases.

The CMS results from Pb+Pb collisions at  $\sqrt{s_{NN}} = 5.02$  TeV are shown in Fig. 2.10. The left part shows the results from 0-100 % central collisions while the right part shows the 0-10 % centrality bin. Both centrality bins show great suppression when compared to p+p collisions with maximal suppression at  $p_T = 5 - 10$  GeV/c and the suppression is slightly greater in the most central collisions, which is expected since the most central collisions should produce the highest energy density and so on. This behavior is consistent with measurements from ALICE and STAR (although STAR does not cover the full  $p_T$  range of the LHC experiments and therefore does not see the minimum of  $R_{AA}$ ). The theoretical predictions seem to describe the data well, especially near the minimum for both centralities as seen in the upper part of the figure. The lower part of the figure offers a comparison of  $R_{AA}$  between  $D^0$  and charged hadrons,  $B^\pm$  mesons and nonprompt  $J/\psi$  mesons. The  $D^0$   $R_{AA}$  is compatible with the  $B^\pm$   $R_{AA}$  within rather large errors, but is significantly lower than the nonprompt  $J/\psi$  ( $B \rightarrow J/\psi$ )  $R_{AA}$  for  $p_T < 10$  GeV/c, which indicates that the energy loss of the b quark is even lower than of the c quark. The  $R_{AA}$  of the  $D^0$  is slightly higher than the charged hadrons  $R_{AA}$  in the low- $p_T$  region.

The STAR collaboration has presented their preliminary results from  $D^0$  meson flow measurements at the 2018 Quark Matter conference [62]. The results for  $v_1$  can

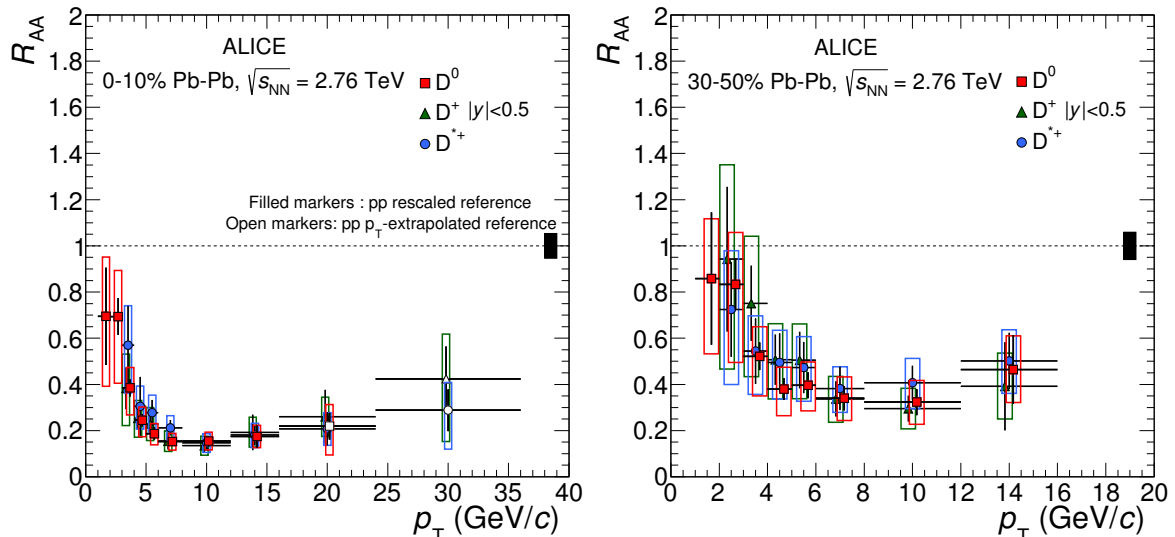


Figure 2.9: The ALICE experiment results of  $R_{AA}$  as a function of  $p_T$  for centralities 0-10 % (left) and 30-50 % (right) in  $\sqrt{s_{NN}} = 2.76$  TeV Pb+Pb collisions at mid-rapidity. Taken from Ref. [61].

be seen in Fig. 2.11 which shows that the directed flow of  $D^0$  and  $\bar{D}^0$  mesons is significantly higher than for charged kaons and also than the theoretical estimation from hydrodynamic model [63].

The elliptic flow has been experimentally confirmed by various STAR measurements and the preliminary results for  $D^0$  mesons were presented at 2018 Quark Matter conference (Fig. 2.12) compared to several theoretical models. The Duke model seems to describe the data very well within the uncertainties at higher  $p_T$ . The presence of a non-zero elliptic flow of the particles implies that the viscosity of the medium is low and, therefore, it can be treated as a near-perfect liquid.

The STAR collaboration preliminary results from their  $v_3$  measurements of  $D^0$  mesons in Au+Au collisions at  $\sqrt{s_{NN}} = 200$  GeV (Fig. 2.13) indicate that there is a significant triangular flow even for heavy mesons which is within uncertainties compatible with the flow of light mesons at the same energies.

The ALICE experiment has also presented their results of  $v_2$  measurement at the 2018 QM (Fig. 2.14), showing significant elliptic flow of D mesons in mid-peripheral collisions at  $\sqrt{s_{NN}} = 5.02$  TeV. Model calculations that provide a solid description of the measurement are LBT, MC@sHQ [68], PHSD [69] and POWLANG [70].

The CMS collaboration has also measured the elliptic flow of the  $D^0$  mesons in p+Pb and mid-peripheral Pb+Pb collisions at  $\sqrt{s_{NN}} = 8.16$  and 5.02 TeV respectively (Fig. 2.15 - left). A significant elliptic flow is observed in both types of collision indicating strong collectivity of the charm hadrons. When compared to strange hadrons, an expected mass and number-of-constituent-quarks ( $n_q$ ) ordering is observed. The results of  $v_2^{\text{sub}}$  as a function of  $p_T$  measurements in p+Pb collisions (upper left) have been corrected for residual jet correlations. There is a trend of rising and declining observed, which is consistent with the behavior observed at STAR (2.12). The elliptic

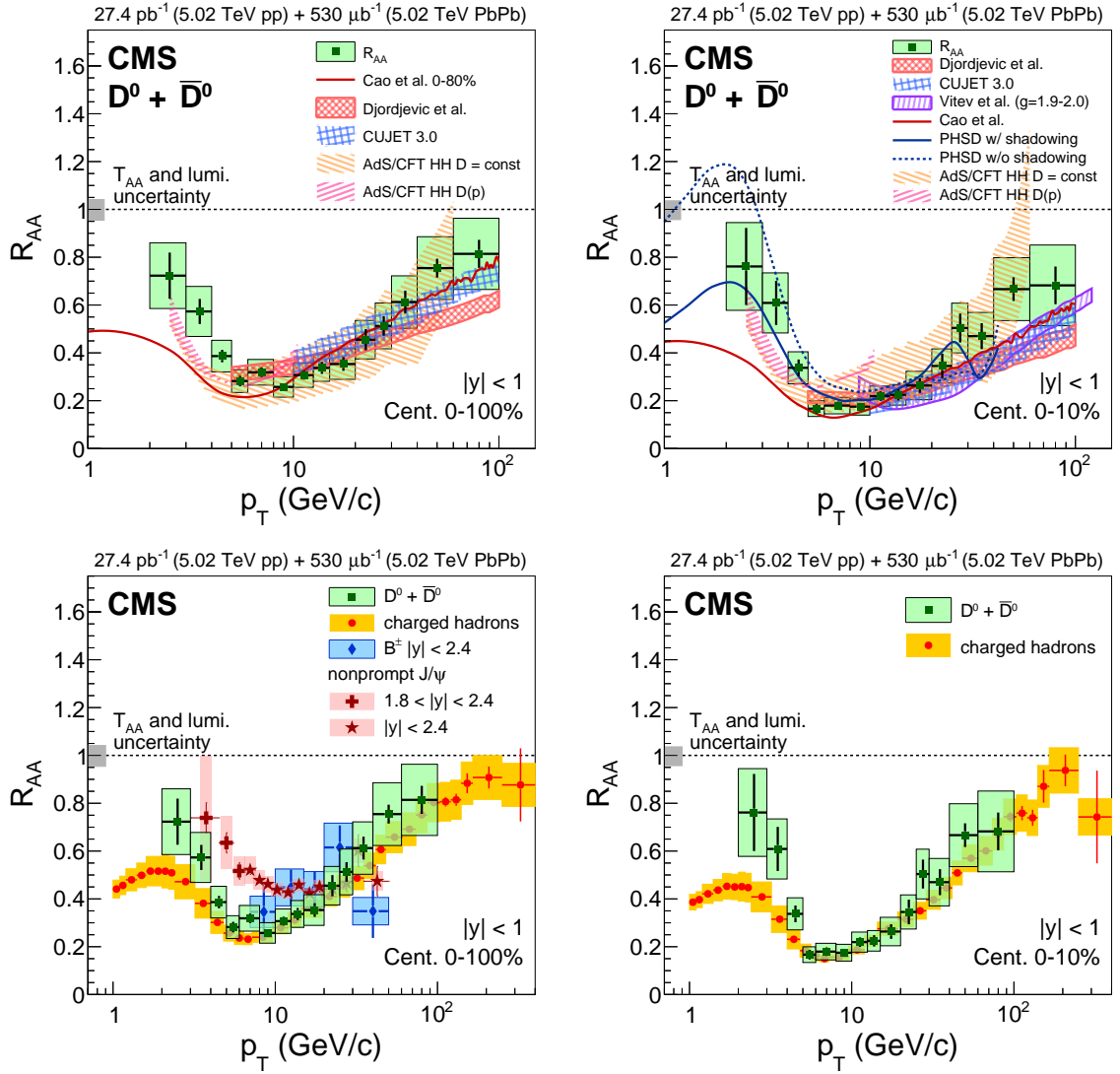


Figure 2.10: The  $R_{AA}$   $p_T$  dependence of  $D^0$  mesons as measured by the CMS collaboration in Pb+Pb collisions at  $\sqrt{s_{NN}} = 5.02$  TeV at mid-rapidity. The plots on the right are from the 0-10 % centrality bin while the plots on the left are from the 0-100 % centrality bin. The results are compared to theoretical predictions (top) and different particle species:  $B^\pm$ , charged hadrons and nonprompt  $J/\psi$  (bottom). Taken from Ref. [53].

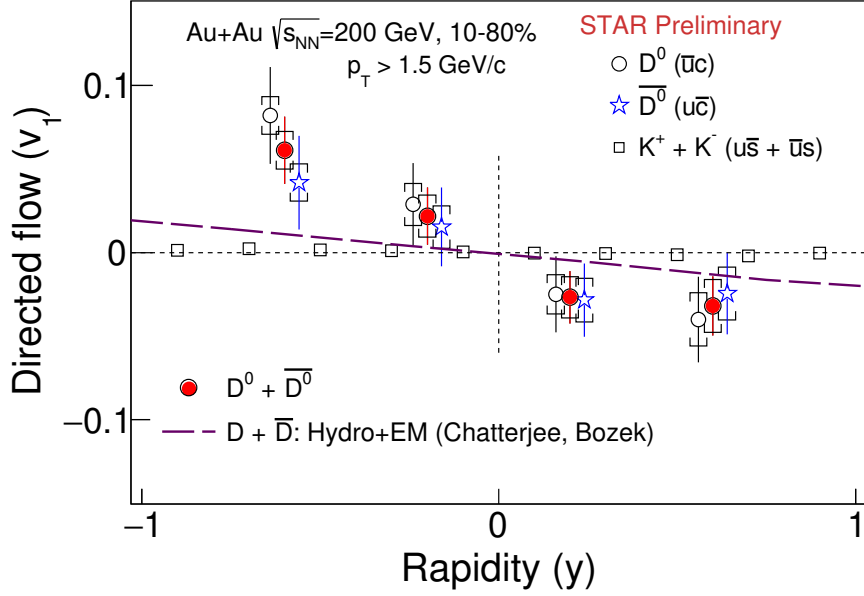


Figure 2.11: STAR measurement of  $D^0$  and  $\bar{D}^0$   $v_1$  as a function of rapidity (for  $p_T > 1.5$  GeV/ $c$  in 10-80 % Au+Au collisions at  $\sqrt{s_{NN}} = 200$  GeV, along with the average for  $D^0$  and  $\bar{D}^0$ , charged kaons  $v_1$  and hydrodynamic model calculation. Taken from Ref. [62].

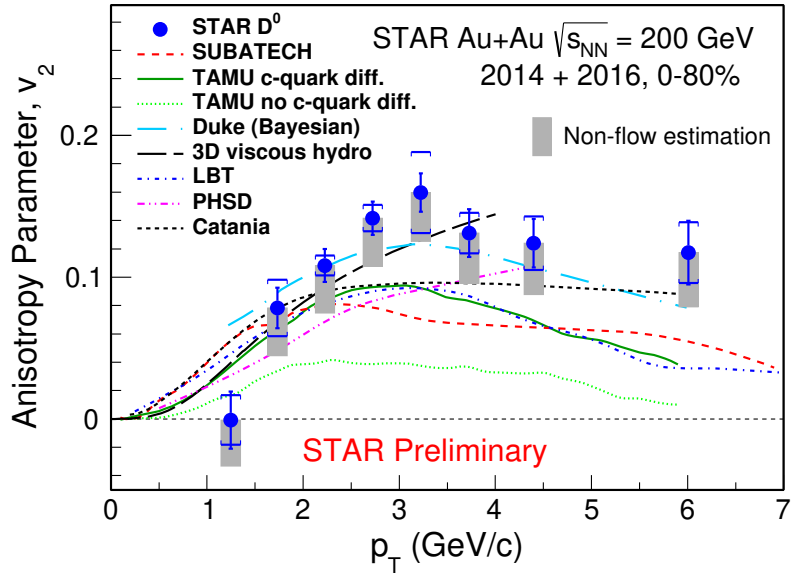


Figure 2.12: STAR results from  $D^0$   $v_2$  flow coefficient dependence on  $p_T$  in Au+Au collisions at  $\sqrt{s_{NN}} = 200$  GeV. The minimum-bias data are compared to several theoretical models including SUBATECH [64], TAMU [65] and Duke. Taken from Ref. [62].

flow coefficient per constituent quark as a function of transverse kinetic energy per

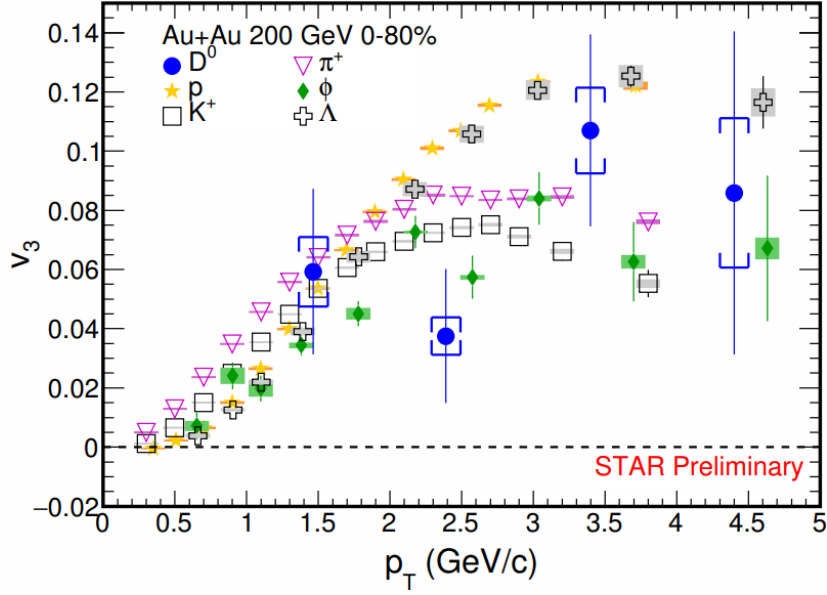


Figure 2.13: STAR preliminary results from the triangular flow  $v_3$  measurement for light hadrons and  $D^0$  mesons as a function of  $p_T$ . Significant triangular flow is observed for all types of particle. Taken from Ref. [66].

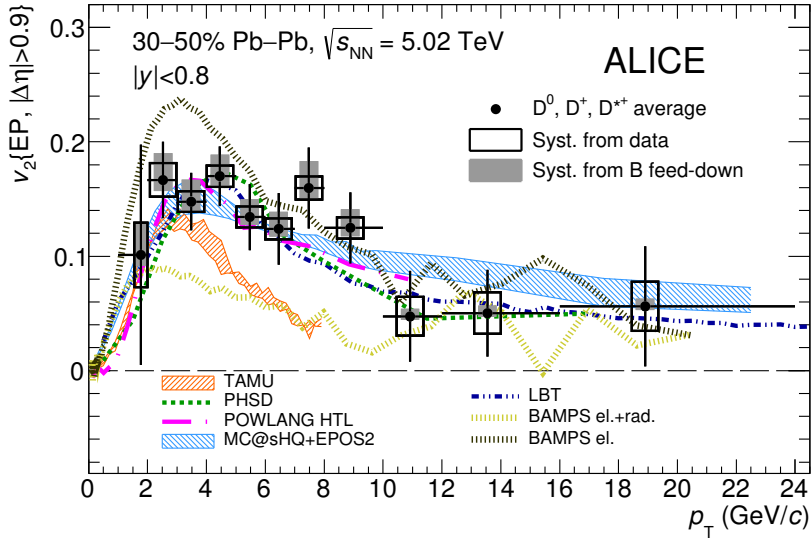


Figure 2.14: ALICE results of D meson elliptic flow in mid-peripheral Pb+Pb collisions at  $\sqrt{s_{NN}} = 5.02$  TeV at mid-rapidity compared to several theoretical predictions. Taken from Ref. [67].

constituent quark  $KE_T/n_q$ , where  $KE_T = \sqrt{m^2 + p_T^2} - m$  for D mesons and strange hadrons is shown in the right part of Fig. 2.15. While all particles follow a universal trend, the  $v_2^{\text{sub}}$  of  $D^0$  mesons is lower than for the strange particles in p+Pb collisions (top) which could be an indication that the charm quark collective behavior is weaker than the behavior of light quarks. There is no such difference observed in Pb+Pb collisions (bottom) indicating that the  $D^0$  observe the same collective behavior as the

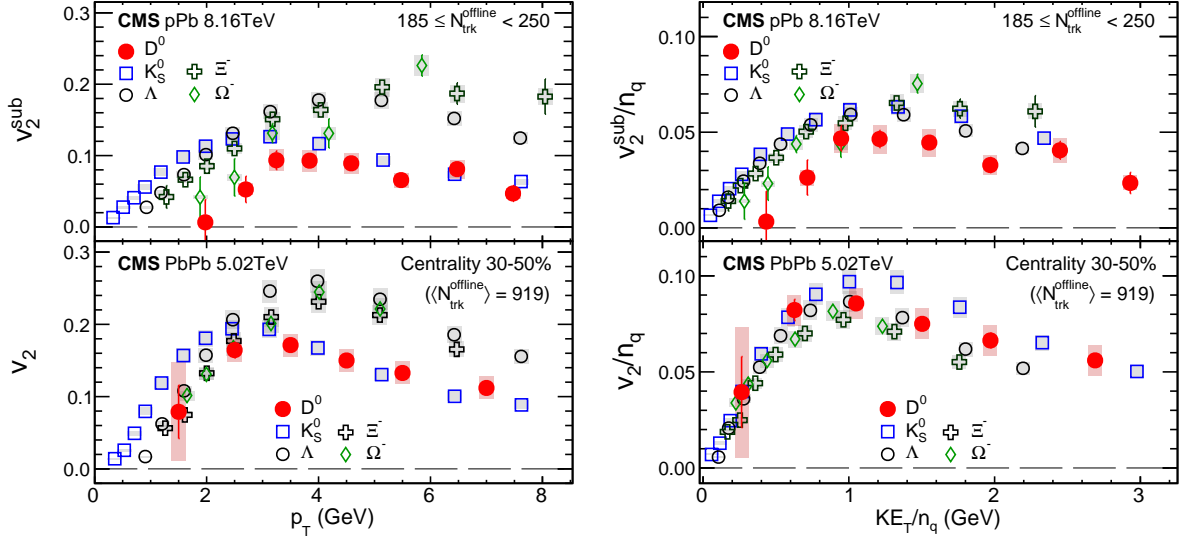


Figure 2.15: Left: Elliptic flow coefficient  $v_2$  as a function of  $p_T$  for  $D^0$  mesons as measured by the CMS experiment in p+Pb collisions at  $\sqrt{s_{NN}} = 8.16$  TeV (top, corrected for residual jet correlations) and Pb+Pb collisions at  $\sqrt{s_{NN}} = 5.02$  TeV compared to strange hadrons. Right: Elliptic flow coefficient  $v_2$  per constituent quark as a function of  $KE_T/n_q$  for  $D^0$  mesons as measured by the CMS experiment in p+Pb collisions at  $\sqrt{s_{NN}} = 8.16$  TeV (top, corrected for residual jet correlations) and Pb+Pb collisions at  $\sqrt{s_{NN}} = 5.02$  TeV compared to strange hadrons. Taken from Ref. [71].

lighter hadrons when the QGP is present.

Overall, the measurements at RHIC and LHC energies show that the production of D mesons in p+p collisions is understood within the pQCD framework. The production of D mesons is not suppressed in high-energy p+A collisions ( $R_{pA} \sim 1$ ) even though a significant collectivity of particles in these collision systems is observed. The D meson production is strongly suppressed in central A+A collisions at RHIC and the LHC ( $R_{AA} \sim 0.2$  for high- $p_T$  particles) which indicates significant energy loss of the c quark inside the QGP, similarly to light quarks. The measurements at STAR show surprisingly large directed flow of the D mesons, while the measurements of higher flow coefficients are consistent with the flow of lighter hadrons, which indicates, that the c quarks reach a thermal equilibrium inside the medium created in high-energy A+A collisions at RHIC and the LHC.

# Chapter 3

## STAR Experiment

Since the Quark-Gluon Plasma is a very extreme medium, we would naturally want to learn as much as possible about its properties and behavior. However, as far as it is known, there is no way to observe the QGP in the present Universe. Fortunately, we as humans found a way to create our own QGP in laboratory conditions. These little droplets of the QGP are created during ultrarelativistic heavy-ion collisions which can achieve sufficient energy density that the system resembles the Universe at the time of about 1 microsecond after the Big Bang. This is one of the main aims of the Relativistic Heavy Ion Collider (RHIC), which is located at the Brookhaven National Laboratory (BNL) on Long Island, NY and is the largest accelerator of the BNL accelerator complex (Sec. 3.1). The accelerator collides protons and/or heavy atomic nuclei (such as gold) at various energies and simulates the extreme conditions right after the Big Bang. Since there are hundreds of particles and antiparticles produced in each collision (event), a complex large-acceptance particle detectors are needed to detect as many of them as possible, identify them and trace them back to the point of their origin. The only currently operating experiment at RHIC is the Solenoidal Tracker At RHIC (STAR) experiment, which consists of many sub-detectors further described in Sec. 3.2.

### 3.1 BNL Accelerator Complex

The accelerator complex in the BNL used to ionize and accelerate heavy nuclei consists of the Laser Ion Source, the Electron Beam Ion Source, the Booster, the Alternating Gradient Synchrotron and RHIC. The entire complex is shown in Fig. 3.1.

#### 3.1.1 Pre-Accelerators

Before the atomic nuclei (for example gold) are collided in a heavy-ion collision, creating hundreds of new particles, they start their journey at the Laser Ion Source (LION), where an intense pulsed laser beam shines on a target (usually a metal foil), creating Au ions with +1 charge. These ions then travel from LION to the Electron Beam Ion Source (EBIS). Here, they are further ionized by an electron beam and sent to the

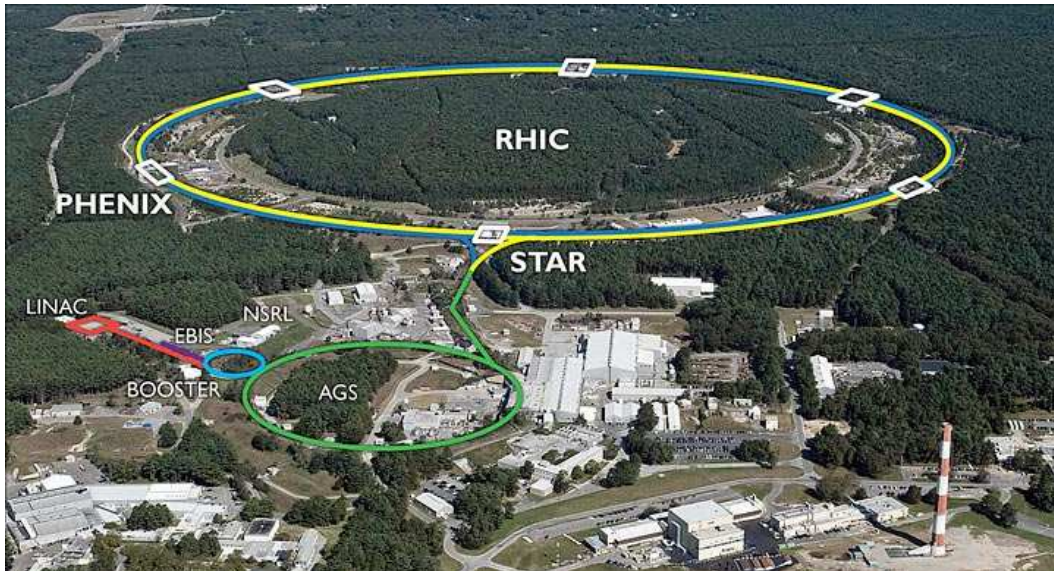


Figure 3.1: The BNL accelerator complex consisting of the Laser Ion Source (not marked), the Electron Beam Ion Source, multiple pre-accelerators and RHIC as the main accelerator. The position of STAR and PHENIX experiments is shown as well. Taken from Ref. [72].

Booster Synchrotron in one short pulse of approximately  $3.4 \times 10^9$   $\text{Au}^{32+}$  ions [73]. The ions are entering the Booster Synchrotron at  $E_{\text{kin}}/A = 2$  MeV and here they are further accelerated to 95 AMeV and organized into 24 bunches which are subsequently stripped to  $\text{Au}^{77+}$ . The bunches are then injected into the Alternating Gradient Synchrotron (AGS), where they are accelerated to 10.8 AGeV and re-bunched into 4 bunches. The nuclei are then finally fully ionized ( $\text{Au}^{79+}$ ) and transferred to RHIC via the AGS-to-RHIC beam pipe [74]. At the RHIC entrance, the bunches are split into smaller bunches and injected into one of the two RHIC rings by an electromagnetic switch and enter the final stage of the acceleration up to 100 AGeV. In total, 112 bunches can circulate inside RHIC, about twice the design value [75].

### 3.1.2 RHIC

The Relativistic Heavy Ion Collider is the only currently operating particle accelerator designed specifically to produce collisions of various systems and at various energies, which is essential for the studies of the QCD phase diagram (Sec. 1.1). Furthermore, RHIC is the only major accelerator capable of colliding polarized protons and therefore allowing for measurements crucial towards our understanding of the spin structure of the proton. It consists of two cocentric hexagonal synchrotrons (named blue and yellow) with a circumference of 3 834 meters, each of them used for acceleration and storage in the opposite direction. Four superconducting radiofrequency (RF) cavities, operating at 28.15 MHz are used for the acceleration and 10 storage cavities with a frequency of 197 MHz are used to keep the beams at the maximum energy throughout the beam storage [74]. An example of a superconducting RF cavity can be seen in Fig.

3.2. The cavity works on the following principle: an antenna excites the electric field inside the cavity, where it is trapped. When the input frequency is the same as the intrinsic frequency of the cavity (given by its shape), the resonance creates very intense electric field in the form of standing waves. When the charged particles of the bunch pass through the cavity, they are accelerated by this electric field. The oscillations are tuned so that particles, which arrive early will be accelerated less than those who arrive later, thus maintaining the bunch spacing and compactness.



Figure 3.2: Superconducting radiofrequency cavity operating at 700 MHz. Taken from Ref. [76].

Superconductive dipole magnets are used to curve the track of the particles along the beampipe and (also superconductive) quadrupole magnets are used for focusing the beam to achieve maximum luminosity (up to  $\sim 10^{27} \text{ cm}^{-2}\text{s}^{-1}$  for Au+Au collisions at  $\sqrt{s_{NN}} = 200 \text{ GeV}$  [77], which makes it the highest-luminosity heavy-ion collider in operation [78]). The RHIC average store nucleon pair luminosity ( $L_{NN} = A_1 A_2 L$ , where  $A_1$  and  $A_2$  are the nucleon numbers of the two colliding nuclei and  $L$  is the luminosity) for different systems (p+p, p+A and A+A) at different energies that were collided during its operation is summarized in Fig. 3.3.

After the RHIC rings are filled by the desired beams, they are accelerated to the top energy (100 AGeV for  $^{197}\text{Au}$ ). The beams can intersect at one of the 6 interaction points, which are marked the same way as numbers on a clock. Currently, the only place where the beams collide is the interaction point at 6 o'clock, where the STAR experiment is located (the other experiments PHOBOS and BRAHMS have finished their program and PHENIX is currently under a major construction upgrade - sPHENIX [79]). The beams can circulate inside the synchrotrons for several hours, producing new and new collisions which are then detected. However, the quality of the beam decreases with time and eventually reaches a level, where it is not suitable for data-taking anymore, so the beam is dumped by a kicker magnet into the beam dump and the entire process starts from the beginning. The beam can also be dumped in a case of emergency or due to the failure of any of the important components. The basic technical design specifications of RHIC are summarized in Tab. 3.1. RHIC is a unique machine filled with state-of-the-art technology, for more information about RHIC see for example [80], [81].



$\sqrt{s_{\text{NN}}} = 27$  GeV and also the first ever STAR fixed-target data from Au+Au collisions at 3.85 AGeV ( $\sqrt{s_{\text{NN}}} = 3.0$  GeV) and 26.5 AGeV ( $\sqrt{s_{\text{NN}}} = 7.2$  GeV) [78]. The BNL Program Advisory Committee has presented a series of recommendations for the near future of RHIC data taking program [82]. The runs during year 2019 will include collisions of gold nuclei at various low energies (see Tab. 3.2) and RHIC will fully enter the BES-II (see [8]), which will continue throughout the year 2021 and should lead to the confirmation of the critical point existence (the fixed-target experiments should cover the low- $T$ , high- $\mu_B$  region of the QCD phase diagram). The upgraded sPHENIX experiment should begin taking new data in 2023. The STAR experiment's program after the BES-II will probably focus on forward physics [82]. Long-term plans include a rebuild of the current RHIC into eRHIC, the world's first electron-ion collider ([83]) and upgrade/rebuild of the RHIC experiments correspondingly. This would open the door to all-new data and physics regarding the structure of protons and nuclei.

System	$\sqrt{s_{\text{NN}}}$ [GeV]	$N_{\text{MB}} \cdot 10^6$ [-]
Au+Au	19.6	400
Au+Au	14.5	300
Au+Au FT	3.9	100
Au+Au FT	4.5	100
Au+Au FT	7.7	100

Table 3.2: Collision systems (FT - fixed target), center-of-mass energy and the number of minimum-bias events planned for the RHIC Run 19. Taken from Ref. [82].

## 3.2 STAR Detector

The Solenoidal Tracker At RHIC (STAR) experiment is located at the 6 o'clock RHIC interaction point. It is a complex, large-acceptance multi-purpose particle detector consisting of many sub-detectors, such as the Time-Projection Chamber (TPC, Subsec. 3.2.1), which is used to identify particles by measuring their ionization energy losses and to track their flight path, the Time-of-Flight detector (TOF, Subsec. 3.2.2), which further helps identifying the particles by measuring their velocity, the Barrel Electromagnetic Calorimeter (BEMC, Subsec. 3.2.3), which measures the deposited energy of charged particles, the Vertex Position Detector (VPD, Subsec. 3.2.4) used for precise location of the primary vertex (the point of the collision) and the Heavy Flavor Tracker (HFT, Subsec. 3.2.5), which was installed between 2014 and 2016 and offered unprecedented accuracy in the reconstruction of secondary vertices related to heavy flavor decays. Another important part of the experiment is a 0.5 T solenoidal magnet which curves the path of the charged particles via the Lorentz force. The experiment has a cylindrical geometry, therefore offering a full azimuthal coverage, and is designed primarily for conducting measurements in the mid-rapidity ( $|y| < 1$ ) region, even though an extensive forward program is emerging as described in Subsec. 3.1.3. The entire STAR experiment can be seen in Fig. 3.4 with the magnet and key sub-detectors highlighted.

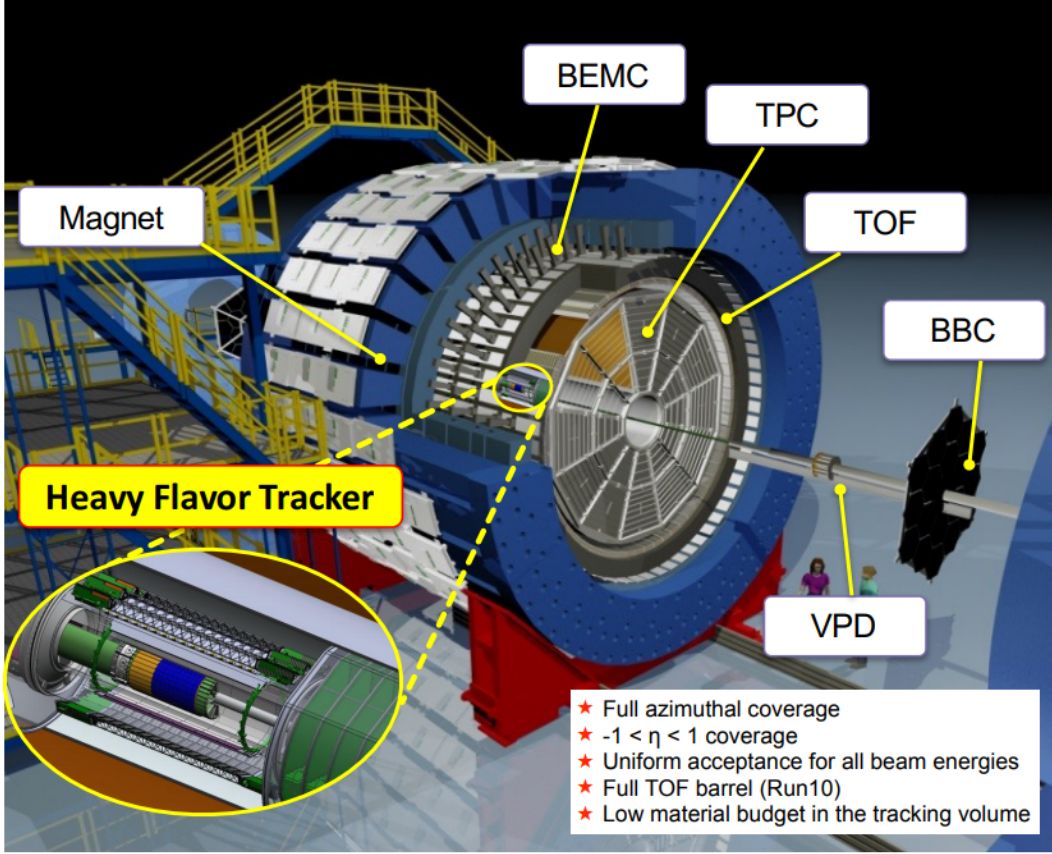


Figure 3.4: The STAR experiment schematic view. Main parts, including magnet, TPC, TOF, BEMC, VPD and HFT are highlighted. Taken from Ref. [84].

### 3.2.1 Time-Projection Chamber

The Time-Projection Chamber (TPC) of the STAR detector is its most important part as it allows tracking and identification of charged particles via their energy losses as a result of working gas ionization. The important value given by the TPC is

$$n_\sigma = \frac{\ln \frac{dE/dx}{\langle dE/dx \rangle}}{R_{dE/dx}}, \quad (3.1)$$

where  $dE/dx$  is an energy loss measured by the TPC,  $R_{dE/dx}$  is the TPC resolution and  $\langle dE/dx \rangle$  is a mean energy loss as given by the Bichsel function [85] for a given particle (Fig. 3.5). This value corresponds to the number of standard deviations from the theoretical energy loss we are still willing to tolerate for a given particle.

The TPC is a cylinder 4.2 m long and 4 m in diameter. It has a full azimuthal coverage and enables tracking in a pseudorapidity range of  $|\eta| < 1.0$ . The fill gas used is the P10 gas mixture (90 % argon - for ionization, 10 % methane - for quenching) kept at 2 mbar above the atmospheric pressure and the entire chamber is in a uniform electric field  $E = 135 \text{ V.cm}^{-1}$  created by a conductive membrane which splits the TPC into two halves. A charged particle passing through the TPC interacts with the gas,

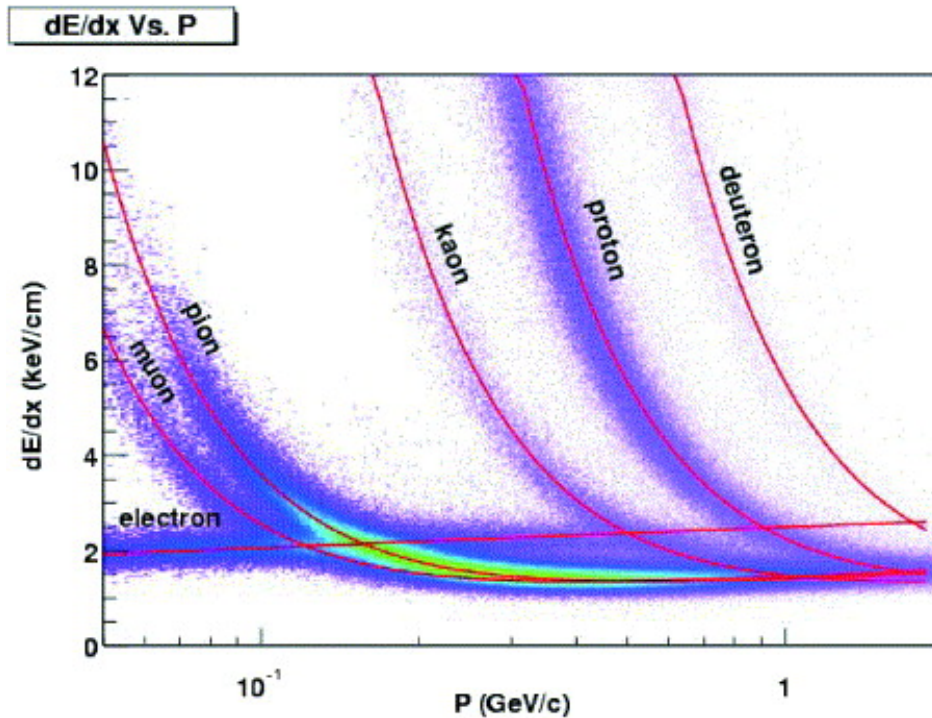


Figure 3.5: Energy loss as a function of particle momentum for common charged particles as measured by the STAR TPC. The Bichsel functions (corresponding to mean energy loss) are shown as the purple lines. Taken from Ref. [86].

creates electron-ion pairs and loses energy. The electrons then move towards the end caps. The end caps are divided into 12 sections further divided into inner and outer sectors, each containing a Multi-Wire-Proportional-Chamber-based read-out system. There, the electrons are amplified by a factor of 1000-3000 to create detectable signal and their drift time is measured. The typical electron drift velocity is about 5.45 cm/ $\mu$ s.

The TPC can measure the particle momentum in 100 MeV/ $c$  to 30 GeV/ $c$  range with momentum resolution down to  $\sim 2\%$ . All technical details of the STAR TPC were taken from Ref. [86]. The schematic view of the STAR TPC with key parts highlighted can be seen in Fig. 3.6 and a real Au+Au event at the top RHIC energy is shown in Fig. 3.7, demonstrating the excellent simultaneous tracking abilities of the TPC.

### 3.2.2 Time-of-Flight Detector

The STAR Time-of-Flight (TOF) detector helps with particle identification (PID) by measuring particle (inverse) velocities

$$\frac{1}{\beta} = c \frac{t - t_0}{\Delta s}, \quad (3.2)$$

where  $t$  is the incident time detected by TOF, the initial time  $t_0$  is given by the VPD (see Subsec. 3.2.4) and the particle path  $\Delta s$  is given by the TPC. Since we know the

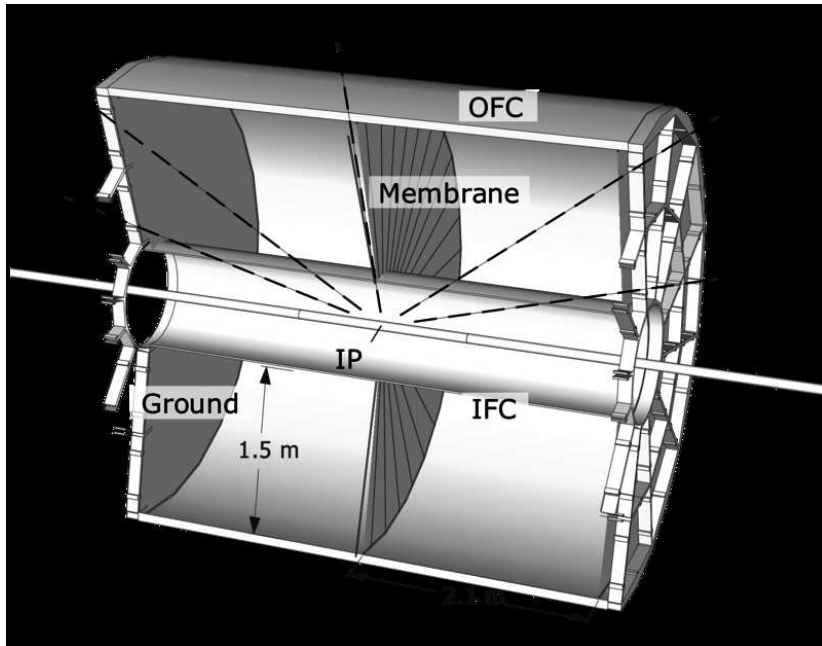


Figure 3.6: The STAR Time Projection Chamber schematic view with main features highlighted, including the Interaction Point (IP), the Inner Field Cage (IFC) and the Outer Field Cage (OFC). Taken from Ref. [87].

particle momentum  $p$  (again from the TPC), the particle mass can then be calculated using

$$m = \frac{p}{c} \sqrt{\left(\frac{1}{\beta}\right)^2 - 1}. \quad (3.3)$$

The measured inverse velocity is usually compared to the theoretical inverse velocity of the same particle with the same momentum  $\frac{1}{\beta_{\text{th}}}$ .

The TOF detector - consisting of 120 Multi-gap Resistive Plate Chamber modules (see Fig. 3.8) - measures time with a resolution of  $\sim 100$  ps. The detector is located between the TPC and the BEMC. Just as the TPC, it covers a full azimuthal angle and  $\eta < |1|$  pseudorapidity range [88]. The TOF detector serves as a complementary detector to the TPC, because it is effective in the high-momentum range ( $p > 1$  GeV/ $c$ ), where the TPC cannot distinguish between different kinds of particles (compare Fig. 3.5 and Fig. 3.9).

### 3.2.3 Barrel Electromagnetic Calorimeter

The Barrel Electromagnetic Calorimeter (BEMC) is used primarily for the identification of electrons and detection of high-energy particles which are the products of some rare hard processes (jets, direct photons, ...). The incident particle will interact with 5 mm thick lead layers and produce a shower which will be detected by a plastic

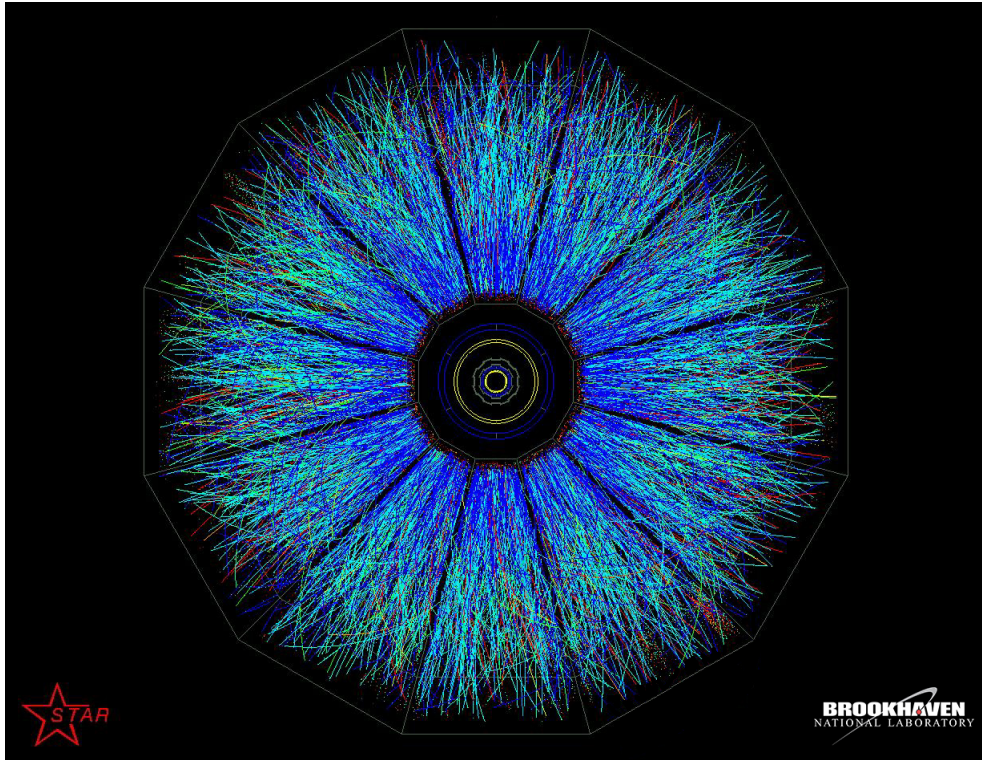


Figure 3.7: One of the first top energy Au+Au collisions at RHIC as detected by the STAR experiment. The colored lines are tracks detected by the TPC and captured by a 3D digital camera. Taken from Ref. [80].

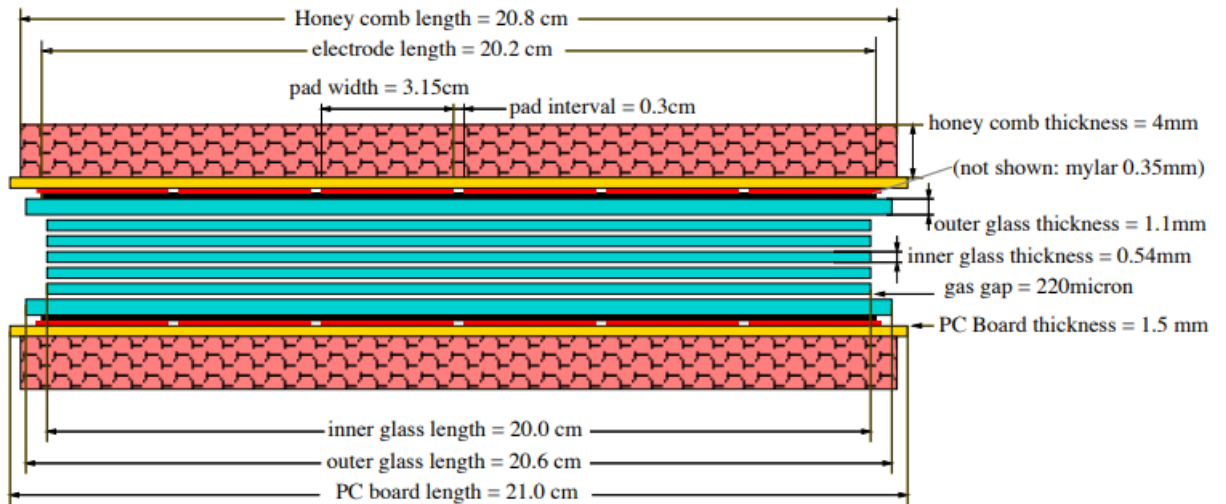


Figure 3.8: One module of the STAR Time-of-Flight detector. Taken from Ref. [88].

scintillator. Electrons tend to lose energy much easier than heavy particles during interactions and therefore will deposit almost all of their energy inside the BEMC. Thus, we can distinguish between electrons and other kinds of particles by measuring the  $E/p$  ratio, where  $E$  is the energy deposited inside the calorimeter and  $p$  is the momentum

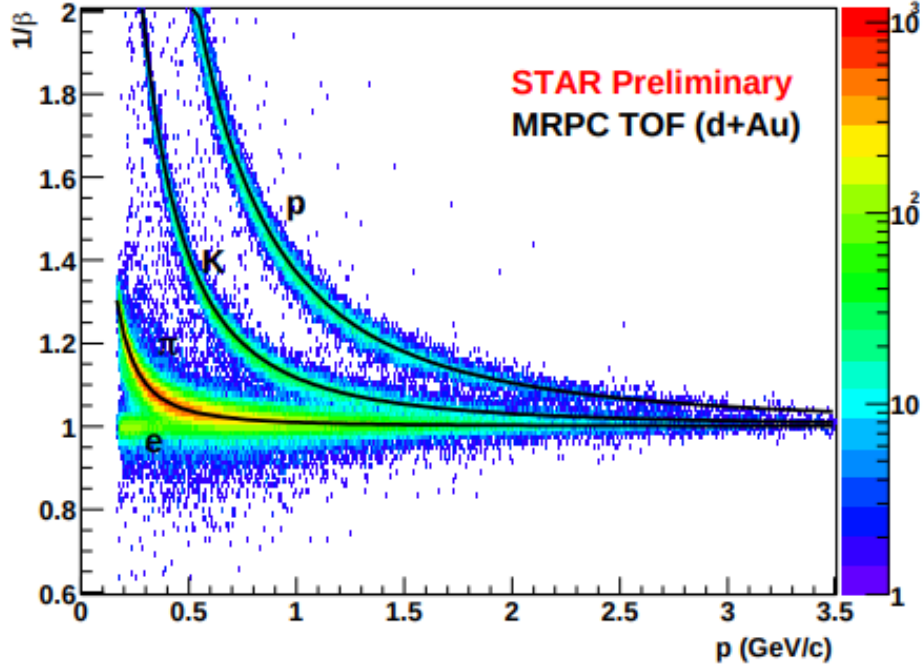


Figure 3.9: STAR Time-of-Flight detector measurement of inverse velocity  $1/\beta$  as a function of momentum  $p$  for different kinds of particles. Taken from Ref. [88].

as measured by the TPC. The calorimeter is composed of 120 modules further divided into 4800 towers each consisting of 20 layers of lead and 21 layers of plastic scintillator. The BEMC is located on the outside of the TOF detector, with inner radius of 2.2 m and outer radius of 2.6 m and matches the TPC coverage (full azimuthal angle and pseudorapidity range of  $\eta < |1|$ ). The energy resolution of the BEMC is about 17 % for 1.5 GeV electrons and about 10 % for 3 GeV electrons. All technical details were taken from Ref. [89]. An illustration of the STAR BEMC is shown in Fig. 3.10 and a side view of the BEMC module can be seen in Fig. 3.11.

### 3.2.4 Vertex Position Detector

Every detector system that uses time measurements needs a very fast trigger detector which can precisely measure the start time of the event and precisely locate the primary vertex. At STAR, this system is called the Vertex Position Detector (VPD), which has two identical parts, each located on one side of the STAR experiment, 5.6 m from the interaction point along the beampipe. Many  $\pi^0$  mesons are created during each heavy-ion collision and they decay almost immediately to photon pairs, which can then travel at the speed of light inside the beampipe. When these photons hit the Pb converter inside the VPD, they will produce charged particles which can be detected by the scintillating part of the VPD. Each VPD assembly contains 19 such detectors. The VPD assembly can be seen in Fig. 3.12.

The start time of the event (which is then used by other systems, such as TOF) is

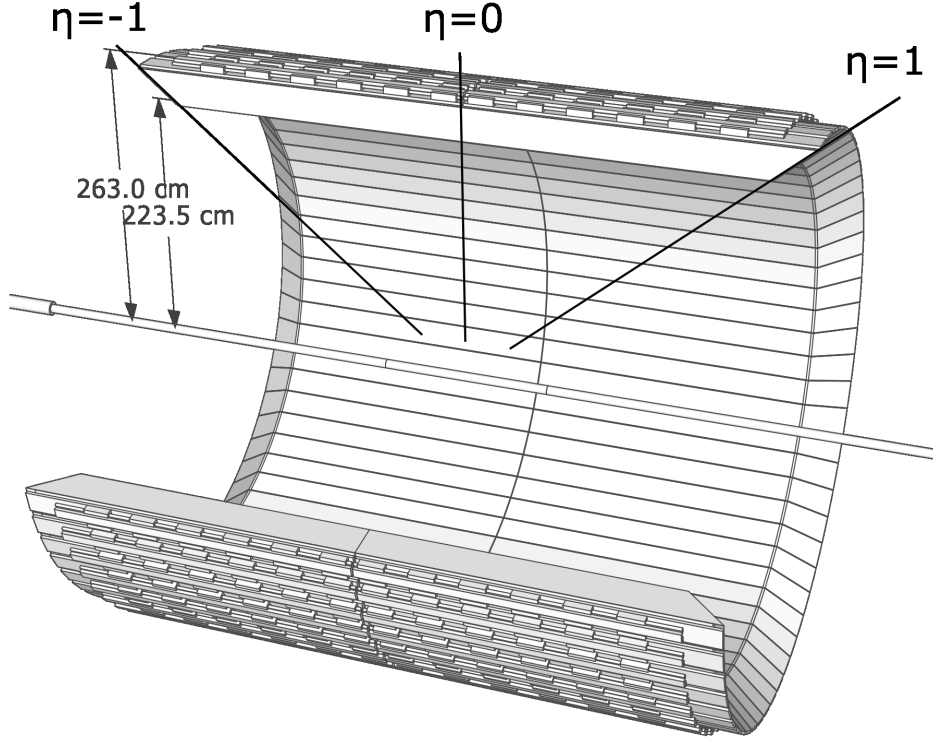


Figure 3.10: An illustration of the STAR Barrel Electromagnetic Calorimeter. Taken from Ref. [87].

calculated by

$$T_0 = (T_{\text{east}} + T_{\text{west}})/2 - L/c, \quad (3.4)$$

where  $T_{\text{east}}$  and  $T_{\text{west}}$  are the times from each of the VPD assemblies and  $L$  is their distance from the center of the STAR experiment. The event start time resolution is of the order of 0.1 ps. The position of the primary vertex is calculated from the following equation:

$$Z_{\text{PV}} = c(T_{\text{east}} - T_{\text{west}})/2 \quad (3.5)$$

and the detector achieves a resolution of 1 cm. The VPD also serves as a minimum-bias trigger for Au+Au collisions. For more technical details on the VPD see [90].

### 3.2.5 Heavy Flavor Tracker

The Heavy Flavor Tracker is a detector system which was installed between 2014 and 2016 and was located closest to the interaction point. The system is composed of 4 layers of silicon detectors in total - 2 Pixel detector (PXL) layers, the Intermediate Silicon Tracker (IST) and the Silicon Strip Detector (SSD). The HFT schematic view with the four silicon layers can be seen in Fig. 3.13.

The PXL detector consists of the 2 innermost layers located just 2.5 and 8 cm from

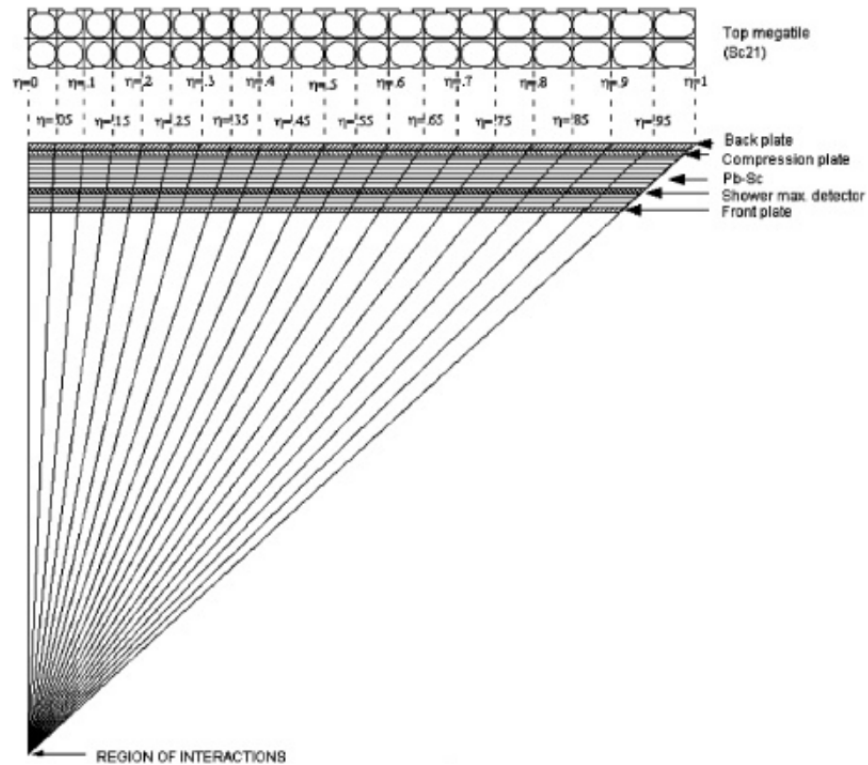


Figure 3.11: The side view of the STAR Barrel Electromagnetic Calorimeter module showing different  $\eta$  directions. Taken from Ref. [89].

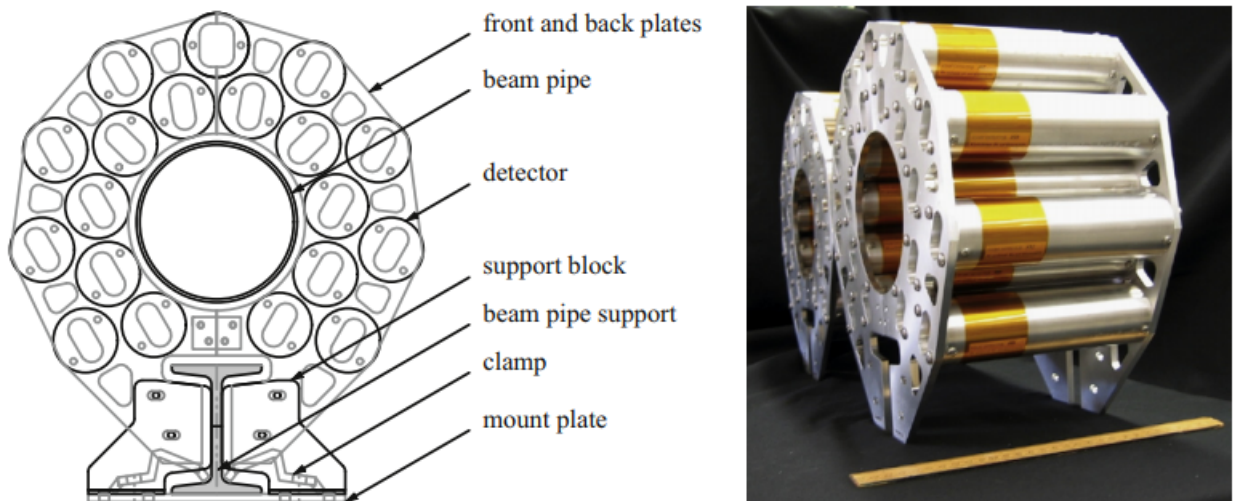


Figure 3.12: The STAR Vertex Position Detector. Left: Schematic front view. Right: a photo of the two VPD assemblies. A one-foot ruler is shown for comparison. Taken from Ref. [90]

the beampipe and is composed of 40 ladders each containing 10 monolithic CMOS chips (first-ever use of this technology in a collider experiment). The PXL detector can

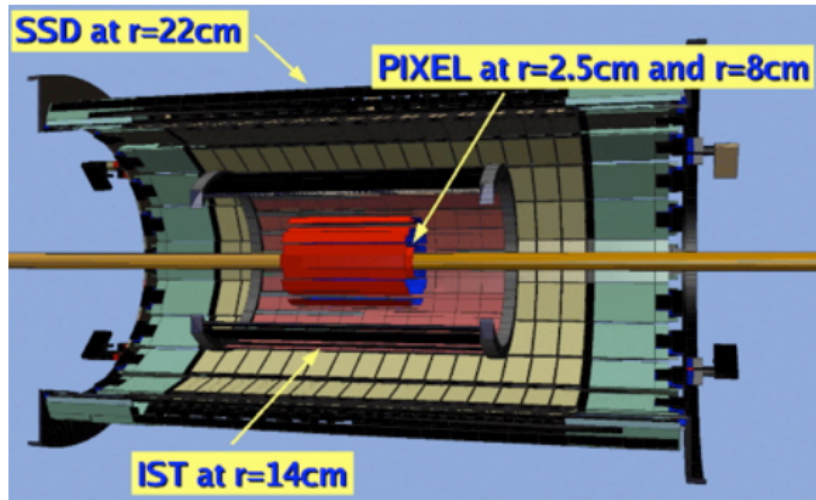


Figure 3.13: A schematic view of the Heavy Flavor Tracker at STAR. The four silicon detector layers are depicted. Taken from Ref. [91].

be seen in Fig. 3.14.

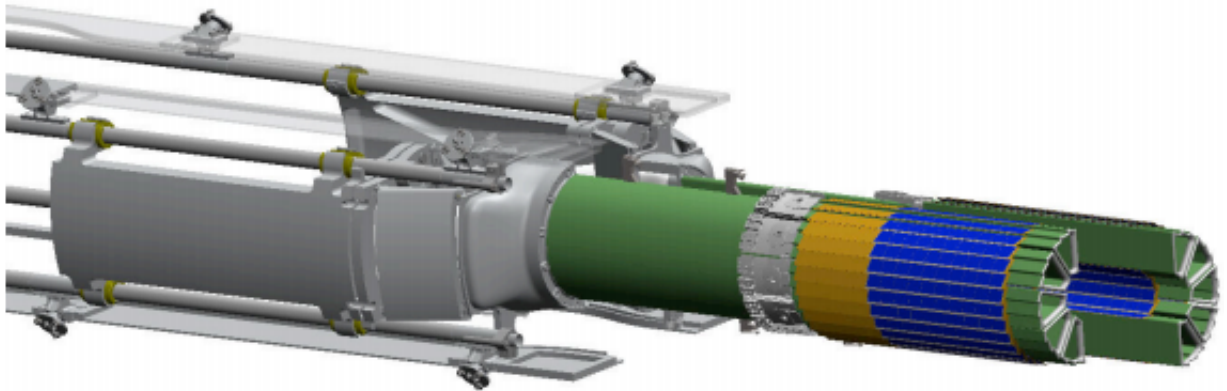


Figure 3.14: The model of the STAR HFT Pixel Detector, here shown with support and insertion structures. Taken from Ref. [91].

The third layer (IST) is made of silicon pad sensors and is located at a radius of 14 cm. As its name suggests, it serves as an intermediate detector which complements the tracking done by the PXL and the TPC. A computer-generated model of the IST can be seen in Fig. 3.15.

The outermost layer consists of double-sided Silicon Strip Detectors (SSD) mounted at a radius of 22 cm. This is midway the distance between the interaction point and the closest active region of the TPC, which makes it a great complementary detector which improves the tracking precision and momentum resolution of the TPC. A model of the SSD can be seen in Fig. 3.16.

The structure of the HFT detector and the usage of state-of-the-art technologies enables the system to achieve unprecedented tracking capabilities and pointing reso-

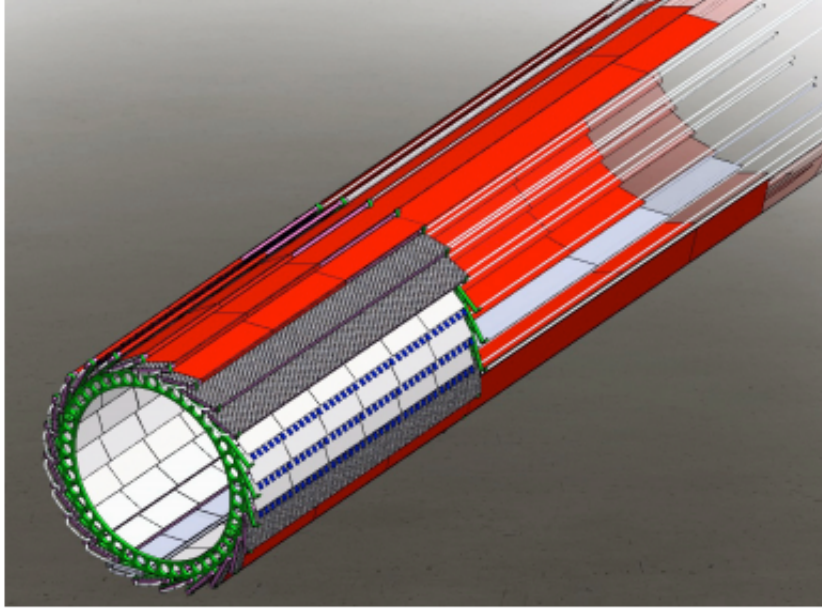


Figure 3.15: A computer model of the STAR HFT Intermediate Silicon Tracker. Taken from Ref. [91].

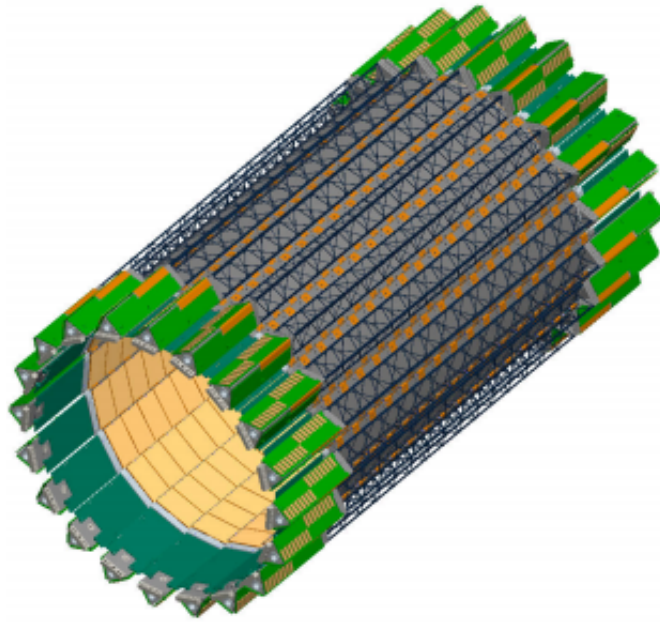


Figure 3.16: A computer model of the STAR HFT Silicon Strip Detector. Taken from Ref. [91].

lution of about  $46 \mu\text{m}$  for  $750 \text{ MeV}/c$  kaons (see Fig. 3.17 and [93]), which is crucial if we want to locate the secondary vertices created by decays of short-living heavy particles, such as  $D^\pm$  mesons, which have a mean decay length of  $c\tau = 312 \mu\text{m}$  or  $\Lambda_c^\pm$  baryons with  $c\tau = 60 \mu\text{m}$ . Because of the great spatial resolution, the HFT en-

ables selecting multiplets of decay products that come from the same vertex (but not the primary vertex) and these multiplets (doublets or triplets in most common decay cases) can then be classified as candidates for some heavy particle. Without the HFT, the combinatorial background (random combinations of common particles that come mostly from the primary vertex) for a three-body decay - which is the case with  $D^\pm$  and  $\Lambda_c^\pm$  - would be too high to obtain any significant signal from the data. Therefore, the installation of the HFT detector system enables first measurements of  $D^\pm$  and  $\Lambda_c^\pm$  production at STAR. These and many more technical details of the HFT can be found in [91].

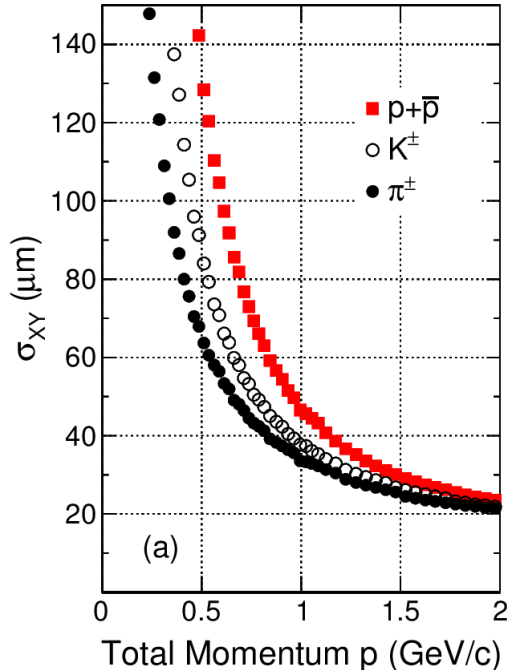


Figure 3.17: The HFT pointing resolution in the transverse plane  $\sigma_{xy}$  for pions (full circles), kaons (empty circles) and protons (squares) as a function of momentum  $p$ . Taken from Ref. [92].

### 3.2.6 Recent and Planned Upgrades

The STAR experiment has been continuously upgraded with new technologies in order to enable new measurements and to improve the precision of the existing measurements. Some of the recently installed detector systems include the Muon Telescope Detector (installed during years 2012-14 [94]), which allows for the detection of muons and therefore opens new decay channels to be used (for example in quarkonia measurements), the HFT described in Subsec. 3.2.5 and the Event Plane Detector (2017-18 [95]) which will allow to precisely measure the event plane and centrality in the forward region. Two new detector upgrades, which were tested during RHIC runs in 2018, were one sector of the inner TPC (iTTPC, [96]), which will improve the pseudorapidity acceptance and overall performance of the TPC, and one sector of the end-cap Time-of-Flight detector (eTOF, [97]), which will help with PID in the forward region. The author of this

thesis has assisted with the testing as a member of the STAR shift crew. The testing has been succesfull and full versions of these two detectors should be installed in the nearest runs. The future plans also include the installation of a forward calorimeter, which would be helpful during the planned fixed-target and forward physics program [98].

# Chapter 4

## Reconstruction of Charmed Mesons in Heavy-Ion Collisions

The analysis of  $D^\pm$  production in heavy-ion collisions, which is the main practical objective of this work, is presented in three chapters. This chapter focuses on the first stage of the analysis, which is the reconstruction of  $D^\pm$  meson signal from the available dataset (Sec. 4.1), that was obtained by the STAR experiment. The steps during this stage include the candidates selection (Sec. 4.2) and the raw yield extraction (Sec. 4.3). For the purpose of this analysis, since  $D^+$  and  $D^-$  mesons are antiparticles, they are reconstructed together to reduce statistical errors as their overall yield and reconstruction efficiency should be the same. For the reconstruction, we chose the  $D^\pm \rightarrow K^\mp + \pi^\pm + \pi^\pm$  decay channel, as is usual for the  $D^\pm$  analysis, since this is the decay channel with the highest branching ratio of all fully-hadronic decays of  $D^\pm$ , which are the easiest to analyze. Some key properties of the  $D^\pm$  meson are shown in Tab. 4.1.

Quark content	$c\bar{d}, \bar{c}d$
$m_{D^\pm}$ [MeV/ $c^2$ ]	$1869.5 \pm 0.4$
$\tau$ [ps]	$1.040 \pm 0.007$
$\lambda$ [ $\mu\text{m}$ ]	$312 \pm 2$
Decay channel	$D^\pm \rightarrow K^\mp \pi^\pm \pi^\pm$
$BR$ [%]	$8.98 \pm 0.28$

Table 4.1: Several basic properties of the  $D^\pm$  meson:  $m_{D^\pm}$  represents the  $D^\pm$  mass,  $\tau$  its mean lifetime,  $\lambda$  the mean decay length and  $BR$  is the decay channel branching ratio. Values taken from [1] and the mean decay length was calculated using  $\lambda = c\tau$ .

### 4.1 Dataset

For this analysis, we used data from RHIC runs with Au+Au collisions at center-of-mass energy per nucleon  $\sqrt{s_{NN}} = 200$  GeV during the year 2014 detected by the STAR experiment. This dataset was produced during production P16id with STAR library

version SL16d. Since these were minimum-bias (MB) data, the only required triggers were: 450050, 450060, 450005, 450015 and 450025. The data were stored in picoDst files, which contain only the most important information about the event and individual tracks. The picoDst files are produced during the third stage of data pre-analyzing from the MuDst data files which are in turn produced from the raw data collected during the process of data taking. In total, 1.33 billion MB events were available for this analysis.

## 4.2 Candidates Selection

The candidates selection consisted mainly of the application of several types of selection criteria (cuts) to identify correct events and tracks that could correspond to the decays of  $D^\pm$  mesons. As for event selection, we set the maximum distance of the primary vertex (PV) from the interaction point along the beampipe obtained from the TPC to  $|V_z| < 6$  cm and the maximum difference between the location of the PV given by the VPD and the TPC to  $|V_z - V_z^{\text{VPD}}| < 3$  cm. About 980 million events passed the event cuts (see Fig. 4.1), however, since the HFT efficiency was low (and too inconsistent to be determined precisely) for runs before day  $\sim 108$ , those runs were discarded and the number of events was reduced to about 880 million. Out of that number, about 20 million events did not have proper centrality defined and therefore were neglected. In the end, 859 246 464 MB events were used for the analysis.

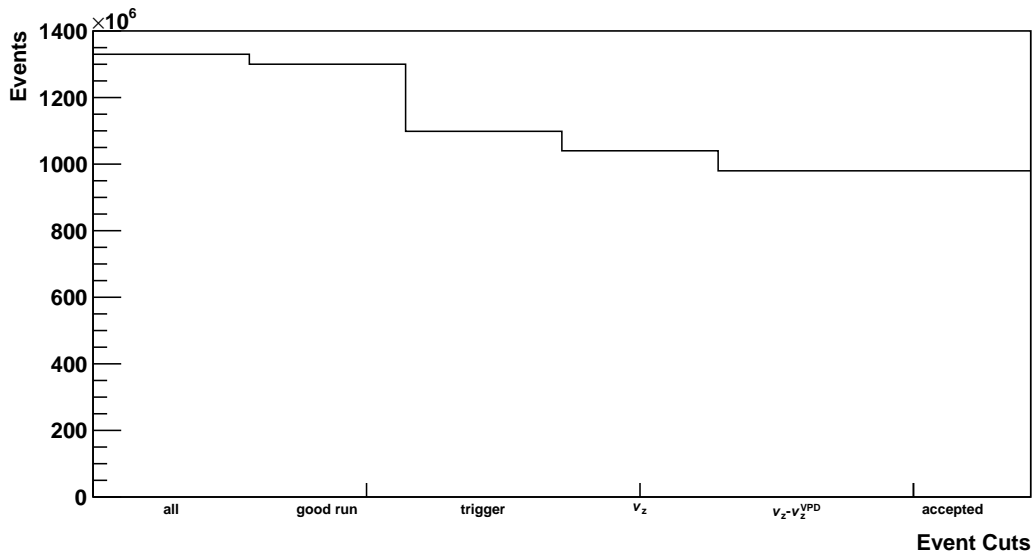


Figure 4.1: Number of events remaining after the application of event cuts. However, due to the low HFT efficiency during early runs and bad determination of centrality, additional  $\sim 120$  M events had to be discarded.

Once the good events had been selected, we conducted a good track quality check. For the track to be accepted, we required it to have hits in all 3 active HFT layers in use (2 PXL layers and the IST layer) and a minimum of 21 hits in the TPC. Because of the acceptance of the STAR detector, only tracks with  $|\eta| < 1$  were accepted.

As usual, the PID was done mainly by the TPC and - for improvement - we used the so-called hybrid TOF approach. When the track was correctly detected and identified by the TOF detector, we used both TPC and TOF information, otherwise only the TPC information was used to identify the particle. In the TPC, the particles are identified by their ionization energy loss and the cuts are set on the  $n_\sigma$  variable (see Subsec. 3.2.1). We set this cut to  $|n_\sigma| < 3$  for pions as this cut assures that almost no particles will be lost. However, we had to set the cut for kaons to  $|n_\sigma| < 2$  to prevent a contamination by other hadrons (mainly pions). Whenever the TOF information could be used, we set the cut for TOF PID to  $|\frac{1}{\beta} - \frac{1}{\beta_{\text{th}}}| < 0.03$  (see Subsec. 3.2.2) for both pions and kaons.

Once the tracks were accepted and identified, we combined them into  $K\pi\pi$  triplets and subsequently flagged them according to the charges of the daughter particles. There are 6 possible charge combinations. Two of them could be corresponding to decaying  $D^+$  ( $K^-\pi^+\pi^+$ ) or  $D^-$  ( $K^+\pi^-\pi^-$ ) mesons. These are referred to as correct-sign combinations while the others ( $K^+\pi^+\pi^-$ ,  $K^+\pi^+\pi^+$ ,  $K^-\pi^+\pi^-$  and  $K^-\pi^-\pi^-$ ) are called wrong-sign combinations and we use them to estimate the combinatorial background under the  $D^\pm$  signal peak, since we know that they do not originate from any particle decay. Simple combinatorics then tells us, that the number of  $K^+\pi^+\pi^-$  and  $K^-\pi^+\pi^-$  combinations will be twice as high as the other combinations. Therefore, we would expect the number of wrong-sign combinations to be approximately three times higher than the number of correct-sign combinations.

Since the  $D^\pm$  meson is fairly heavy and the  $p_T$  spectra of the daughter particles have maxima at around  $0.35 \text{ GeV}/c$ , we required the daughter particles to have  $p_T > 0.5 \text{ GeV}/c$  to significantly reduce the combinatorial background. The invariant mass of the triplets was calculated using the formula  $mc^2 = \sqrt{E_i^2 - |\vec{p}_i|^2 c^2}$ , where  $E_i$  are the energies of the detected particles and  $\vec{p}_i$  are the corresponding momenta. The mass range was restricted to  $1.7 < mc^2 < 2.1$ , around the expected  $D^\pm$  mass. We then located the secondary vertex (a place, where the D meson decayed into the daughter particles, see Fig. 4.2) using the distances of closest approach (DCA) between  $K\pi$  and  $\pi\pi$  pairs. Each pair of tracks has a vertex at the middle of the DCA between the two tracks. Since it is a three body decay, there are three such vertices creating a triangle. The secondary vertex is then located at the geometric center of this triangle. Thanks to the well-defined topology of the decay, we applied some loose topological pre-cuts to reduce the number of triplets and therefore the computational and storage requirements. These cuts include restrictions on the DCA between  $K\pi$  and  $\pi\pi$  pairs and the distance between the primary and secondary vertices - equal to the  $D^\pm$  meson decay length  $\lambda$ . These cuts were then tightened during the following yield extraction phase. The last applied cut in this stage was the pointing angle cut. The pointing angle is the angular difference between the reconstructed combined momentum vector direction and the line connecting primary and secondary vertices. The angle should be equal to zero to satisfy the law of conservation of momentum, however, that is not the case in real data due to the finite resolution of the STAR detector. Therefore, we set the cut to  $\cos\theta > 0.998$ . All triplets that passed these cuts are from now on referred to as ( $D^\pm$ ) candidates. Because of the geometry of the STAR experiment, these candidates were reconstructed at mid-rapidity ( $|y| < 1$ ), where  $y$  was calculated from the kinematics of the reconstructed  $D^\pm$  meson.

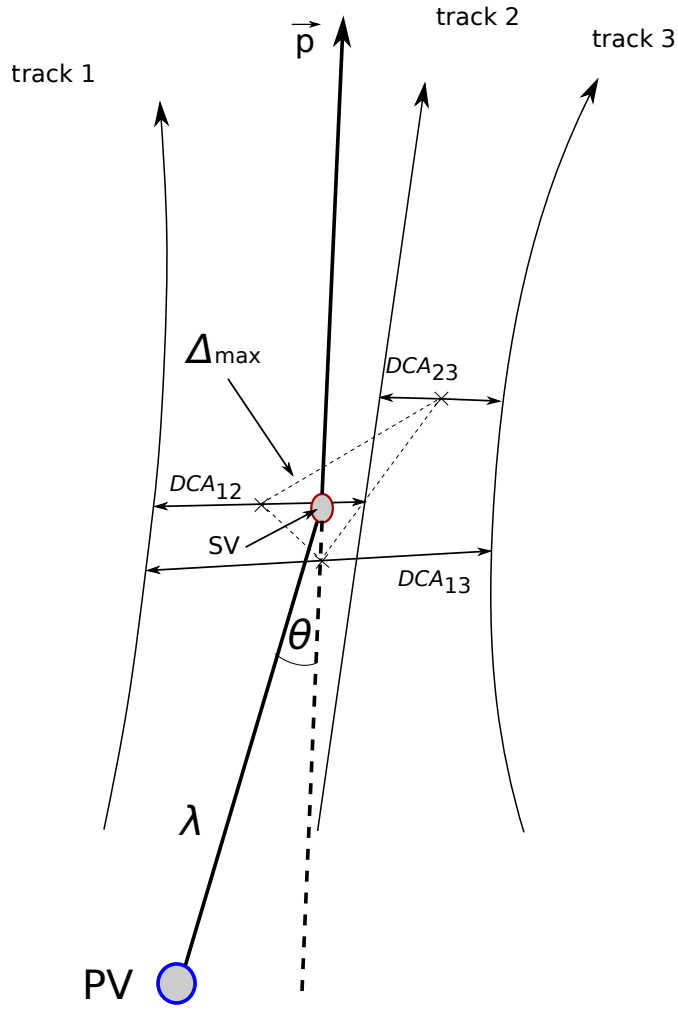


Figure 4.2: An illustration of the  $D^\pm$  three-body decay with important topological features highlighted: the combined reconstructed momentum of the tracks  $\vec{p}$ , the pointing angle  $\theta$ , the distance of closest approach between corresponding tracks  $DCA_{12,23,13}$ , the  $D^\pm$  meson decay length  $\lambda$  and the longest side of the vertex triangle  $\Delta_{\max}$ . The location of the primary vertex (PV) and the reconstructed secondary vertex (SV) is also illustrated.

### 4.3 Raw Yield Extraction

We then applied additional and tighter cuts to improve the discrimination between the signal and background candidates. The DCA of daughter particles to the PV was required to be  $DCA_\pi > 100 \mu\text{m}$  for pions and  $DCA_K > 80 \mu\text{m}$  for kaons to assure, that the daughter particles do not originate from the primary vertex. The maximum of DCA between any two daughter tracks was set to  $DCA_{\text{pair}} < 80 \mu\text{m}$  which is the best achievable resolution of the HFT. The last variable we used for the discrimination between signal and background combinations was the longest side of the vertex triangle

$\Delta_{\max}$  to be certain, that the secondary vertex was located with sufficient precision. Here, the cut was set to  $\Delta_{\max} < 200 \mu\text{m}$ . All the cuts are summarized in Tab. 4.2 and the corresponding distributions are shown in App. A. It should be mentioned that these cuts were chosen "by hand" using some assumptions about the decay, are not  $p_T$ - or centrality-dependent and are not tuned by any machine-learning technique. Cut tuning using machine learning will be discussed in Ch. 6.

Type	Cut	Value(s)
Event Selection	Primary vertex (PV) position	$ V_z  < 6 \text{ cm}$
	PV positions from TPC and VPD	$ V_z - V_z^{\text{VPD}}  < 3 \text{ cm}$
Track Selection	TPC Hits	$N_{\text{TPC}} > 20$
	HFT Hits	2 PXL and IST
	Pseudorapidity	$ \eta  < 1$
	Daughter transverse momentum	$p_T > 0.5 \text{ GeV}/c$
Particle Identification	TPC energy loss - pions	$ n_{\sigma}^{\pi}  < 3$
	TPC energy loss - kaons	$ n_{\sigma}^{\text{K}}  < 2$
	Particle flight time	$ \frac{1}{\beta} - \frac{1}{\beta_{\text{th}}}  < 0.03$
Topological Cuts	Daughter pairs DCA	$DCA_{\text{pair}} < 80 \mu\text{m}$
	Decay length	$30 < \lambda < 2000 \mu\text{m}$
	Maximum distance of pair vertices	$\Delta_{\max} < 200 \mu\text{m}$
	Pointing angle	$\cos \theta > 0.998$
	Pion DCA to PV	$DCA_{\pi} > 100 \mu\text{m}$
	Kaon DCA to PV	$DCA_{\text{K}} > 80 \mu\text{m}$

Table 4.2: Event, track, PID and topological cuts used to obtain the raw yield. The cuts are further described in the text. Related distributions (mainly for PID and topological cuts) can be found in App. A.

After all cuts were applied, some 407 thousand correct-sign combinations and about 1.2 million wrong-sign combinations remained. We then divided them into 13  $p_T$  and 3 centrality bins (and also studied the inclusive 0-80 % bin), since we are interested in the  $p_T$  spectrum and we want to compare the raw yield in different centralities. The next step towards the extraction of the raw yield was the scaling of the background so it can be subtracted to produce the invariant mass spectrum. For this purpose, we fitted the correct-sign distributions with a Gaussian + first-order polynomial function in the peak region, obtained the  $\sigma$  parameter of the Gaussian and counted the number of correct-sign ( $\#_{CS}$ ) and wrong-sign ( $\#_{WS}$ ) combinations using the bin counting method outside of the  $4\sigma$  range. We then scaled the background distributions by the correct-sign-to-wrong-sign ratio (which should be close to 1/3) and, finally, we subtracted the background from the correct-sign mass distribution to obtain the invariant mass distribution of the  $D^\pm$  signal.

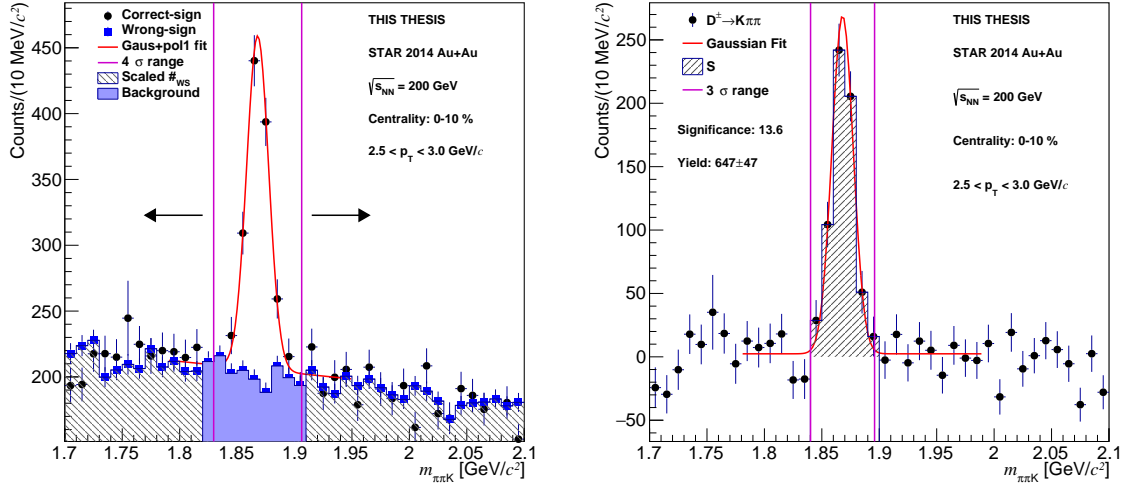


Figure 4.3: Left: invariant mass distribution of correct-sign (black circles) and scaled wrong-sign (blue squares)  $K\pi\pi$  triplets with a clearly visible peak fitted by a Gaussian + linear function. The magenta lines indicate the  $4\sigma$  range. The shaded area represents the scaled number of wrong-sign combinations outside this range and the blue area represents the scaled background under the peak. Right:  $K\pi\pi$  invariant mass distribution after the subtraction of scaled background, with a clearly observable peak around the expected  $D^\pm$  mass, fitted by a Gaussian + constant function. The shaded area represents the  $D^\pm$  raw yield and the magenta lines again represent the bin counting range. Both plots are made for the 0-10 % most central collisions in the  $2.5 < p_T < 3.0$  GeV/ $c$  bin.

To obtain the raw yield and significance, we then fitted the signal distribution with a Gaussian function with a constant offset (to approximate the residual background) and obtained the number of  $D^\pm$  mesons using the bin counting method inside the  $3\sigma$  range. This number ( $S$ ) is then equal to the raw yield, while significance can be calculated from:

$$\text{Sig.} = \frac{S}{\sqrt{S + \left(1 + \frac{\#_{CS}}{\#_{WS}}\right) B}}, \quad (4.1)$$

where  $B$  is the scaled number of background combinations inside the  $3\sigma$  range. The denominator of eq. 4.1 has this form as a result of propagation of errors from the correct-sign and wrong-sign distributions and is therefore equal to the raw yield statistical error. The factor  $\frac{\#_{CS}}{\#_{WS}} \approx \frac{1}{3}$  has to be included since the background is not determined precisely (this could be improved by using the mixed-event technique). The significance itself stands for the confidence level (expressed in standard deviations) that the observed peak is not resulting from random fluctuations, but rather is originating from a  $D^\pm$  meson decay. An example of the raw yield extraction can be seen in Fig. 4.3 for the  $2.5 < p_T < 3.0$  GeV/ $c$  bin for the 0-10 % most central collisions. Invariant mass distributions for all available bins are shown in App. B. Raw yields calculated for various  $p_T$  bins between  $p_T = 1$  GeV/ $c$  and  $p_T = 14$  GeV/ $c$  and for 4 centrality bins (0-10 %, 10-40 %, 40-80 % and 0-80 %) can be seen in Tab. 4.3 along with the corresponding significance of the peak. Bins, where Sig.  $< 3$  were dismissed as insignificant. The total yield of  $D^\pm$  mesons in the 0-80 % centrality bin and  $1.0 < p_T < 14.0$  GeV/ $c$  range is then  $11499 \pm 328$ .

$p_T$ [GeV/ $c$ ]	0-10 %		10-40 %		40-80 %		0-80 %	
	Yield [-]	Sig. [-]						
1.0-2.0	262±149	1.8	1091±168	6.5	314±33	9.6	1781±261	6.8
2.0-2.5	390±98	4.0	1442±82	17.6	397±23	17.4	2267±125	18.1
2.5-3.0	647±47	13.6	1493±55	27.3	422±22	19.5	2532±76	33.2
3.0-3.5	437±32	13.7	1106±39	28.2	349±19	18.2	1879±53	35.3
3.5-4.0	256±21	12.4	734±30	24.5	249±16	15.3	1245±40	31.4
4.0-4.5	160±17	9.6	441±23	19.5	151±13	11.9	754±30	25.1
4.5-5.0	79±10	7.6	277±18	15.2	100±11	9.3	456±24	19.3
5.0-5.5	54±9	6.0	170±14	12.1	60±9	6.9	283±19	15.3
5.5-6.0	30±6	4.9	96±11	9.0	29±6	4.9	154±14	11.2
6.0-7.0	22±6	3.6	96±10	9.2	30±6	5.1	153±14	11.3
7.0-8.0	11±3	3.2	28±6	4.5	12±3	3.5	49±8	6.3
8.0-10.0	2±3	0.6	16±5	3.3	4±4	1.2	22±7	3.2
10.0-14.0	-	-	-	-	5±3	1.7	-	-

Table 4.3: Raw yields of  $D^\pm$  meson for all used  $p_T$  and centrality bins along with corresponding peak significances. The corresponding plots can be found in App. B.

The mean of the Gaussian function used to fit the signal histogram should then be equal to the mass of the  $D^\pm$  meson ( $m_D = 1869.59$  MeV/ $c^2$ ) and the  $\sigma$  of the Gaussian corresponds to the  $D^\pm$  mass resolution. These values for all available centrality and transverse momentum bins in the 1-8 GeV/ $c$  range can be seen in Fig. 4.4 and Fig. 4.5 and are summarized in Tab. 4.4. The values of the offset are not very important - and therefore not shown - but generally are close to 0 for all bins with minimal value being -12.2 and maximal value +3.2 and the effect is (often significantly) less than 1 % for all relevant bins.

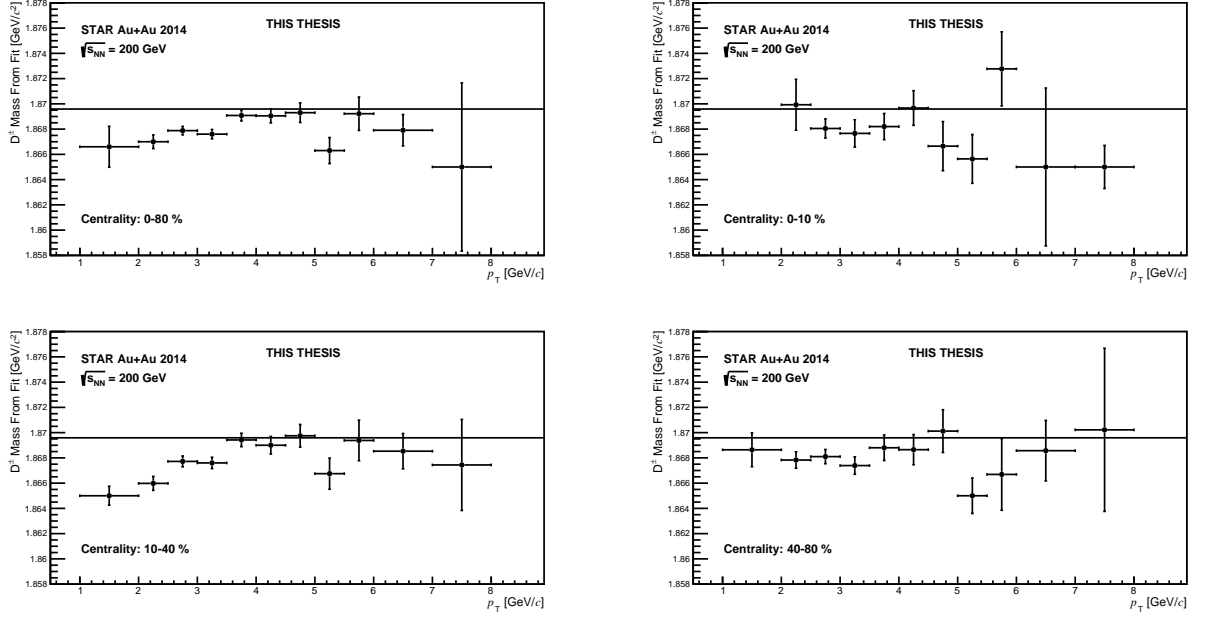


Figure 4.4:  $D^\pm$  mass obtained from fit of signal histogram for centralities 0-80 % (top, left), 0-10 % (top, right), 10-40 % (bottom, left) and 40-80 % (bottom, right) for all available transverse momentum bins. The solid black line at  $1.86959 \text{ GeV}/c^2$  indicates the  $D^\pm$  mass presented in [1].

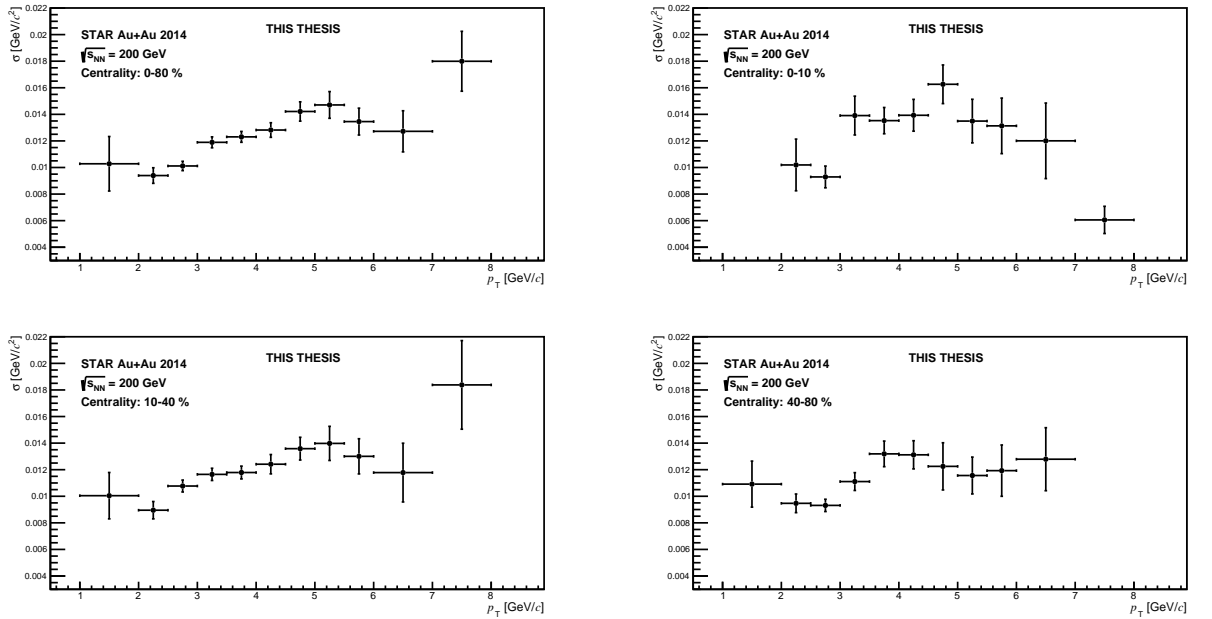


Figure 4.5:  $D^\pm$  mass resolution  $\sigma$  obtained from the fit of signal histogram for centralities 0-80 % (top, left), 0-10 % (top, right), 10-40 % (bottom, left) and 40-80 % (bottom, right) for all transverse momentum bins in the  $1-8 \text{ GeV}/c$  range.

$p_T$ [GeV/c]	0-10 %		10-40 %		40-80 %		0-80 %	
	$m_D$ [GeV/c <sup>2</sup> ]	$\sigma$ [GeV/c <sup>2</sup> ]						
1.0-2.0	-	-	1.8650±0.0007	0.010±0.002	1.869±0.001	0.011±0.002	1.866±0.002	0.010±0.002
2.0-2.5	1.870±0.002	0.010±0.002	1.8660±0.0006	0.0090±0.0007	1.8678±0.0006	0.0095±0.0007	1.8670±0.0005	0.0091±0.0006
2.5-3.0	1.8681±0.0008	0.0093±0.0008	1.8677±0.0004	0.0108±0.0004	1.8681±0.0006	0.0093±0.0005	1.8679±0.0003	0.0101±0.0004
3.0-3.5	1.868±0.001	0.014±0.001	1.8676±0.0004	0.0116±0.0005	1.8674±0.0007	0.0111±0.0007	1.8676±0.0004	0.0112±0.0004
3.5-4.0	1.868±0.001	0.0135±0.0010	1.8694±0.0005	0.0118±0.0005	1.869±0.001	0.0132±0.0010	1.8691±0.0004	0.0123±0.0004
4.0-4.5	1.870±0.001	0.014±0.001	1.8690±0.0007	0.0124±0.0007	1.869±0.001	0.031±0.001	1.8691±0.0006	0.0128±0.0005
4.5-5.0	1.867±0.002	0.016±0.001	1.8698±0.0009	0.0136±0.0009	1.870±0.002	0.012±0.002	1.8693±0.0008	0.0142±0.0007
5.0-5.5	1.866±0.002	0.013±0.002	1.867±0.001	0.014±0.001	1.870±0.001	0.012±0.001	1.866±0.001	0.015±0.001
5.5-6.0	1.873±0.003	0.013±0.002	1.869±0.002	0.013±0.001	1.867±0.003	0.012±0.002	1.869±0.001	0.013±0.001
6.0-7.0	1.865±0.006	0.012±0.003	1.869±0.001	0.012±0.002	1.869±0.002	0.013±0.002	1.868±0.001	0.013±0.002
7.0-8.0	1.865±0.002	0.006±0.001	1.867±0.004	0.018±0.003	1.870±0.006	0.05±0.02*	1.865±0.007	0.018±0.002

Table 4.4:  $D^\pm$  meson mass  $m_D$  obtained from fit and the mass resolution  $\sigma$  for various transverse momentum and centrality ranges. The values are also shown in Fig. 4.4 and Fig. 4.5. \* - not shown in plot.

# Chapter 5

## Yield Correction & Results

This chapter focuses mainly on the corrections of the raw yield (see Ch. 4) and the steps necessary to obtain the  $p_T$  spectrum and the nuclear modification factor of the  $D^\pm$  mesons. These steps are necessary, since the raw yield depends on many factors, such as the number of analyzed events, the efficiency of the  $D^\pm$  meson reconstruction - caused by the imperfection of the detectors - and the decay channel used, to be able to compare the results to results from other datasets and/or experiments. Therefore, we want to calculate the invariant yield using the following formula:

$$\frac{1}{2\pi p_T} \frac{d^2N}{dp_T dy} = \frac{1}{2\pi p_T} \frac{Y_{\text{raw}}}{N_{\text{ch}} \cdot N_{\text{evt}} \cdot BR \cdot \Delta p_T \cdot \Delta y \cdot \text{Eff}(p_T)}, \quad (5.1)$$

where  $Y_{\text{raw}}$  is the raw yield in a given  $p_T$  and centrality bin,  $N_{\text{ch}} = 2$  is the number of different meson charges (+, -),  $N_{\text{evt}}$  is the number of events analyzed for a given centrality (see Tab. 5.1) corrected by the reference multiplicity,  $BR = (8.98 \pm 0.28) \%$  is the  $D^\pm \rightarrow K^\mp + \pi^\pm + \pi^\pm$  decay branching ratio,  $p_T$  is the first estimation of the center of the  $p_T$  bin (which is a subject to correction, see Sec. 5.2),  $\Delta p_T$  is the  $p_T$  bin width,  $\Delta y = 2$  is the rapidity interval size and  $\text{Eff}(p_T)$  is the STAR detector's acceptance $\times$ efficiency factor (see Sec. 5.1).

Centrality [%]	$N_{\text{evt}}$ [-]
0 – 10	102 916 176
10 – 40	320 439 616
40 – 80	435 890 688
0 – 80	859 246 464

Table 5.1: Number of Au+Au events (corrected by the reference multiplicity) at  $\sqrt{s_{\text{NN}}} = 200$  GeV from year 2014 analyzed for each centrality bin.

### 5.1 Detector Acceptance $\times$ Efficiency

The information about the STAR detector's geometrical acceptance (see Sec. 3.2) and the efficiency of each detector subsystem that was used in the analysis of the

$D^\pm \rightarrow K^\mp + \pi^\pm + \pi^\pm$  decay channel in Au+Au collisions (HFT, TPC, TOF - when available) is included in the  $Eff(p_T)$  normalization factor. To obtain the  $Eff(p_T)$  values, a data-driven fast simulator (FastSim) has been developed. The FastSim, which uses PYTHIA [99] and/or EvtGen [100], works in the following steps:

- Obtain the  $V_Z$  distribution (from data).
- Generate  $D^\pm$  mesons flat in  $p_T$  and rapidity and then let them decay to daughter particles via the same decay channel as was used for this analysis.
- Smear the momentum according to TPC resolution (from K and  $\pi$  embedding).
- Smear the distributions of  $DCA$  for daughter particles (from data).
- Apply HFT matching efficiency (from data).
- Apply TPC reconstruction efficiency (from K and  $\pi$  embedding)
- Reconstruct the  $D^\pm$  mesons with the analysis cuts.

The FastSim has been validated by a full HIJING+Geant4 simulation [101, 102] and the results differ by less than 5 %, so this value is therefore taken as the overall  $Eff(p_T)$  systematic error. The efficiency points are then obtained as a simple ratio of generated and reconstructed  $D^\pm$  mesons in each  $p_T$  and centrality bin. However, since the default centrality bins used for the simulation are different from the analysis centrality bins, we had to re-scale the points by the mean number of binary collisions in the default centrality bins (see Tab. 5.2).

Centrality [%]	$N_{\text{coll}}$ [-]
0 – 5	$1066.5 \pm 27.8$
5 – 10	$852.8 \pm 23.4$
10 – 20	$606.9 \pm 30.6$
20 – 30	$375.9 \pm 33.4$
30 – 40	$222.6 \pm 30.3$
40 – 50	$124.0 \pm 24.6$
50 – 60	$64.0 \pm 17.8$
60 – 70	$30.6 \pm 11.4$
70 – 80	$13.7 \pm 6.2$

Table 5.2: The mean number of binary collisions in each centrality bin obtained from the Monte Carlo Glauber model [12] for Au+Au collisions at  $\sqrt{s_{\text{NN}}} = 200$  GeV. Centrality from 80 to 100 % is so poorly defined, that it is not shown here and also not used for the analysis.

The  $Eff(p_T)$  points obtained from the FastSim can be seen in Fig. 5.1 for all 4 centrality bins and we can see that the efficiency is the highest for the peripheral collisions and in the high- $p_T$  range. Since the  $Eff(p_T)$  binning in  $p_T$  was the same as the analysis binning, there was no need to fit the points, which would introduce additional errors into the analysis.

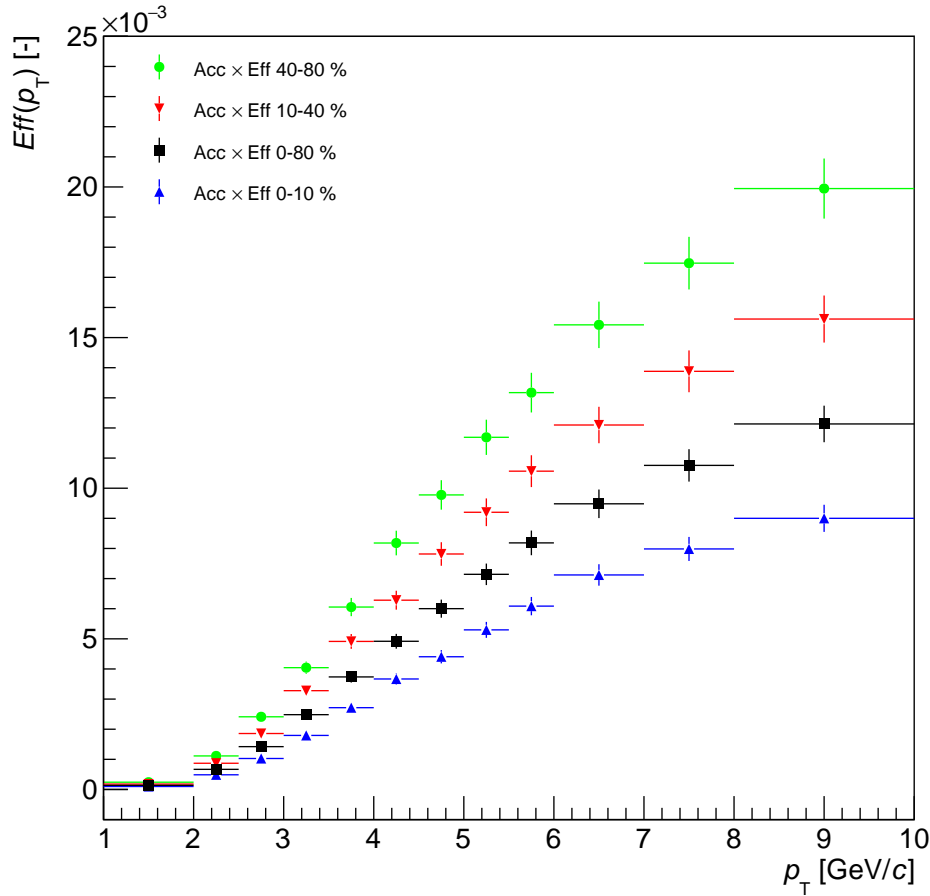


Figure 5.1: The STAR detector acceptance $\times$ efficiency  $Eff(p_T)$  of the  $D^\pm \rightarrow K^\mp + \pi^\pm + \pi^\pm$  reconstruction for centrality bins 0-10 % (blue triangles), 0-80 % (black squares), 10-40 % (red reverse triangles) and 40-80 % (green circles) of Au+Au collisions at  $\sqrt{s_{NN}} = 200$  GeV. Output from the EvtGen-based FastSim. The vertical errorbars are set to match the 5 % systematic error of the FastSim, while the horizontal errorbars show the width of the bins.

## 5.2 Transverse Momentum Correction

The invariant yield data points are scaled by the mean  $p_T$  of each bin. In the calculation given by 5.1, the invariant yield is calculated for each  $p_T$  bin using the  $p_T = \frac{p_{Tmin} + p_{Tmax}}{2}$  approximation, where  $p_{Tmin}$  and  $p_{Tmax}$  are the end points of the bin. Unfortunately, the correct  $p_T$  value is not this trivial mean value, but rather a weighted average dependent on the shape of the  $p_T$  spectrum inside the bin. This effect then mandates that we need to shift the points to the correct position inside the bin and this is especially important for wider bins. An iterative correction method is used to obtain the correct  $p_T$  points.

The invariant yield spectrum is fitted using the Levy function:

$$f(p_T) = \frac{1}{2\pi} \frac{dN}{dy} \cdot \frac{(n-1)(n-2)}{(nT+m)(m(n-1)+nT)} \cdot \left( \frac{nT + \sqrt{p_T^2 + m^2}}{nT+m} \right)^{-n}, \quad (5.2)$$

where  $m = 1.870 \text{ GeV}/c^2$  is the theoretical mass of  $D^\pm$  meson and  $\frac{dN}{dy}$ ,  $T$  and  $n$  are free parameters determined from the fit. From this, we can then calculate the function value of the new point using the formula:

$$f(p_T) = \frac{\int_{p_{T\min}}^{p_{T\max}} f(p_{T0}) dp_{T0}}{\Delta p_T}, \quad (5.3)$$

and then it is possible to finally obtain the new  $p_T$  point. However, this process will naturally change the invariant yield calculated by 5.1, since our initial assumption was not entirely correct, so it is necessary to re-calculate the invariant yield with the new  $p_T$  values. Since the fit would be slightly different this time, this calculation will in turn change the correct position of the  $p_T$  points again, which results in an iterative process. The number of iterations required was three, since the spectrum does not change within the accuracy of  $10^{-5}$  afterwards. The result of the  $p_T$ -point shift correction for the 0-80 % centrality bin can be seen in Fig. 5.2 and for all centrality bins, the results are summarized in Tab. 5.3, where the larger impact on wider bins is apparent.

$p_T$ range [GeV/c]	Original $p_T$ bin center [GeV/c]	Corrected $p_T$ bin center [GeV/c]			
		0-10 %	10-40 %	40-80 %	0-80 %
1.0-2.0	1.50	-	1.38	1.39	1.38
2.0-2.5	2.25	2.21	2.21	2.22	2.21
2.5-3.0	2.75	2.71	2.71	2.72	2.71
3.0-3.5	3.25	3.21	3.21	3.21	3.21
3.5-4.0	3.75	3.71	3.71	3.71	3.71
4.0-4.5	4.25	4.21	4.21	4.22	4.21
4.5-5.0	4.75	4.71	4.72	4.72	4.72
5.0-5.5	5.25	5.22	5.22	5.22	5.22
5.5-6.0	5.75	5.72	5.72	5.72	5.72
6.0-7.0	6.50	6.38	6.38	6.38	6.38
7.0-8.0	7.50	7.39	7.39	7.39	7.39
8.0-10.0	9.00	-	8.36	-	8.62

Table 5.3: Position of original and corrected  $p_T$  points for all 4 centrality bins.

### 5.3 Systematic Errors

The total systematic error  $\sigma_{\text{tot}}$  of the  $D^\pm$  yield measurement can be calculated as

$$\sigma_{\text{tot}} = \sqrt{\sigma_{\text{BR}}^2 + \sigma_{\text{FS}}^2 + \sigma_{\text{sys}}^2}, \quad (5.4)$$

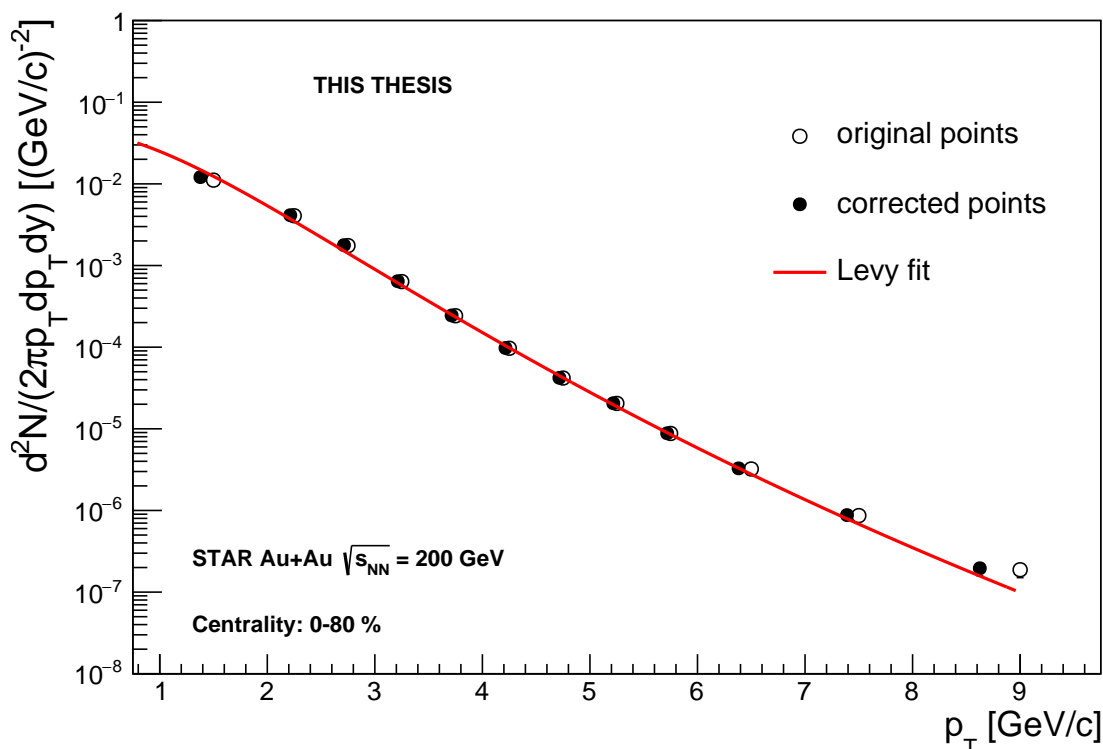


Figure 5.2: The correction for the  $p_T$  point position as a reflection of the spectrum shape inside the bins for the 0-80 % centrality bin. Open circles represent the original position of the points inside the center of each bin and the filled circles represent the correct point position as determined from the Levy fit (red line, see 5.2).

where  $\sigma_{\text{BR}} = 3.1\%$  is the uncertainty of the branching ratio of the decay channel used for this analysis,  $\sigma_{\text{FS}} = 5\%$  is the uncertainty of the FastSim used for the efficiency $\times$ acceptance calculation and  $\sigma_{\text{sys}}$  is the systematic uncertainty of the raw yield. There are many ways of estimating the raw yield systematic error. One estimation has been presented in Ref. [3] and consisted of the variation of several cuts, the binning and fit range one at a time and comparing the raw yields scaled by the respective extraction efficiencies since these ratios should in theory stay the same. We can also estimate the  $\sigma_{\text{sys}}$  by comparing the yields from the  $3\sigma$  bin counting range (where 99.7 % of the  $D^\pm$  mesons should be found) and different range normalized by the value of the error function, which gives the portion of  $D^\pm$  mesons that should be in found in this range (for example, about 95.4 % of all  $D^\pm$  mesons should lie within  $2\sigma$  away from the mean of the Gaussian peak). Another method used to estimate the systematic error is the comparison between the raw yield obtained by bin counting and the raw yield obtained directly from the fit of the signal peak. However, since we will probably use a cut tuning using the Toolkit for Multivariate Analysis (TMVA) package - implemented in Root (see Ch. 6) - as the ultimate method for the raw yield extraction, it makes more sense for the systematic errors to be determined only after the application of such machine-learning techniques and for now remain a work in progress. Another planned task is to investigate the correlations between the systematic uncertainties as

this should reduce the overall measurement uncertainty. Therefore, only the global systematic errors were estimated in this thesis.

## 5.4 $D^\pm$ Spectra

After we applied all the corrections mentioned in this chapter, it was possible to obtain the invariant  $p_T$  spectrum of  $D^\pm$  mesons for 4 centrality bins and compare it with the results from STAR  $D^0$  measurements (after rescaling the  $D^\pm$  data points by a fragmentation function ratio of 0.565/0.246) published in 2018 [58]. The results are shown in Fig. 5.3 - 5.6. The comparison to the  $D^0$  results can be seen in the bottom panel of each corresponding figure. However, since the  $p_T$  binning is different, the results cannot be compared directly to the  $D^0$  data points, but rather are compared to the Levy fit (see Sec: 5.2) of the spectrum. The  $D^\pm$  spectra from the same dataset (2014 Au+Au collisions at  $\sqrt{s_{NN}} = 200$  GeV) obtained by J. Kvapil and presented in his Master's thesis [3] are also shown for comparison. The errorbars of the points from this analysis do not include the full systematic errors as was discussed in Sec. 5.3 and the other results are shown with statistical errors only. For clarification: the results presented in this thesis only are marked as "this thesis", the results marked as "preliminary" are results that have been approved by the STAR collaboration for public presentation and are referenced in the figure captions as are the published results.

The  $D^\pm$  spectrum in the most central bin (0-10 %) exhibits overall behavior similar to the spectrum obtained from the other analyses with the data points mostly consistent within uncertainties, while the first point (2.0-2.5 GeV/ $c$ ) appears to lie below the fit of  $D^0$  points with a  $\sim 1.5 \sigma$  deviation. The invariant mass distribution for this bin does not show any unexpected behavior compared to the other bins (see App. B), however the yield is significantly lower than yield in the same bin in [3]. It is also important to note, that the comparison in the bottom panel of Fig. 5.3 is done to the Levy fit to  $D^0$  points which introduces further uncertainties.

The  $D^\pm$  spectrum for the mid-peripheral centrality range (10-40 %) can be seen in Fig. 5.4 and shows excellent agreement with results from  $D^0$  analysis, while the points from the previous  $D^\pm$  analysis lie above the  $D^0$  points. The only visible exception is again the data point in the first  $p_T$  bin (1-2 GeV/ $c$ ), which appears to lie significantly below the points from the other analyses. As of right now, the reason for this behavior is not known, but the difference seems to be related to the raw yield in the bin, which is significantly higher in [3].

Figure 5.5 shows the results for the 40-80 % centrality bin (peripheral collision). The comparison with the  $D^0$  Levy fit shows good agreement between these two analyses - especially in the middle part ( $2 < p_T < 4$  GeV/ $c$ ) of the  $D^\pm$  spectrum - with the exception again being the first data point (1-2 GeV/ $c$ ), which lies visibly - about  $2 \sigma$  - below the unity line. Again, the corresponding signal peak can be found in App. B and does not exhibit any unconventional behavior. The data points from the previous  $D^\pm$  analysis appear to lie higher than the  $D^0$  spectrum in the mid- $p_T$  range and also do not extend to the 7-8 GeV/ $c$   $p_T$  bin.

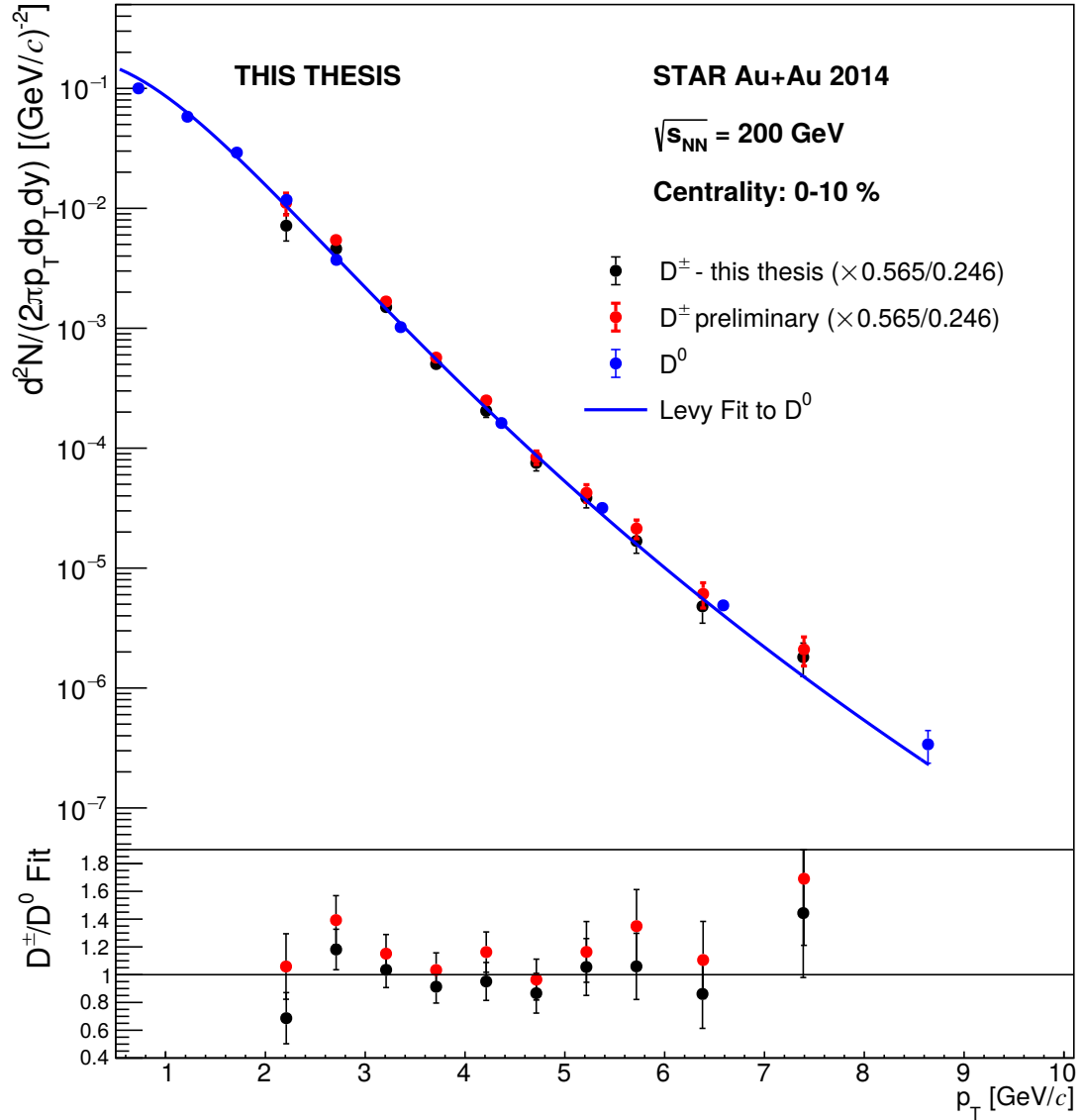


Figure 5.3: Top: The  $D^\pm$   $p_T$  spectrum (invariant yield) obtained in this thesis (black points) and compared with STAR results from  $D^0$  [58] fitted with a Levy function (blue points and line) and  $D^\pm$  results from [3] (red points) in Au+Au collisions at  $\sqrt{s_{NN}} = 200 \text{ GeV}$  for centrality bin 0-10 %. The vertical errorbars represent statistical errors. Bottom: The comparison between the  $D^\pm$  points and the Levy fit to the  $D^0$  points. Please note that all  $D^\pm$  points in both plots are scaled by the fragmentation function ratio 0.565/0.246.

The overall results for all centralities (0-80 %) can be seen in Fig. 5.6. The results again show great agreement with the  $D^0$  analysis, with the majority of the points being consistent with the unity line. The position of the first point is, similarly to other centrality bins, lying below the other results which is expected since the yield in this  $p_T$  bin is dominated by the production in mid-peripheral collisions. The previous  $D^\pm$  analysis data points seem to be above the unity line throughout the  $p_T$  range, with the exception of the first point.

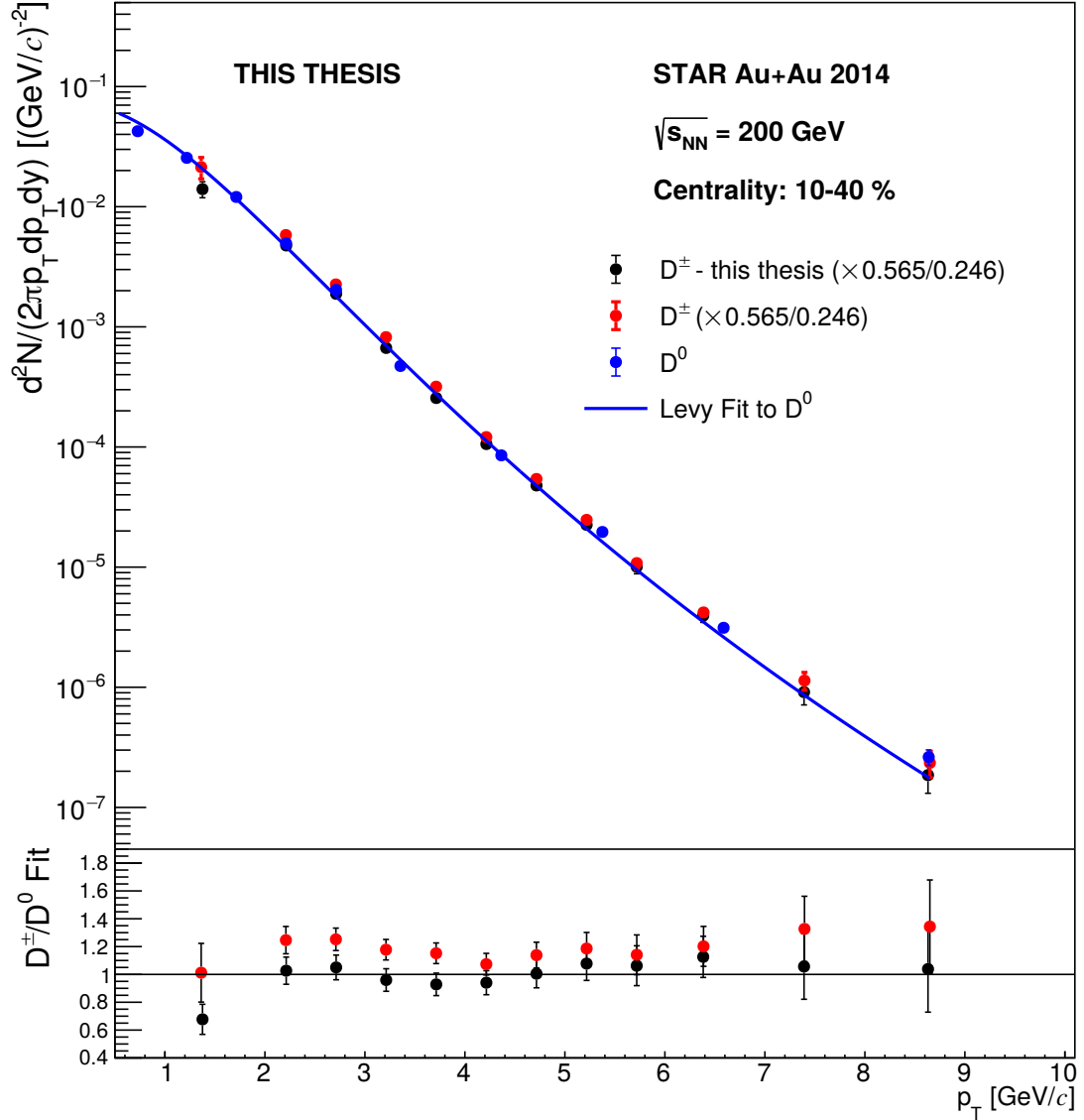


Figure 5.4: Top: The  $D^\pm$   $p_T$  spectrum (invariant yield) obtained in this thesis (black points) and compared with STAR results from  $D^0$  [58] fitted with a Levy function (blue points and line) and  $D^\pm$  results from [3] (red points) in Au+Au collisions at  $\sqrt{s_{NN}} = 200 \text{ GeV}$  for centrality bin 10-40 %. The vertical errorbars represent statistical errors. Bottom: The comparison between the  $D^\pm$  points and the Levy fit to the  $D^0$  points. Please note that all  $D^\pm$  points in both plots are scaled by the fragmentation function ratio 0.565/0.246.

The small differences between the results of the spectra could have various causes. Since the  $D^0$  results come from a different analysis, many extra corrections have to be made to be able to compare the results (fragmentation functions and branching ratios, efficiency difference between 2- and 3-body decays and so on) and the uncertainties of these corrections could add up to the overall dissimilarities. As far as the J. Kvapil results are concerned, some inconsistencies were found in his analysis, which could cause the slight differences observed between the results of these two analyses. J. Kvapil also

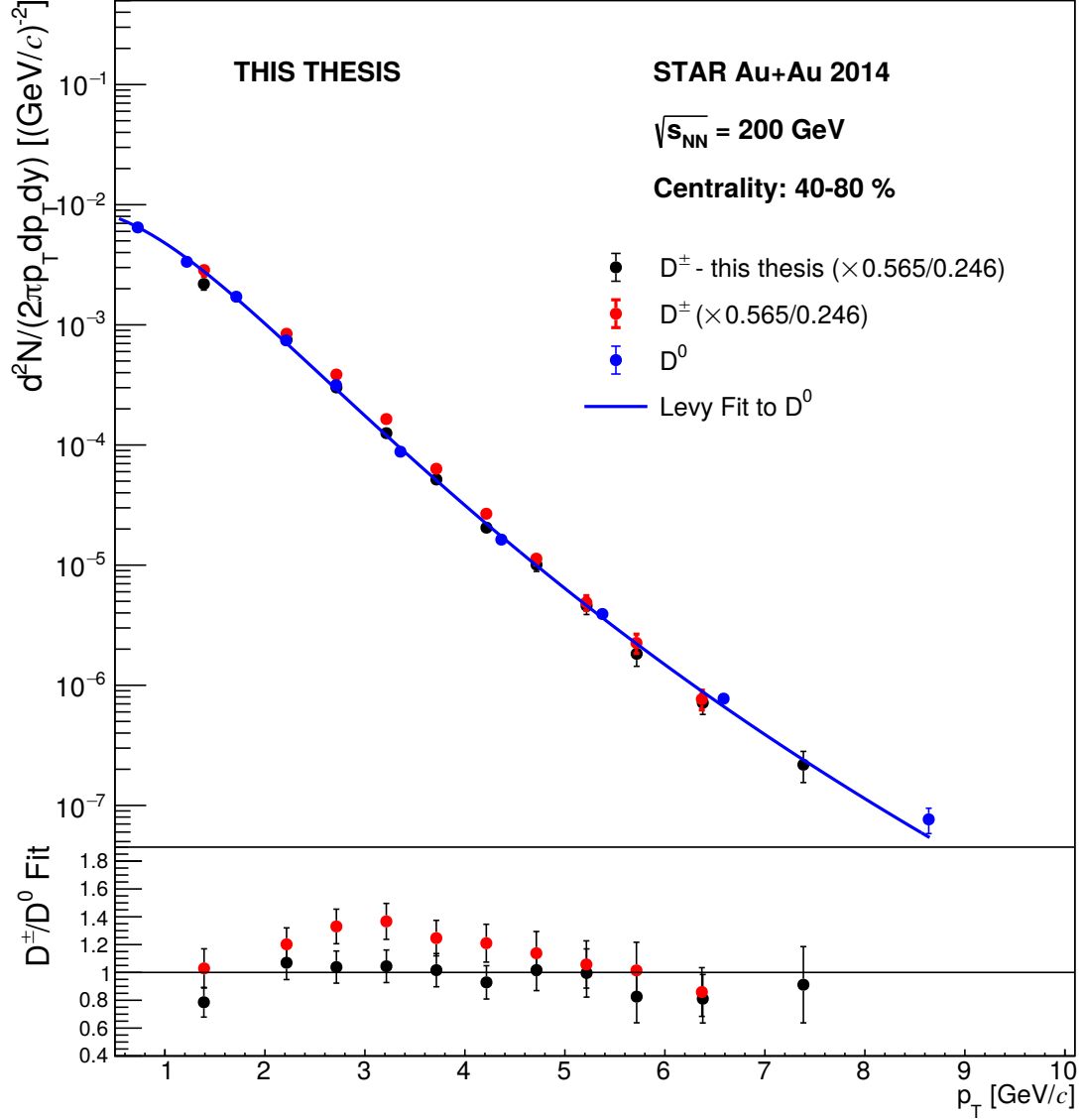


Figure 5.5: Top: The  $D^\pm$   $p_T$  spectrum (invariant yield) obtained in this thesis (black points) and compared with STAR results from  $D^0$  [58] fitted with a Levy function (blue points and line) and  $D^\pm$  results from [3] (red points) in Au+Au collisions at  $\sqrt{s_{NN}} = 200$  GeV for centrality bin 40-80 %. The vertical errorbars represent statistical errors. Bottom: The comparison between the  $D^\pm$  points and the Levy fit to the  $D^0$  points. Please note that all  $D^\pm$  points in both plots are scaled by the fragmentation function ratio 0.565/0.246.

uses an older version of the  $D^\pm \rightarrow K^\mp \pi^\pm \pi^\pm$  branching ratio ( $9.13 \pm 0.19$ ) %, which results in a systematic deviation of about 5 % from the results presented in this thesis, which uses an updated value  $BR = (8.98 \pm 0.28)$  % shown by the PDG group in 2018. However, this should not be an alarming information since the results presented in this work are consistent with the published  $D^0$  results and the significances of signal peaks are similar or even higher than in the previous  $D^\pm$  analysis, which were some of the main goals of this analysis. It is also important to note that the systematic errors

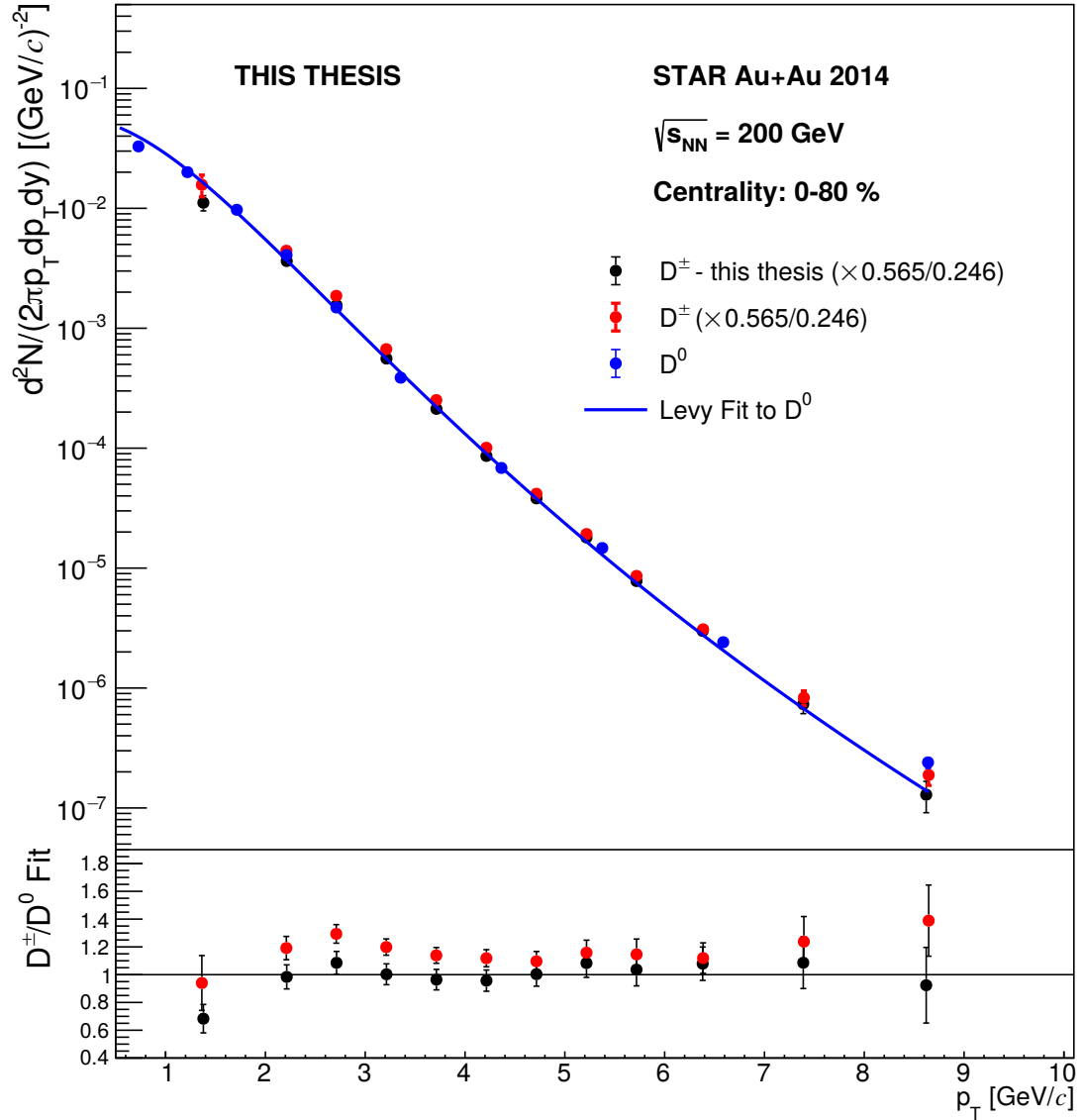


Figure 5.6: Top: The  $D^\pm$   $p_T$  spectrum (invariant yield) obtained in this thesis (black points) and compared with STAR results from  $D^0$  [58] fitted with a Levy function [58] fitted with a Levy function (blue points and line) and  $D^\pm$  results from [3] (red points) in Au+Au collisions at  $\sqrt{s_{NN}} = 200 \text{ GeV}$  for centrality bin 0-80 %. The vertical errorbars represent statistical errors. Bottom: The comparison between the  $D^\pm$  points and the Levy fit to the  $D^0$  points. Please note that all  $D^\pm$  points in both plots are scaled by the fragmentation function ratio 0.565/0.246.

presented in both analyses are not final and will be recalculated in the future. This allows for declaring the results presented in this thesis as consistent with other similar results.

## 5.5 $D^\pm$ Nuclear Modification Factor

The main motivation behind the analysis of  $D^\pm$  meson production in high-energy Au+Au collisions is to investigate the effects of the QGP that is formed in these collisions, but is not expected to form in smaller collision systems. Therefore, the main result of this analysis is the nuclear modification factor  $R_{AA}$ . To obtain the  $R_{AA}$  results presented in this thesis, we divided the spectra presented in Sec. 5.4 by the Levy fit to the published STAR  $D^0$  and  $D^*$  results from p+p collisions taken during the year 2009 [47] that has been then corrected for the  $D^0/D^*$  fragmentation function ratio. These results were then - for the purposes of this analysis - scaled by the STAR collaboration estimation of the average number of binary collisions in each centrality bin (see Tab. 5.4) obtained from MC-Glauber simulations [12].

Centrality [%]	$N_{\text{coll}}$ [-]
0 - 10	$959.65 \pm 36.53$
10 - 40	$401.80 \pm 54.50$
40 - 80	$58.07 \pm 33.02$
0 - 80	$373.00 \pm 73.45$

Table 5.4: The mean number of binary collision in each centrality bin used to scale the p+p data in this analysis estimated by the MC-Glauber simulation.

The p+p reference introduces a global systematic uncertainty of 10.4 % into the  $D^\pm$  results. The other global systematic uncertainty shown along with the  $R_{AA}$  dependence on  $p_T$  in Figs. 5.7 - 5.9 is a combined systematic error from the branching ratio error, the fragmentation function error and the uncertainty of the estimation of the number of binary collisions in the analysis bins. The data points are again compared to the results from the 2014 STAR  $D^0$  measurements [58] and also to the (corrected)  $D^0$  results from the pre-HFT analysis of data from years 2010 and 2011 [103] in same centrality bins, collision system and energy. Since the study of systematic errors is not complete yet, only statistical uncertainties are shown as errorbars with the points.

The  $R_{AA}$  dependence on  $p_T$  for the 0-10 % most central Au+Au collisions is shown in Fig. 5.7. The results appear to have the expected shape, consistent with the results from the  $D^0$  analyses with a hint of a maximum at low  $p_T$  and then declining with higher  $p_T$  and reaching values as low as  $R_{AA} \simeq 0.2$ . These results show significant suppression of the D meson production that could be interpreted as a result of the charm quark energy loss in the medium created in central Au+Au collisions at high energy.

Similar situation can be seen in Fig. 5.8 for the 10-40 % centrality bin. The nuclear modification factor in this centrality bin also exhibits trend consistent with the results from  $D^0$  measurements. There is again a maximum in the low- $p_T$  region (2-3 GeV/c) and then a decreasing trend towards the higher  $p_T$  region. The lowest value of  $R_{AA}$  in the mid-peripheral collisions is about twice as high as in the most central collisions (Fig. 5.7) indicating lower suppression in these types of collision, which is not surprising since we expect the energy density of these collisions to be lower due to the lower number of participants and binary collisions.

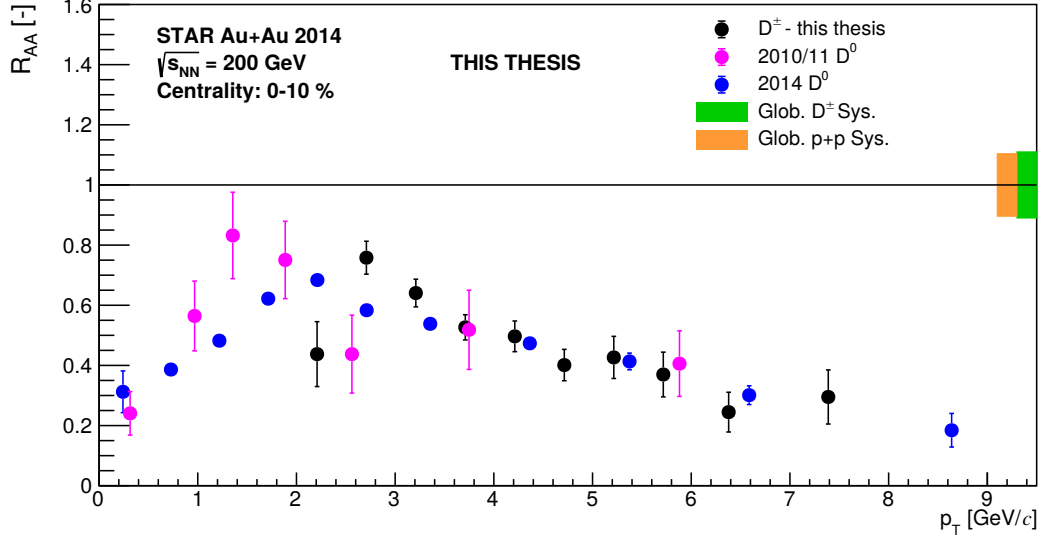


Figure 5.7: The  $D^\pm$  nuclear modification factor  $R_{AA}$  as a function of  $p_T$  for the 0-10 % most central Au+Au collisions at  $\sqrt{s_{NN}} = 200$  GeV. The black points represent the  $D^\pm$   $R_{AA}$  obtained in this analysis while the blue and magenta points represent STAR results from  $D^0$  from years 2014 [58] and 2010/11 [103] respectively. The vertical errorbars represent statistical errors. The global systematic uncertainties are also shown as the color bands on the side of the figure.

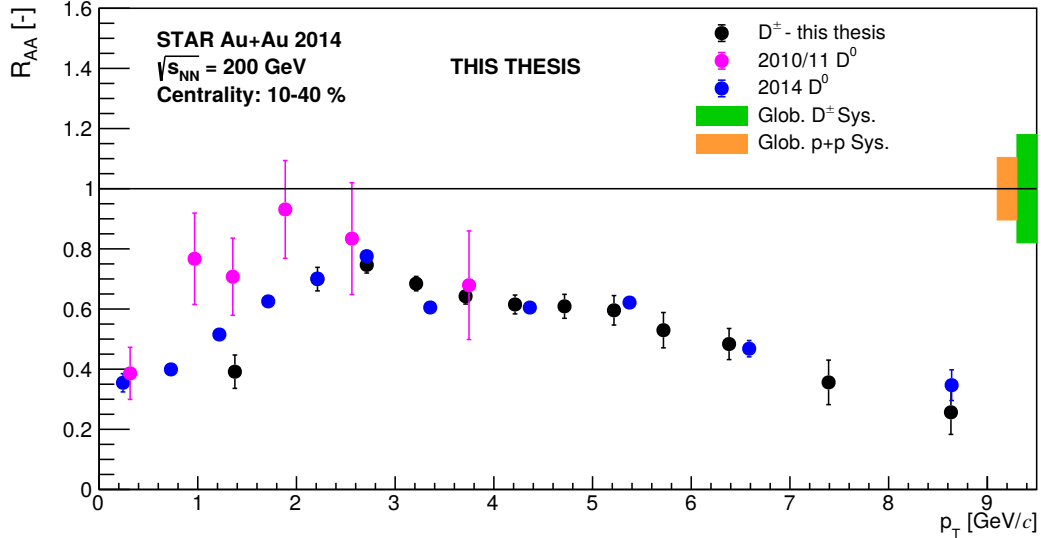


Figure 5.8: The  $D^\pm$  nuclear modification factor  $R_{AA}$  as a function of  $p_T$  for the 10-40 % centrality bin in Au+Au collisions at  $\sqrt{s_{NN}} = 200$  GeV. The black points represent the  $D^\pm$   $R_{AA}$  obtained in this analysis while the blue and magenta points represent STAR results from  $D^0$  from years 2014 [58] and 2010/11 [103] respectively. The vertical errorbars represent statistical errors. The global systematic uncertainties are also shown as the color bands on the side of the figure.

Figure 5.9 shows the  $D^\pm$  nuclear modification factor as a function of  $p_T$  obtained in the most peripheral collisions measurable at STAR (40-80 % centrality). A hint of a

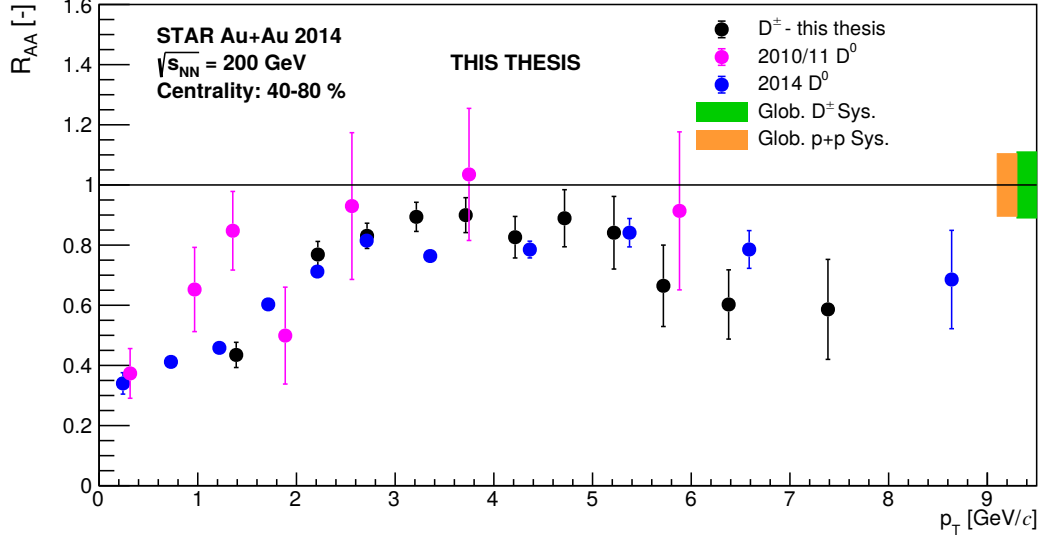


Figure 5.9: The  $D^\pm$  nuclear modification factor  $R_{AA}$  as a function of  $p_T$  for the 40-80 % centrality bin in Au+Au collisions at  $\sqrt{s_{NN}} = 200$  GeV. The black points represent the  $D^\pm$   $R_{AA}$  obtained in this analysis while the blue and magenta points represent STAR results from  $D^0$  from years 2014 [58] and 2010/11 [103] respectively. The vertical errorbars represent statistical errors. The global systematic uncertainties are also shown as the color bands on the side of the figure.

maximum is again observed at  $p_T \simeq 3 - 5$  GeV/ $c$  and the points lie slightly below the unity line, which indicates slight  $D^\pm$  meson production suppression in this centrality bin. The  $D^\pm$  data points are consistent within uncertainties with both results from  $D^0$  analysis, especially considering that we do not show the systematical error in the plots.

Overall, these  $D^\pm$   $R_{AA}$  results follow the same trend as the  $D^0$  results from other STAR analyses and indicate charmed-meson production suppression - increasing with centrality - in Au+Au collisions at  $\sqrt{s_{NN}} = 200$  GeV, and therefore support the claim, that charm quarks lose significant amounts of energy in the QGP.

# Chapter 6

## Application of Machine-Learning Techniques

The ability of artificial intelligence to improve over time, based on self-analyzing and self-implementing its previous results has been an active and fascinating topic since the beginning of the computer era. Since computers today can perform calculations at much higher rates than humans, it would seem beneficial to eliminate the need to explicitly program every task we require from the computer and rather develop an algorithm that can improve itself by learning from available data the same way as humans do, but much faster. Machine learning today has a very broad range of applications including the field of high-energy physics (Sec. 6.1), where various techniques are used to improve the experimental results. The application of the Boosted Decision Tree method on STAR data from Au+Au collisions at  $\sqrt{s_{\text{NN}}} = 200$  GeV, with an aim to improve the significance of the  $D^\pm$  signal, is discussed in Sec. 6.2.

### 6.1 Machine Learning in High-Energy Physics

Physicists in the field of high-energy physics have long been interested in machine learning as a tool to improve the precision of their results. This is especially true for analyses, where it is difficult to distinguish between the main two classes of data - signal and background - because, for example, the studied process is very rare and is therefore overshadowed by the background. The most common way to distinguish between signal and background is to apply cuts on certain variables which are chosen based on the knowledge of the physical processes and therefore should have a discriminating power, as was illustrated in Ch. 4. One of the main objectives is then to maximize the discriminating power of the cuts. We can achieve that by selecting variables whose distributions show large differences for the signal and for the background and then cutting on them at a point that rejects most of the background while keeping as much signal as possible. In general, the optimization problem can be stated as follows: we have a  $d$ -dimensional space, where  $d$  is the number of our variables and we want to find a function  $f$  which transforms a  $d$ -dimensional vector of input variables into an  $n$ -dimensional output vector, preferably so that  $n \ll d$  and therefore simplifies

the problem. Such function  $f$  is then called the response function. In high-energy physics, we want to discriminate between signal and background, therefore, we set  $n = 1$  and then the output vector is a number between -1 (pure background) and +1 (pure signal). When both the input and the output are known, we are talking about supervised machine learning (as is our case), while unsupervised machine learning gives us an output which is not known and the main result are the connections between the input variables.

There are many methods of optimization using machine learning and some of the most common ones were implemented into the ROOT framework as a part of the Toolkit for Multivariate Analysis (TMVA) package [104]. The most basic TMVA technique is the rectangular cuts optimization. This method varies the values of selected variables and looks for the highest significance (or signal-to-background ratio) in the reconstructed signal. This process then results in a single hypercube in the  $d$ -dimensional variable space, which has the highest concentration of signal. Another machine-learning technique, which is more advanced and also widely popular within the high-energy physics community, is the usage of Boosted Decision Trees (BDT). A cartoon illustration of a binary decision tree can be seen in Fig. 6.1.

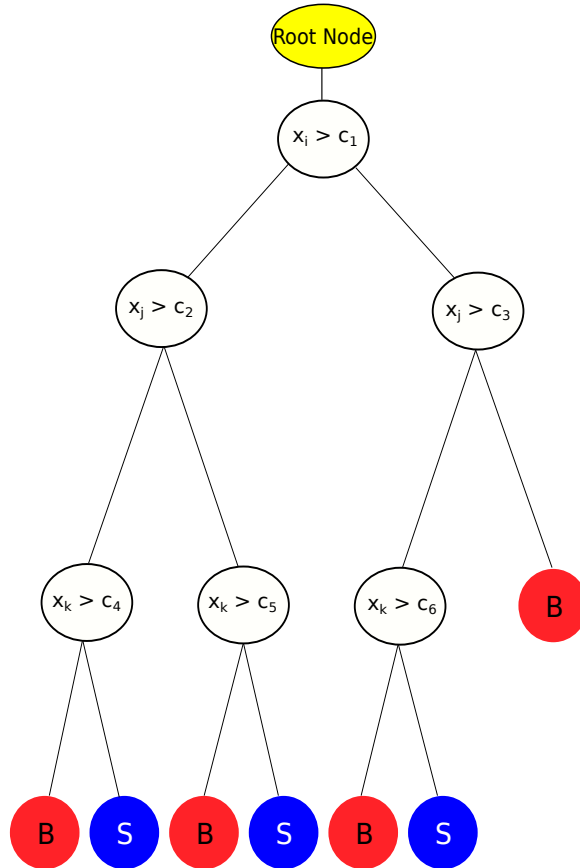


Figure 6.1: An illustration of a decision tree, where  $x_{i,j,k}$  represent different variables and  $c_n$  represent corresponding cut values. S and B then represent signal-like and background-like event respectively.

A binary decision tree contains both signal and background samples in the root node. One variable is compared to a conditional value (cut) and the dataset is subsequently divided into two disjoint sets based on the result of the comparison. In the following steps, other divisions are occurring either with the same variable and different cut value or with one of the other discriminating variables. In the end, the leaf nodes get labeled as signal (S) or background (B) based on the majority of data that ended up in this node during the BDT training part. In simple terms, the training is basically showing the TMVA what our signal and background looks like and will be illustrated on an example in Sec. 6.2. The decision tree method is similar to the optimized rectangular cuts method since both cut the space into signal-like and background-like hypercubes with the main difference (and advantage) being that the decision tree is not limited to a single hypercube, but can select multiple hypercubes for one dataset. Therefore - in theory - the BDT method should give us a better classification performance, since it should converge in the worst case to the result from rectangular cuts optimization. However, using just one large decision tree would be inefficient, since large trees are prone to overtraining (fixating on fluctuations). Therefore, a forest of smaller trees is used instead (boosting). The boosting process then dramatically reduces the instability due to overtraining while maintaining a high separation power. These are the reasons why we chose to use the TMVA:BDT method to improve the significance of the  $D^\pm$  signal.

## 6.2 Reconstruction of $D^\pm$ Meson Using TMVA

As described in the previous section, physicists often use machine-learning techniques to improve the classification of the data as signal or background. We have chosen the TMVA:BDT method to try to improve the significance of the  $D^\pm$  signal (see Ch. 4). The application of the BDT is done in two steps - training and application on real data - which will be described in the following subsections.

### 6.2.1 BDT Training

The training of the BDT is an important part of the whole reconstruction process, since we need an algorithm that can discriminate correctly between the signal and the background. The first phase of the BDT training is to choose correct variables with high discriminating power. Influenced by the approach in the analysis with rectangular cuts, the chosen variables were:

- distance of closest approach of daughters to PV  $DCA_{\pi 1}$ ,  $DCA_{\pi 2}$  and  $DCA_K$
- distance of closest approach of daughter pairs  $DCA_{\text{pair}}$
- pointing angle  $\cos \theta$
- $D^\pm$  meson decay length  $\lambda$ .

The maximum vertex triangle side length ( $\Delta_{\max}$ ) was not used for the training since it is highly correlated with  $\lambda$  ( $\sim 90\%$ ).

The next step was producing the signal and background samples. For the signal sample, we used 8.37 M  $D^\pm$  mesons generated by the FastSim (see Sec. 5.1), which used PYTHIA to decay them into the daughter triplets via the decay channel  $D^\pm \rightarrow K^\mp \pi^\pm \pi^\pm$  and smeared the distributions of the variables so they are consistent with the real data from STAR 2014 Au+Au collisions at  $\sqrt{s_{\text{NN}}} = 200$  GeV. The background sample has been selected directly from these STAR data, using only wrong-sign combinations to avoid introducing a bias. Loose rectangular cuts were used to select 8.41 M background triplets. The training was done in the same bins as the analysis. The distributions of all six discriminating variables used for the BDT training for signal and background with  $2.0 < p_T < 2.5$  GeV/ $c$  and centrality range 0-10 % can be seen in Fig. 6.2. It appears that the pointing angle is the variable with the highest discriminating power, which is expected, since the signal triplets are generated with  $\cos\theta = 1$  and then smeared by the  $p$  resolution of the detector (this closely resembles the reality), while the background distribution in  $\cos\theta$  is not expected to show any distinct features. The daughter DCA variables  $DCA_K$  and  $DCA_\pi$  also show good discriminating power as does the decay length  $\lambda$ . On the other hand, the  $DCA_{\text{pair}}$  distribution does not show much difference between the signal and background. The correlations between the training variables for signal and background can be seen in Fig. 6.3, with most variables showing mild (anti)correlations ( $< 15\%$ ) for both signal and background, while the  $DCA_{\text{pair}}$  and  $\lambda$  variables are more correlated. Overall, the signal shows larger (anti)correlations than the background which is expected.

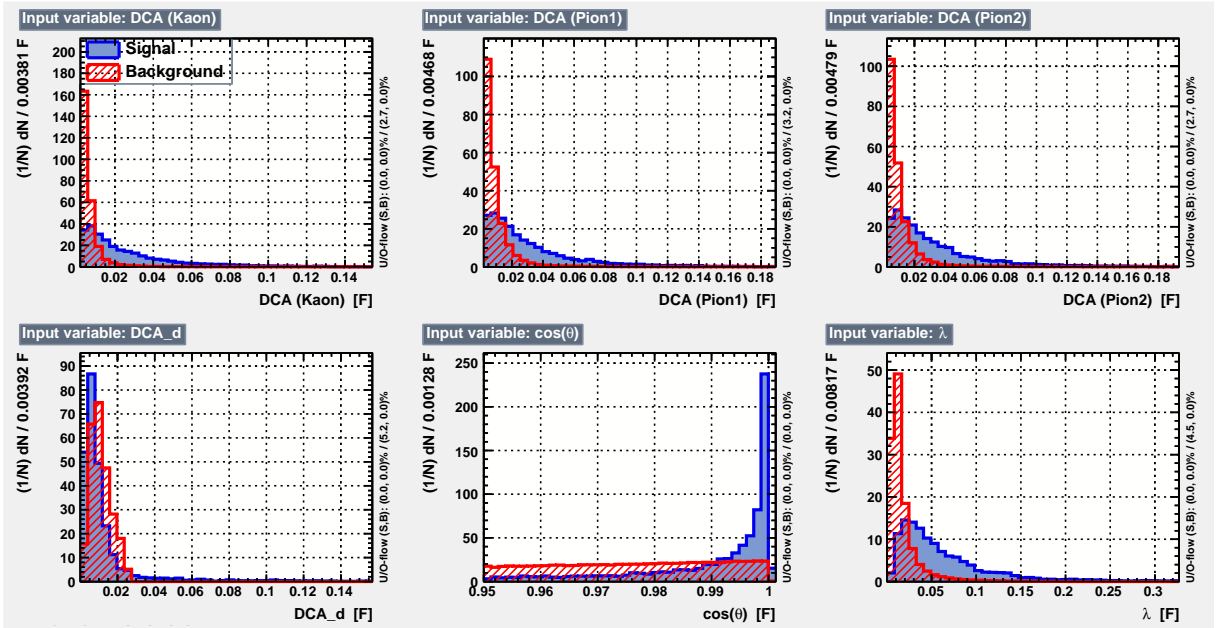


Figure 6.2: The distributions of all 6 discriminating variables in background (red) and signal (blue) samples used for BDT training in the  $2.0 < p_T < 2.5$  GeV/ $c$  and 0-10 % centrality bin.

The maximum depth of the trees - the number of steps between the root node

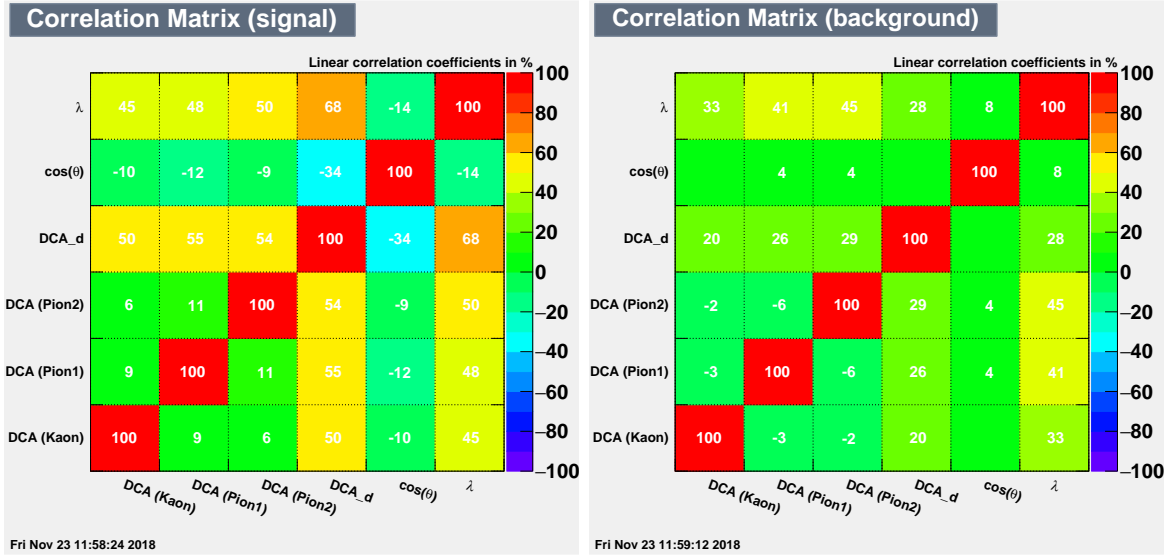


Figure 6.3: The correlation matrix of discriminating variables for signal (left) and background (right) training samples in the  $2.0 < p_T < 2.5$  GeV/c and 0-10 % centrality bin.

and the leaf nodes - is set to three (as illustrated in Fig. 6.1), while the number of trees is 850 (both standard settings, which were optimized by the developers). These weak trees are then boosted using the AdaBoost algorithm, which assigns a weight to each tree based on its performance. Because of the boosting, the decision trees are not prone to overtraining. The overtraining can be defined as an over-fixation on statistical fluctuations caused by having too many options for a limited sample of training events. For this reason, the input datasets for signal and background are split into two samples - training and testing. The training sample is used for the BDT training as described in this section, while the test sample is used to compare the performance of the trees. In ideal case, distributions of signal and background for both test and training samples should be identical. The situation for the  $2.0 < p_T < 2.5$  GeV/c and 0-10 % centrality bin can be seen in Fig. 6.4 and shows good agreement between both samples (the Kolmogorov-Smirnov test implemented within TMVA is known to perform incorrectly so we use just visual comparison) and therefore the BDT can be considered well-trained in this bin.

## 6.2.2 BDT Application and Results

After successfully training the decision trees, we could apply them on real data and then the  $D^\pm$  signal could be extracted. The application consists of applying a single cut on the BDT response function instead of many rectangular cuts as described in Ch. 4 and afterwards, the process of raw yield extraction is identical. However, the selection of the optimal BDT response function value is not trivial, since we want to avoid introducing any bias into the analysis. First, we need to define what our optimal cut should be. For our purposes, we consider the optimal BDT response value the one that gives us the highest signal significance. However, the dependence of the

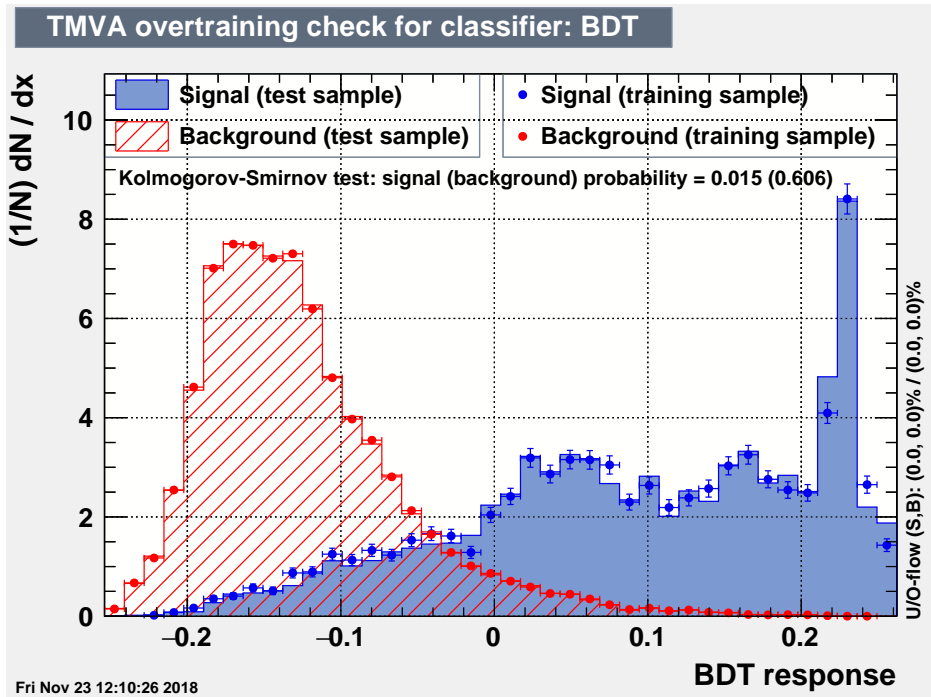


Figure 6.4: The distributions of signal (blue) and background (red) as a function of the BDT response function value with training samples plotted over the test sample results.

signal significance on the value of the BDT response function also depends on the ratio between the number of signal and background events in the real dataset. Therefore, we need to estimate the expected number of  $D^\pm$  mesons before we can apply the BDT cut and extract the yield. The situation can be seen in Fig. 6.5, where the green curve represents the significance dependence on the BDT cut value for 4 different cases of signal-to-background (S:B) ratio (1:1, 1:100, 1:1000, 1:10000). There is a clear change of behavior, where the significance maximum shifts towards higher BDT cut values as the S:B ratio decreases, while the curve exhibits less smooth behavior.

There are some ways to estimate the correct S:B ratio, for example, one can deduce the ratio from a previous  $D^0$  analysis. However, this would then make our results reliant on the results of another analysis which naturally introduces a bias into our analysis. However, there is another way of obtaining the optimal value of the BDT response cut. This method does not predict the correct way of the BDT cut before the application but rather applies many values of the BDT cut simultaneously on the  $K\pi\pi$  triplets ( $D^\pm$  candidates) created with loose pre-cuts, and for each value we extract the raw yield and significance. This process produces a significance dependence on the BDT cut value, similarly to the ones seen in Fig. 6.5, only this time represented by a set of points instead of a curve (see Fig. 6.6). We can then select the value which gives us the highest significance of the signal. However, we need to be careful not to select a value that is a result of some fluctuation without any physical meaning. The two main indications, that this method is correct is the rather smooth shape of the significance vs. BDT response dependence (finer binning was used around the maximum) and the

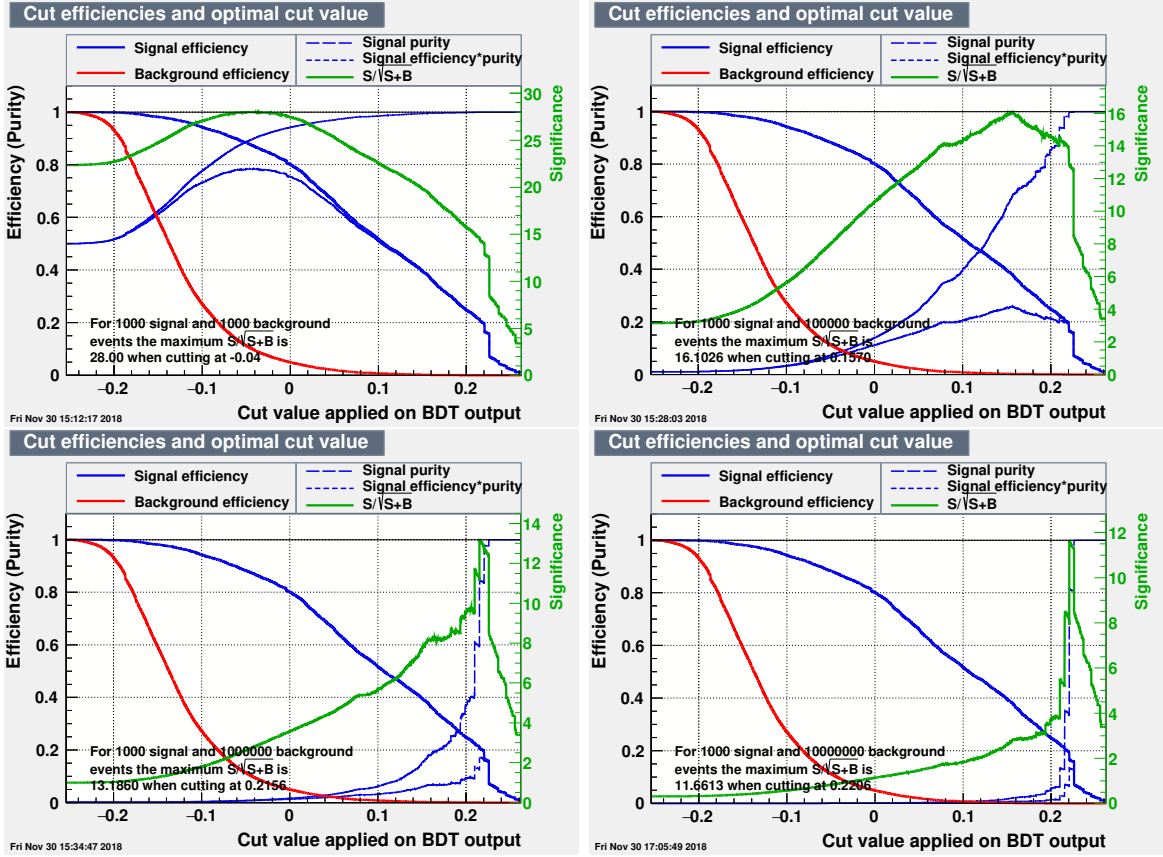


Figure 6.5: The signal significance as a function of the BDT response function (green curve) for the  $2.0 < p_T < 2.5$  GeV/ $c$  range in the 0-10 % most central Au+Au collisions at  $\sqrt{s_{NN}} = 200$  GeV for four different cases of signal-to-background ratio: 1:1 (top, left), 1:100 (top, right), 1:1000 (bottom, left) and 1:10000 (bottom, right). Please note, that the ratios are multiplied by a factor of 1000 to represent a more realistic estimate of the raw yield and significance inside this bin, while showing the same curve.

non-existence of a peak-like structure in the wrong-sign triplet distributions in the  $D^\pm$  mass region, while the peak is clearly visible in the correct-sign distribution, as shown in Fig. 6.7 for the  $2.0 < p_T < 2.5$  GeV/ $c$  range in the 0-10 % most central collisions.

After obtaining the invariant mass spectrum, using the same raw yield extraction technique as before, we could compare the results of both methods. The difference between both distributions in the  $2.0 < p_T < 2.5$  GeV/ $c$  and 0-10 % centrality bin is clearly visible in Fig. 6.8, as the significance of the peak on the right hand side (with BDT optimization) is almost 5 times higher than without optimized cuts.

So far, the BDT cuts were successfully applied on 7  $p_T$  bins in the 0-10 % centrality range. The comparison between the raw yields and  $D^\pm$  signal significances can be seen in Fig. 6.9 and is also summarized in Tab. 6.1. The improvement at the higher  $p_T$  is also significant, even though it does not reach the improvement for the 2.0-2.5 GeV/ $c$   $p_T$  bin. This is expected, because most of the rectangular topological cuts were chosen to keep sufficient statistic even in the higher  $p_T$  region and therefore do not perform very well in the low- $p_T$  region. The samples used for the BDT training are not large enough

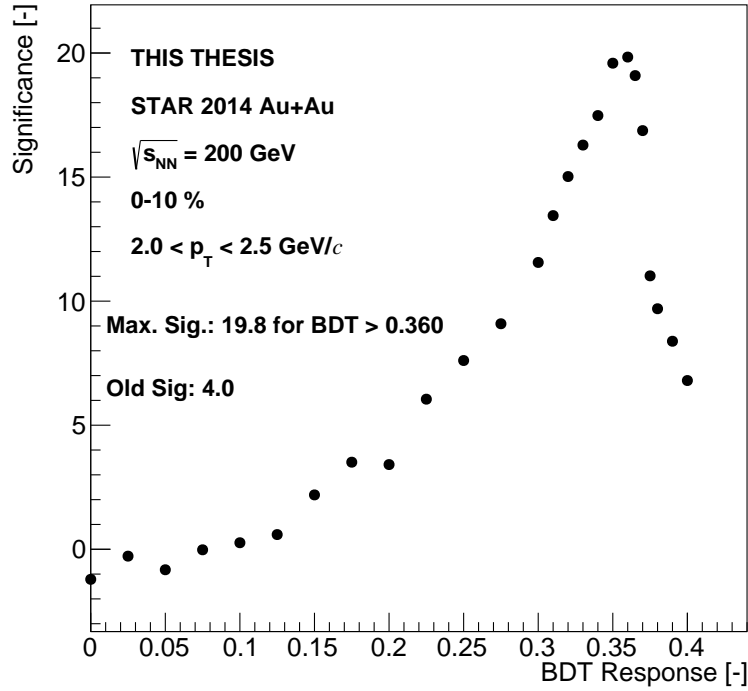


Figure 6.6: The black points represent the  $D^\pm$  signal significance for a given value of the BDT response cut for the  $2.0 < p_T < 2.5$  GeV/ $c$  range in the 0-10 % most central Au+Au collisions at  $\sqrt{s_{NN}} = 200$  GeV. The maximal significance is shown along with the corresponding BDT cut value, as well as the significance of the  $D^\pm$  signal obtained using the unoptimized rectangular cuts in the same  $p_T$  and centrality bin.

to sufficiently train the trees in the high  $p_T$  region ( $p_T > 5.5$  GeV/ $c$ ), and therefore the performance in those bins is very poor and not presented in this thesis. However, since the main motivation for the use of the BDT method is to obtain significant  $D^\pm$  signal in the low- $p_T$  region - where the uncertainties are not dominated by the low statistics, but by the presence of a large combinatorial background - even these early results show great promise for the BDT analysis in this region. If possible, we would like to extract the  $D^\pm$  signal in bins as low as  $0 < p_T < 0.5$  GeV/ $c$  to be able to further confirm the results from  $D^0$  analyses (see Ch. 5) and deepen our understanding of the charm quark interaction inside the QGP.

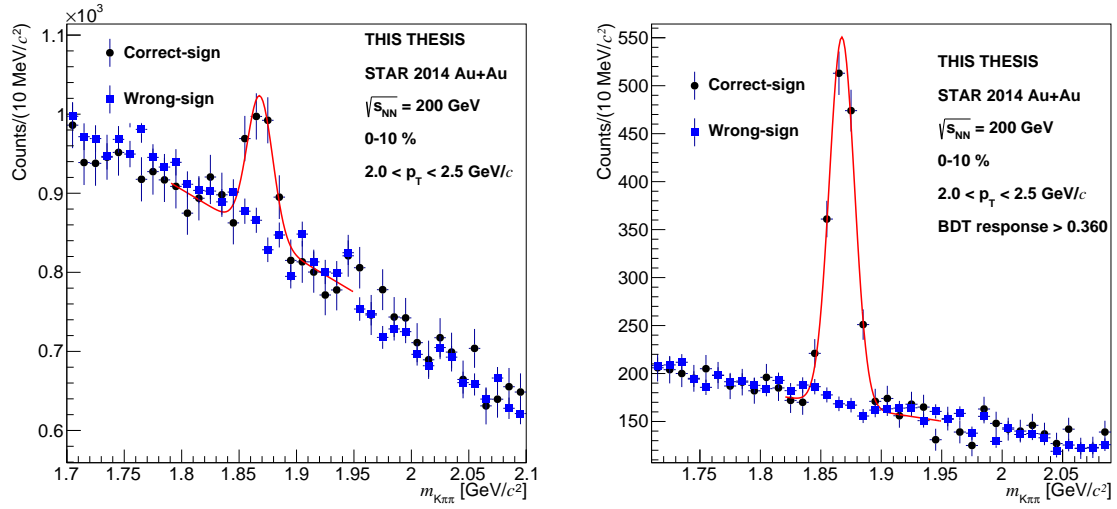


Figure 6.7: The invariant mass distributions of correct-sign (black circles) and wrong-sign (blue squares)  $K\pi\pi$  triplets around the expected  $D^\pm$  mass range for the  $2.0 < p_T < 2.5$   $\text{GeV}/c$  range in the 0-10 % most central Au+Au collisions at  $\sqrt{s_{\text{NN}}} = 200$  GeV. The correct-sign distribution has been fitted by a Gaussian+linear function (red line). The plot on the left hand side was made with using unoptimized rectangular cuts, while the plot on the right was made with the BDT response cut  $> 0.360$ .

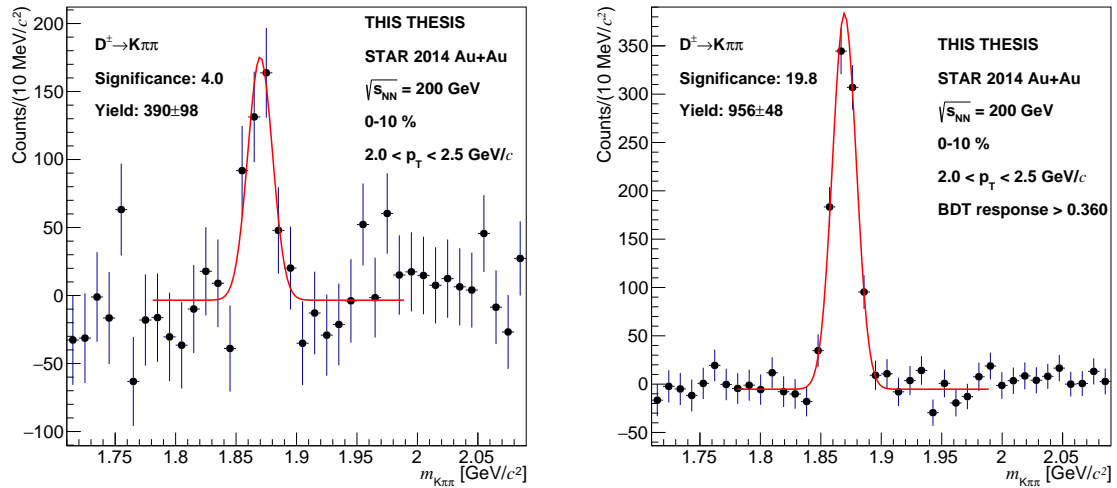


Figure 6.8: The  $K\pi\pi$  triplet invariant mass distributions after background subtraction for the  $2.0 < p_T < 2.5$   $\text{GeV}/c$  range in the 0-10 % most central Au+Au collisions at  $\sqrt{s_{\text{NN}}} = 200$  GeV obtained by the unoptimized rectangular cuts method (left) and by the TMVA:BDT method (right). Please note different scale of the  $y$  axis. The raw yield and the  $D^\pm$  signal significance is shown in both cases as well.

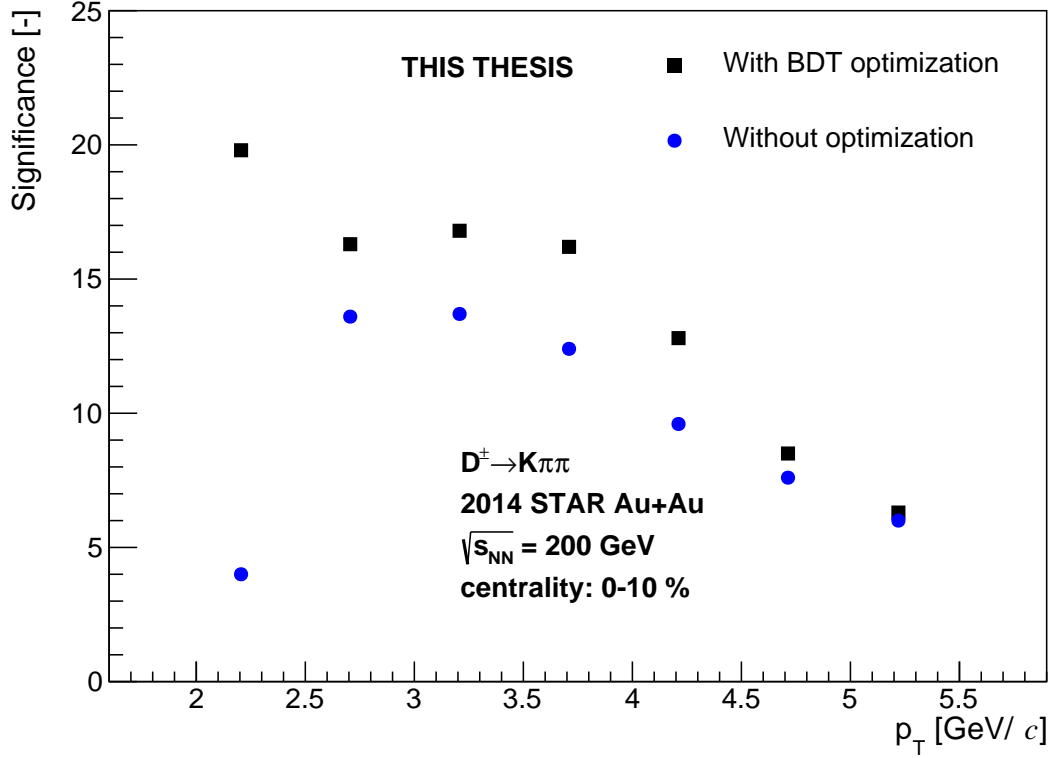


Figure 6.9: Significance of  $D^\pm$  signal in the  $2.0 < p_T < 5.5$  GeV/ $c$  range for the 0-10 % most central Au+Au collisions at  $\sqrt{s_{NN}} = 200$  GeV. The black squares represent values obtained using the BDT optimization, while the blue circles represent values obtained by using unoptimized rectangular cuts. See also Tab. 6.1.

$p_T$ range [GeV/ $c$ ]	Rectangular cuts		BDT optimization	
	Yield [-]	Sig. [-]	Yield [-]	Sig. [-]
2.0-2.5	$390 \pm 98$	4.0	$956 \pm 48$	19.8
2.5-3.0	$647 \pm 47$	13.6	$1013 \pm 62$	16.3
3.0-3.5	$437 \pm 32$	13.7	$534 \pm 32$	16.8
3.5-4.0	$256 \pm 21$	12.4	$461 \pm 28$	16.3
4.0-4.5	$160 \pm 17$	9.6	$207 \pm 16$	12.8
4.5-5.0	$79 \pm 10$	7.6	$113 \pm 13$	8.5
5.0-5.5	$54 \pm 9$	6.0	$85 \pm 14$	6.3

Table 6.1: Raw yield and significance of the  $D^\pm$  in the 0-10 % most central Au+Au collisions at  $\sqrt{s_{NN}} = 200$  GeV in all  $p_T$  bins with good performance. Compared are the results from the unoptimized rectangular cuts analysis and the results obtained using BDT optimization. See also Fig. 6.9.

# Summary

The main motivation and purpose of this thesis was to study the production of open-charmed meson  $D^\pm$  in ultrarelativistic heavy-ion collisions. The first chapter of this work provides an introduction to the physics of high-energy heavy-ion collisions. First, the basic variables used for the description of the collisions were introduced, then, the collision space-time evolution was discussed and afterwards, the chapter focused on the exotic state of matter created in these high energy collisions - the Quark-Gluon Plasma, including the physical background for the parton energy loss and system collectivity. The importance of the probes in the QGP - including the charmed mesons - has also been discussed.

The second chapter presented an overview of recent results from open-charmed meson measurements by major collaborations at RHIC (STAR) and the LHC (ALICE, ATLAS and CMS). The D meson production in p+p collision can be sufficiently described by pQCD calculations. These recent measurements have shown that the D meson production is not suppressed in p+A collisions at LHC energies. However, significant D meson collectivity has been observed in these collisions - which serve as a baseline for the cold nuclear matter effects - at both RHIC and the LHC. The measurements of D meson production at RHIC and the LHC have shown significant suppression in central heavy-ion collisions compared to proton-proton collisions. The suppression at high  $p_T$  is comparable to the suppression observed for lighter hadrons - an evidence of large energy loss of charm quarks inside the QGP. The measurements have also shown significant collective motion of D mesons, which means, that charm quarks enter a thermal equilibrium within the medium during the hydrodynamical evolution of the system.

The third chapter presented RHIC - the only particle accelerator in the world designed specifically for collisions of many different systems and also capable of colliding polarized protons - and mainly the STAR experiment and its subdetectors. STAR has great tracking and particle identification abilities and allows very precise measurements thanks to the unprecedented pointing resolution of the Heavy Flavor Tracker - a multi-layer silicon detector designed specifically for the reconstruction of open-heavy-flavor hadrons.

In the following chapters, we presented the practical results of this work. The fourth chapter provided a detailed description of the  $D^\pm$  raw yield extraction from a dataset consisting of Au+Au collisions at  $\sqrt{s_{NN}} = 200$  GeV taken by the STAR experiment during year 2014. Significant  $D^\pm$  signal has been reconstructed in 10-12  $p_T$  bins from 1 to 10 GeV/c in each of the 3 centrality bins (0-10 %, 10-40 % and 40-80 %) and also

in the inclusive 0-80 % centrality bin.

The next chapter described the corrections applied to the raw yield - including the STAR detector acceptance and reconstruction efficiency calculation and the  $p_T$  point correction - and presented the  $D^\pm$  meson invariant  $p_T$  spectra. The  $p_T$  spectra show great agreement with STAR  $D^0$  measurement and improve the previous results of  $D^\pm$  analysis. The spectra were then compared to the spectra of  $D$  mesons in p+p collisions at the same energy, producing the nuclear modification factor. These results have shown strong suppression ( $R_{AA} \leq 0.5$  for particles with  $p_T > 4.5$  GeV/ $c$ ) of the  $D^\pm$  meson production in central Au+Au collisions with the suppression observable even in more peripheral collisions. The observed behavior is consistent with the measurements from the  $D^0$  analyses, confirming large energy losses of the charm quark inside the medium created in high-energy Au+Au collisions. The results also improve the results of the previous STAR  $D^\pm$  analysis, which was also one of the main goals of this thesis. The systematic errors were also briefly discussed in this chapter.

Finally, the last chapter contains a brief introduction to the application of machine-learning techniques - a modern trend in the field of high energy physics - and a demonstration of the performance of the Boosted Decision Trees method, which is implemented in the ROOT TMVA package, on the  $D^\pm$  reconstruction in the 0-10 % most central Au+Au collisions at  $\sqrt{s_{NN}} = 200$  GeV detected by the STAR experiment in 2014. The improvement of the signal significance has been remarkable, especially at the low- $p_T$  region (from 4.0 to 19.8 for particles with  $2.0 < p_T < 2.5$  GeV/ $c$ ), which demonstrated that the BDT method can distinguish between the signal and background much better than the manually-tuned rectangular cuts. The application of the BDT method has shown great potential towards future analysis, which should extend the  $D^\pm$  measurement to the lowest part of the  $p_T$  spectrum (ideally down to  $p_T \sim 0$ ) for all centrality bins. The plan is then to precisely determine the systematic errors of this measurement and publish the results together with STAR results of  $D^\pm$  production in similar dataset from the year 2016.

# References

- [1] C. Patrignani *et al.* (Particle Data Group), *Chin. Phys. C*, 40, 100001 (2016) and 2017 update.
- [2] J. Kvapil (STAR Collaboration), "D<sup>±</sup> meson production in Au+Au collisions at  $\sqrt{s_{NN}} = 200$  GeV measured by the STAR experiment", Quark Matter 2017, Chicago, 2/5-11/2017.
- [3] J. Kvapil, "Charged charm mesons in Au+Au collisions", Master's Thesis, Czech Technical University in Prague, 2017.
- [4] B. B. Back, "Studies of multiplicity in relativistic heavy-ion collisions ", 11/8/2004, *J. Phys.: Conf. Ser.* 5 (2005) 1-16.
- [5] J. F. Grosse-Oetringhaus, K. Reygers, "Charged-Particle Multiplicity in Proton-Proton Collisions", 2/24/2010, *J. Phys. G* 37 (2010) 083001.
- [6] R. A. Lacey *et al.*, "Has the QCD Critical Point Been Signaled by Observations at RHIC?", 2/14/2007, *Phys. Rev. Lett.* 98 (2007) 092301.
- [7] R. A. Lacey, "Indications for a critical end point in the phase diagram for hot and dense nuclear matter", Quark Matter 2015, Kobe, 9/28/2015.
- [8] L. Kumar (STAR Collaboration), "STAR Results from the RHIC Beam Energy Scan-I", 5/2/2013, *Nucl. Phys. A*, Vol. 904-905, pp. 256-263.
- [9] The 2015 Nuclear Science Advisory Committee (US Department of Energy), "Reaching for the Horizon - The 2015 Long Range Plan for Nuclear Science", 10/20/2015, [online, cit. 12/15/2018], <https://science.energy.gov/np/nsac/>.
- [10] R. Snellings, "Collective Expansion at the LHC: selected ALICE anisotropic flow measurements", 8/21/2014, *J. Phys. G: Nucl. Part. Phys.* 41 (2014) 12.
- [11] K. Aamodt *et al.* (ALICE Collaboration), "Centrality Dependence of the Charged-Particle Multiplicity Density at Midrapidity in Pb-Pb Collisions at  $\sqrt{s_{NN}} = 2.76$  TeV", 1/20/2011, *Phys. Rev. Lett.* 106, 032301.
- [12] M. Miller *et al.*, "Glauber Modeling in High Energy Nuclear Collisions", *Annual Review of Nuclear and Particle Science* 2007 57:1, 205-243.
- [13] Ch. Shen "Sketch of relativistic heavy-ion collisions", The Ohio State University, 8/6/2014, [online, cit. 10/16/2018], <https://u.osu.edu/vishnu/2014/08/06/sketch-of-relativistic-heavy-ion-collisions/>.

- [14] J. Adams *et al.* (STAR Collaboration), "Experimental and Theoretical Challenges in the Search for the Quark Gluon Plasma: The STAR Collaboration's Critical Assessment of the Evidence from RHIC Collisions", 8/8/2005, Nucl. Phys. A, Vol. 757 102-183.
- [15] I. Arsene *et al.* (BRAHMS Collaboration), "Quark-gluon plasma and color glass condensate at RHIC? The perspective from the BRAHMS experiment", 8/8/2005, Nucl. Phys. A, Vol. 757 1-27.
- [16] B. B. Back *et al.* (PHOBOS Collaboration), "The PHOBOS perspective on discoveries at RHIC", 8/8/2005, Nucl. Phys. A, Vol. 757 28-101.
- [17] K. Adcox *et al.* (PHENIX Collaboration), "Formation of dense partonic matter in relativistic nucleus-nucleus collisions at RHIC: Experimental evaluation by the PHENIX Collaboration", 8/8/2005, Nucl. Phys. A, Vol. 757 184-283.
- [18] L. Adamczyk *et al.* (STAR Collaboration), "Global  $\Lambda$  hyperon polarization in nuclear collisions: evidence for the most vortical fluid", 08/03/2017, Nature 548, 62 (2017).
- [19] M. Peskin *et al.*, "An Introduction to Quantum Field Theory", Westview, 1995, p. 552.
- [20] D. Abbaneo *et al.*, "Constraints on parton distribution functions and extraction of the strong coupling constant from the inclusive jet cross section in pp collisions at  $\sqrt{s} = 7$  TeV", 7/2/2015, Eur. Phys. J. C 75 (2015) 288.
- [21] Z. Fodor, S.D. Katz, "The Phase Diagram of Quantum Chromodynamics", 8/23/2009, Landolt-Boernstein Vol. 1-23A.
- [22] U. Heinz, M. Jacob, "Evidence for a New State of Matter: An Assessment of the Results from the CERN Lead Beam Programme", 2/16/2000, arXiv:nucl-th/0002042v1.
- [23] R.J. Reed, " $\Upsilon$  production at  $\sqrt{s_{NN}} = 200$  GeV in p+p and Au+Au collisions at STAR", Ph.D. Thesis, UC Davis, 2011.
- [24] D. d'Enterria, B. Betz, "High- $p_T$  Hadron Suppression and Jet Quenching", 12/21/2009, Lect. Notes Phys. 785, 285-339 (2010).
- [25] M. J. Tannenbaum, "How do quarks and gluons lose energy in the QGP?", 4/24/2014, J. Phys.: Conf. Ser. 589 (2015).
- [26] B. Z. Kopeilovich *et al.*, "Cronin Effect in Hadron Production off Nuclei", 1/3/2002, Phys. Rev. Lett. 88 (2002) 232303.
- [27] E. M. Levin *et al.*, "Baryon Anomaly in Heavy-Ion Collisions and Colour Correlations in QGP", 5/2/2013, Nucl. Phys. A, Vol. 904-905.
- [28] D. d'Enterria, "Jet Quenching", 4/19/2009, Landolt-Boernstein Vol. 1-23A.

- [29] T. Matsui, H. Satz, "J/ $\psi$  Suppression by Quark-gluon Plasma Formation", 10/9/1986, Phys. Let. B, Vol. 178.
- [30] X. Zhao, R. Rapp, "Charmonium in Medium: From Correlators to Experiment", 8/31/2010, Phys. Rev. C 82 (2010) 064905.
- [31] B. Trzeciak (STAR Collaboration), "J/ $\psi$  measurements in the STAR experiment", 12/23/2014, arXiv:1412.7345v1 [hep-ex].
- [32] H. Satz, "Colour Deconfinement and Quarkonium Binding", 3/2/2006, J. Phys. G 32 (2006) R25.
- [33] A. Andronic *et al.*, "Heavy-flavour and Quarkonium Production in the LHC Era: From Proton-proton to Heavy-ion Collisions", 12/1/2015, Eur. Phys. J. C 76 (2016) 107.
- [34] B.I. Abelev *et al.*, "Mass, Quark-number, and  $\sqrt{s_{NN}}$  Dependence of the Second and Fourth Flow Harmonics in Ultra-relativistic Nucleus-nucleus Collisions", 1/6/2007, Phys. Rev. C 75 (2007) 054906.
- [35] J. Adam *et al.*, "Higher harmonic flow coefficients of identified hadrons in Pb-Pb collisions at  $\sqrt{s_{NN}} = 2.76$  TeV", 6/20/2016, JHEP 1609 (2016) 164.
- [36] L. Adamczyk *et al.* (STAR Collaboration), "Beam-Energy Dependence of the Directed Flow of Protons, Antiprotons, and Pions in Au+Au Collisions", 4/23/2014, Phys. Rev. Lett. 112 (2014) 162301.
- [37] U. Heinz, "The strongly coupled quark-gluon plasma created at RHIC", 10/30/2008, J. Phys. A 42 (2009) 214003.
- [38] P. Huovinen, "Hydrodynamics of QCD", Excited QCD 2015, Tatranska Lomnica, 3/9/2015.
- [39] B. Schenke *et al.*, "Higher flow harmonics from (3+1)D event-by-event viscous hydrodynamics", 9/28/2011, Phys. Rev. C 85 (2012) 024901.
- [40] J. Xu, C. M. Ko, "Triangular flow in heavy ion collisions in a multiphase transport model", 3/27/2011, Phys. Rev. C 84 (2011) 014903.
- [41] F. G. Gardim *et al.*, "Anisotropic flow in event-by-event ideal hydrodynamic simulations of  $\sqrt{s_{NN}} = 200$  GeV Au+Au collisions", 3/13/2012, Phys. Rev. Lett. 109 (2012) 202302.
- [42] V. P. Konchakovski *et al.*, "Azimuthal anisotropies for Au+Au collisions in the parton-hadron transient energy range", 1/16/2012, Phys. Rev. C 85 (2012) 044922.
- [43] L. Adamczyk *et al.* (STAR Collaboration), "Third Harmonic Flow of Charged Particles in Au+Au Collisions at  $\sqrt{s_{NN}} = 200$  GeV", 7/15/2013, Phys. Rev. C 88 (2013) 014904.
- [44] J. Adams *et al.* (STAR Collaboration), "Azimuthal anisotropy in Au+Au collisions at  $\sqrt{s_{NN}} = 200$  GeV", 9/29/2004, Phys. Rev. C 72 (2005) 014904.

- [45] Yu L. Dokshitzer *et al.*, "On specific QCD properties of heavy quark fragmentation ('dead cone')", 12/9/1990, J. Phys. G: Nucl. Part. Phys. 17 (1991) 1602.
- [46] M. Cacciari *et al.*, "The  $p_T$  Spectrum in Heavy-Flavour Hadroproduction", 3/20/1998, JHEP 9805 (1998) 007.
- [47] L. Adamczyk *et al.* (STAR Collaboration), "Measurements of  $D^0$  and  $D^*$  production in p+p collisions at  $\sqrt{s} = 200$  GeV", 10/31/2012, Phys. Rev. D 86 (2012) 072013.
- [48] E. Scapparini (ALICE Collaboration), "Preliminary Physics Summary: Measurement of  $D^0$ ,  $D^+$ ,  $D^{*+}$  and  $D_s^+$  production in pp collisions at  $\sqrt{s} = 5.02$  TeV with ALICE", 5/10/2018, ALICE-PUBLIC-2018-006.
- [49] G. Aad *et al.* (ATLAS Collaboration), "Measurement of  $D^{*\pm}$ ,  $D^\pm$  and  $D^{\pm s}$  meson production cross sections in pp collisions at  $\sqrt{s} = 7$  TeV with the ATLAS detector", 4/25/2016, Nucl. Phys. B, Vol. 907 (2016) 717.
- [50] B. A. Kniehl, G. Kramer, I. Schienbein, and H. Spiesberger, "Inclusive charmed-meson production at the CERN LHC", Eur. Phys. J. C 72 (2012) 2082.
- [51] S. Frixione *et al.*, "A Positive-Weight Next-to-Leading-Order Monte Carlo for Heavy Flavour Hadroproduction", 7/20/2007, JHEP 0709 (2007) 126.
- [52] S. Frixione *et al.*, "Matching NLO QCD and parton showers in heavy flavour production", 9/10/2003, JHEP 08 (2003) 007.
- [53] A. M. Sirunyan *et al.* (CMS Collaboration), "Nuclear modification factor of  $D^0$  mesons in PbPb collisions at  $\sqrt{s_{NN}} = 5.02$  TeV", 7/10/2018, Phys. Lett. B 782 (2018) 474.
- [54] E. Scapparini (ALICE Collaboration), "Preliminary Physics Summary: Measurement of prompt  $D^0$ ,  $D^+$ ,  $D^{*+}$  and  $D_s^+$  production in p-Pb collisions at  $\sqrt{s_{NN}} = 5.02$  TeV", 7/5/2017, ALICE-PUBLIC-2017-008.
- [55] Z. Kang *et al.*, "Multiple scattering effects on heavy meson production in p+A collisions at backward rapidity", 9/8/2014, Phys. Lett. B 740 (2015) 23.
- [56] Q. Hu (ATLAS Collaboration), "Measurement of heavy flavor production and azimuthal anisotropy in small and large systems with ATLAS", Quark Matter 2018, Venice, 5/16/2018.
- [57] J. Vanek (STAR Collaboration), "Production of  $D^\pm$  Mesons in Au+Au Collisions at  $\sqrt{s_{NN}} = 200$  GeV Measured by the STAR Experiment", Quark Matter 2018, Venice, 5/15/2018.
- [58] J. Adam *et al.* (STAR Collaboration), "Centrality and transverse momentum dependence of  $D^0$ -meson production at mid-rapidity in Au+Au collisions at  $\sqrt{s_{NN}} = 200$  GeV", 12/26/2018, arXiv:1812.10224 [nucl-ex].

- [59] S. Cao *et al.*, "Energy loss, hadronization, and hadronic interactions of heavy flavors in relativistic heavy-ion collisions", 8/14/2015, Phys. Rev. C 92 (2015) 024907.
- [60] S. Cao *et al.*, "Heavy and light flavor jet quenching at RHIC and LHC energies", 2/10/2018, Phys. Lett. B 777 (2018) 255.
- [61] J. Adam *et al.* (ALICE Collaboration), "Transverse momentum dependence of D-meson production in Pb–Pb collisions at  $\sqrt{s_{NN}} = 2.76$  TeV", 9/23/2015, JHEP 03 (2016) 081.
- [62] S. Singha (STAR Collaboration), "Measurements of directed and elliptic flow for D0 and  $\bar{D}^0$  mesons using the STAR detector at RHIC", arXiv:1807.04771 [nucl-ex].
- [63] S. Chatterjee, P. Bozek, "Interplay of drag by hot matter and electromagnetic force on the directed flow of heavy quarks", 4/13/2018, arXiv:1804.04893 [nucl-th].
- [64] M. Nahrgang *et al.*, "Elliptic and triangular flow of heavy flavor in heavy-ion collisions", 1/20/2015, Phys. Rev. C 91 (2015) 014904.
- [65] M. He *et al.*, "Heavy-quark diffusion and hadronization in quark-gluon plasma", 7/10/2012, Phys. Rev. C 86 (2012) 014903.
- [66] L. He (STAR Collaboration), "Centrality dependence of  $D^0$  elliptic and triangular flow in Au+Au collisions at  $\sqrt{s_{NN}} = 200$  GeV at STAR", Nucl. Phys. A, Vol. 967 (2017) 616–619.
- [67] G. Luparello (ALICE Collaboration), " $D$ -meson  $v_2$  measurement in Pb-Pb collisions at 5.02 TeV with ALICE", Quark Matter 2018, Venice, 5/15/2018.
- [68] M. Nahrgang *et al.*, "Influence of hadronic bound states above  $T_c$  on heavy-quark observables in Pb + Pb collisions at the CERN Large Hadron Collider", 1/22/2014, Phys. Rev. C 89 (2014) 014905.
- [69] T. Song *et al.*, "Charm production in Pb + Pb collisions at energies available at the CERN Large Hadron Collider", 3/10/2016, Phys. Rev. C 93 (2016) 034906.
- [70] A. Berardo *et al.*, "Heavy flavors in heavy-ion collisions: quenching, flow and correlations", 3/14/2015, Eur. Phys. J. C 75 (2015) 121.
- [71] A. M. Sirunyan *et al.* (CMS Collaboration), "Elliptic flow of charm and strange hadrons in high-multiplicity pPb collisions at  $\sqrt{s_{NN}} = 8.16$  TeV", 8/21/2018, Phys. Rev. Lett. 121 (2018) 082301.
- [72] K. Walsh, "Accelerating Particles Accelerates Science — With Big Benefits for Society", 3/13/2013, [online, cit. 12/6/2018], <https://www.bnl.gov/rhic/news2/news.asp?a=3758&t=today>.
- [73] J. G. Alessi *et al.*, "Design of EBIS for RHIC", Proceedings of the 2003 Particle Accelerator Conference, 10.1109/PAC.2003.1288848.

- [74] M. Harrison *et al.*, "RHIC project overview", Nucl. Instrum. Meth., Vol. A499, pp. 235-244, 2003.
- [75] Accelerator Division, Collider-Accelerator Department "RHIC Configuration Manual", 2006, [online, cit. 12/20/2018], <https://www.bnl.gov/cad/accelerator/docs/pdf/RHICConfManual.pdf>.
- [76] Accelerators, Cryogenics and Magnetism Division, Institute of Research into the Fundamental Laws of the Universe, "Development of superconducting accelerating structures", 3/19/2008, [online, cit. 12/5/2018], [http://irfu.cea.fr/dacm/en/Phoce/Vie\\_des\\_labos/Ast/ast\\_visu.php?id\\_ast=2407](http://irfu.cea.fr/dacm/en/Phoce/Vie_des_labos/Ast/ast_visu.php?id_ast=2407).
- [77] G. Robert-Demolaize *et al.*, "RHIC Performance for FY2014 Heavy Ion Run", Proceedings of IPAC2014, Dresden, Germany.
- [78] W. Fischer, "Run Overview of the Relativistic Heavy Ion Collider", 10/23/2018, [online, cit. 10/25/2018], <http://www.agsrhichome.bnl.gov/RHIC/Runs/>.
- [79] S. Campbell (sPHENIX Collaboration), "sPHENIX: The next generation heavy ion detector at RHIC", 11/9/2016, J. Phys.: Conf. Ser. 832 012012.
- [80] "RHIC - Brookhaven National Laboratory", [online, cit. 12/3/2018], <https://www.bnl.gov/rhic/>.
- [81] H. Hahn *et al.*, "The RHIC design overview", Nucl. Instrum. Meth., Vol. A499, pp. 245–263, 2003.
- [82] M. Gazdzicki *et al.*, "Recommendations of the Nuclear and Particle Physics Program Advisory Committee, Brookhaven National Laboratory", 6/7-8/2018, [online, cit. 10/26/2018], <https://drupal.star.bnl.gov/STAR/system/files/BNL%20PAC%202018%20Recommendations%20-%20Final-1.pdf>.
- [83] A. Accardi *et al.*, "Electron Ion Collider: The Next QCD Frontier - Understanding the glue that binds us all", 9/8/2016, Eur. Phys. J. A 52 (2016) 268.
- [84] K. Oh (STAR Collaboration), "Measurements of Charm and Bottom Productions in Semi-leptonic Channels at STAR", Quark Matter 2015, Kobe, 9/29/2015.
- [85] H. Bichsel, "Comparison of Bethe-Bloch and Bichsel functions", 3/3/2002, STAR Note SN0439.
- [86] M. Anderson *et al.*, "The STAR Time Projection Chamber: A Unique Tool for Studying High Multiplicity Events at RHIC", Nucl. Instrum. Meth., Vol. A499, pp. 659–678, 2003.
- [87] "The STAR Experiment", [online, cit. 12/18/2018], <https://drupal.star.bnl.gov/STAR>
- [88] F. Geurts *et al.*, "Proposal for a Large Area Time of Flight System for STAR", 5/24/2004, STAR Note SN0621.

- [89] M. Beddo *et al.*, "The STAR Barrel Electromagnetic Calorimeter", Nucl. Instrum. Meth. Vol. A499, pp. 725-739, 2003.
- [90] W.J. Llope *et al.*, "The STAR Vertex Position Detector", Nucl. Instrum. Meth., Vol. A759, pp 23-28, 2014.
- [91] D. Beavis *et al.*, "The STAR Heavy Flavor Tracker Technical Design Report", 6/30/2011, STAR Note SN0600.
- [92] L. Adamczyk *et al.* (STAR Collaboration), "Measurement of  $D^0$  Azimuthal Anisotropy at Midrapidity in Au+Au Collisions at  $\sqrt{s_{NN}} = 200$  GeV", 5/26/2017, Phys. Rev. Lett. 118, 212301 (2017).
- [93] G. Contin *et al.*, "The STAR MAPS-based PiXeL detector", Nucl. Instrum. Meth., Vol. A907, pp 60-80, 2018.
- [94] T.C. Huang *et al.*, "Muon Identification with Muon Telescope Detector at the STAR Experiment", Nucl. Instrum. Meth., Vol. A833, pp 88-93, 2016.
- [95] M. Lisa *et al.*, "An Event Plane Detector for STAR", [online, cit. 10/30/2018], [https://drupal.star.bnl.gov/STAR/system/files/Construction\\_Proposal\\_0.pdf](https://drupal.star.bnl.gov/STAR/system/files/Construction_Proposal_0.pdf).
- [96] Z. Xu *et al.* (STAR Collaboration), "A Proposal for STAR Inner TPC Sector Upgrade (iTTPC)", 6/9/2015, STAR Note SN0619.
- [97] F. Geurts *et al.* (STAR Collaboration & CBM Collaboration eTOF Group), "Physics Program for the STAR/CBM eTOF Upgrade", 9/16/2016, arXiv:1609.05102 [nucl-ex].
- [98] O.D. Tsai *et al.*, "Development of a forward calorimeter system for the STAR experiment", J. Phys.: Conf. Ser. 587 (2015) 012053.
- [99] H.U. Bengtsson *et al.*, "The Lund Monte Carlo for High  $p_T$  Physics", Comput. Phys. Commun. 34 251 LU TP 84-3, CERN-TH-3820, 1985.
- [100] D.J. Lange, "The EvtGen particle decay simulation package", Nucl. Instrum. Meth., Vol. A462, pp 152-155, 2001.
- [101] X. Wang, M. Gyulassy, "HIJING 1.0: A Monte Carlo Program for Parton and Particle Production in High Energy Hadronic and Nuclear Collisions", Comput. Phys. Commun. 83:307, 1994.
- [102] S. Agostinelli *et al.*, "Geant4 — a simulation toolkit", Nucl. Instrum. Meth., Vol. A506, pp 250-303, 2003.
- [103] L. Adamczyk *et al.* (STAR Collaboration), Phys. Rev. Lett. 113, 142301 (2014) (Erratum: arXiv:1809.08737 [nucl-ex]).
- [104] A. Hoecker *et al.*, "TMVA - Toolkit for Multivariate Data Analysis", 3/4/2007, CERN-OPEN-2007-007.

# Appendices

# Appendix A

## Variables Distributions

The distributions of variables used for this analysis - with the position of the cuts marked by red lines - are shown in Figs. A.1 - A.9. Please note that these cuts were not tuned in any way by machine-learning techniques.

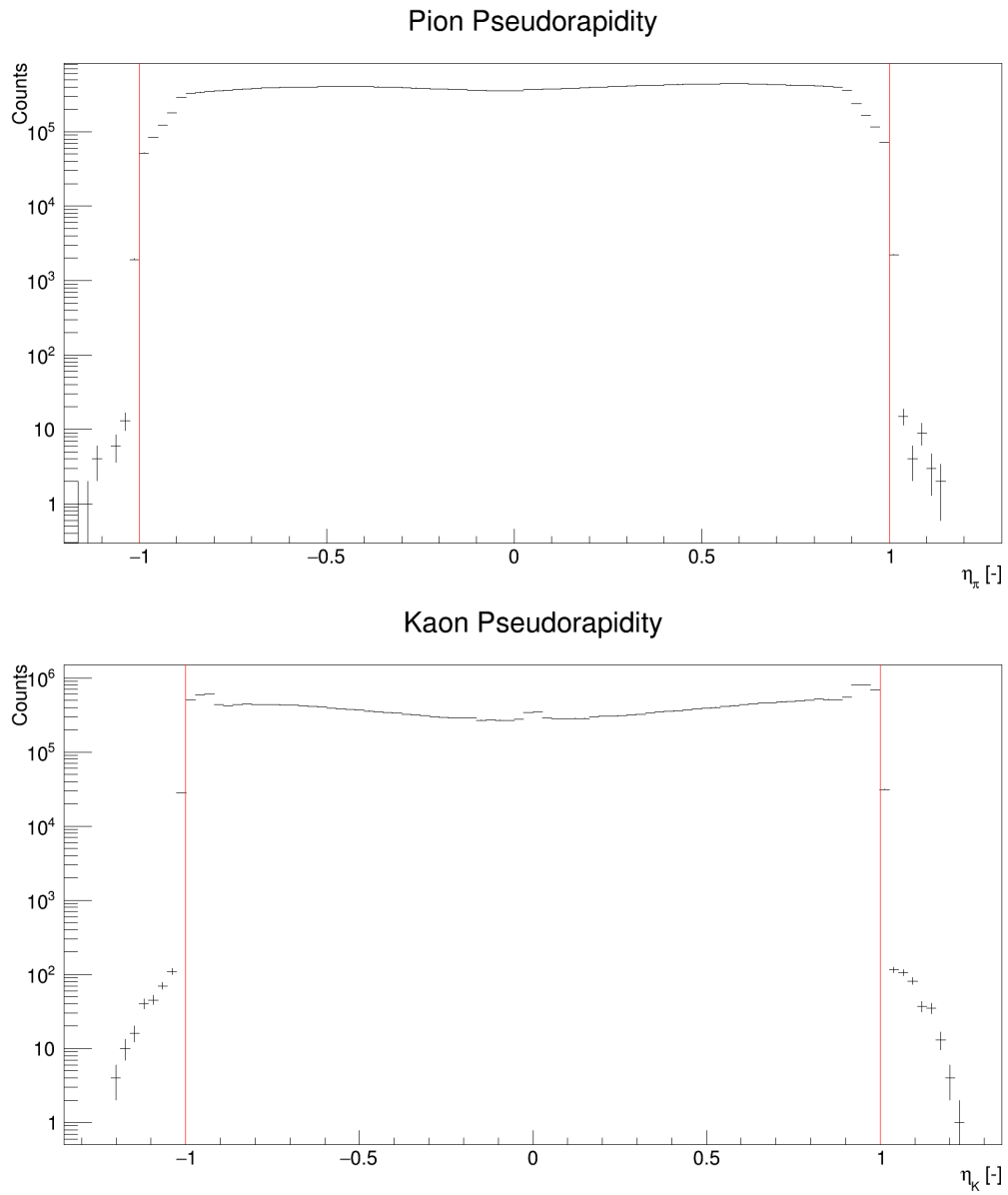


Figure A.1: Pseudorapidity distribution of pions (top) and kaons (bottom) with red lines drawn to show the cut. Values within these lines were accepted.

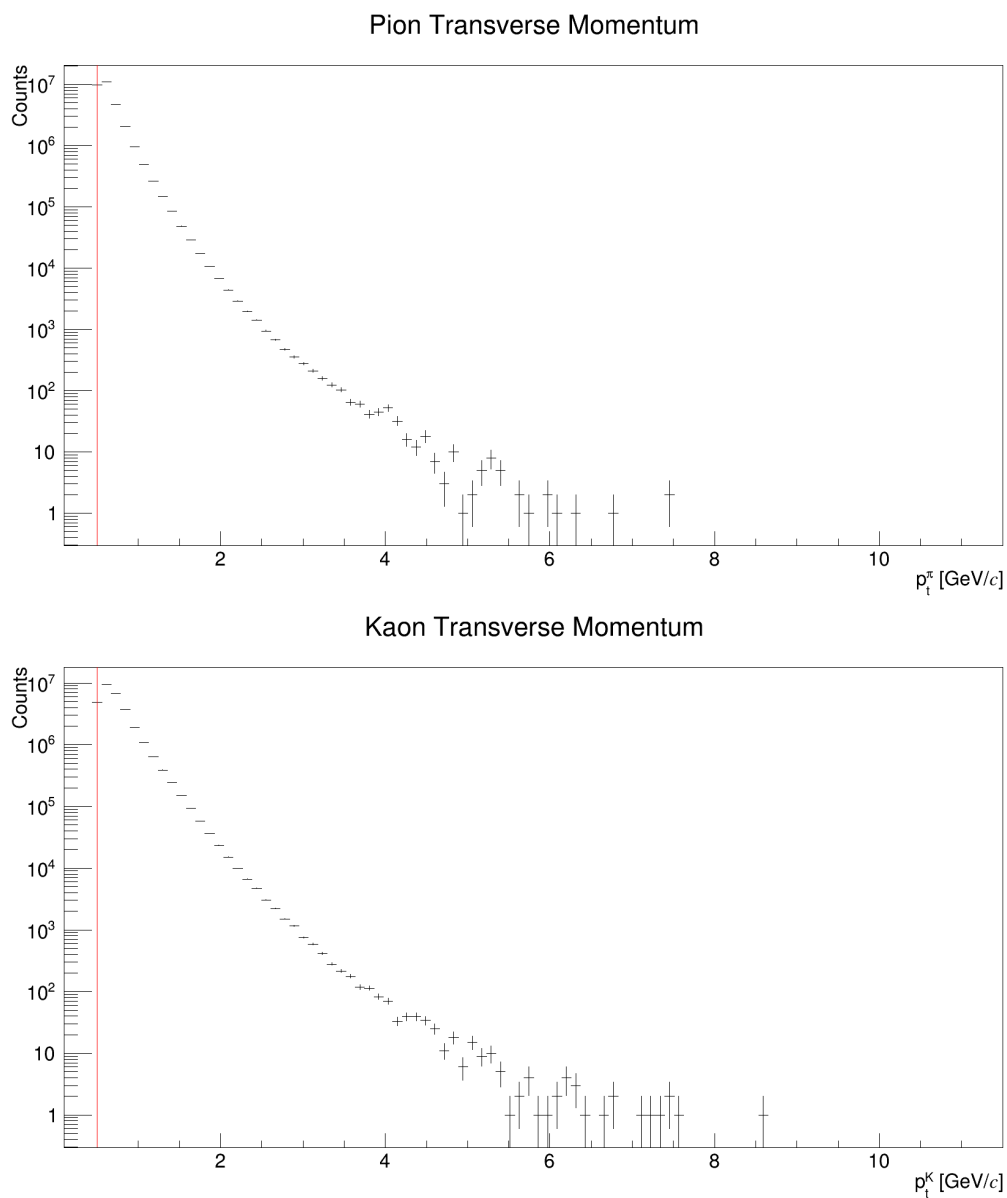


Figure A.2: Transverse momentum distribution of pions (top) and kaons (bottom) with red line drawn to show the cut. Values beyond this line were accepted.

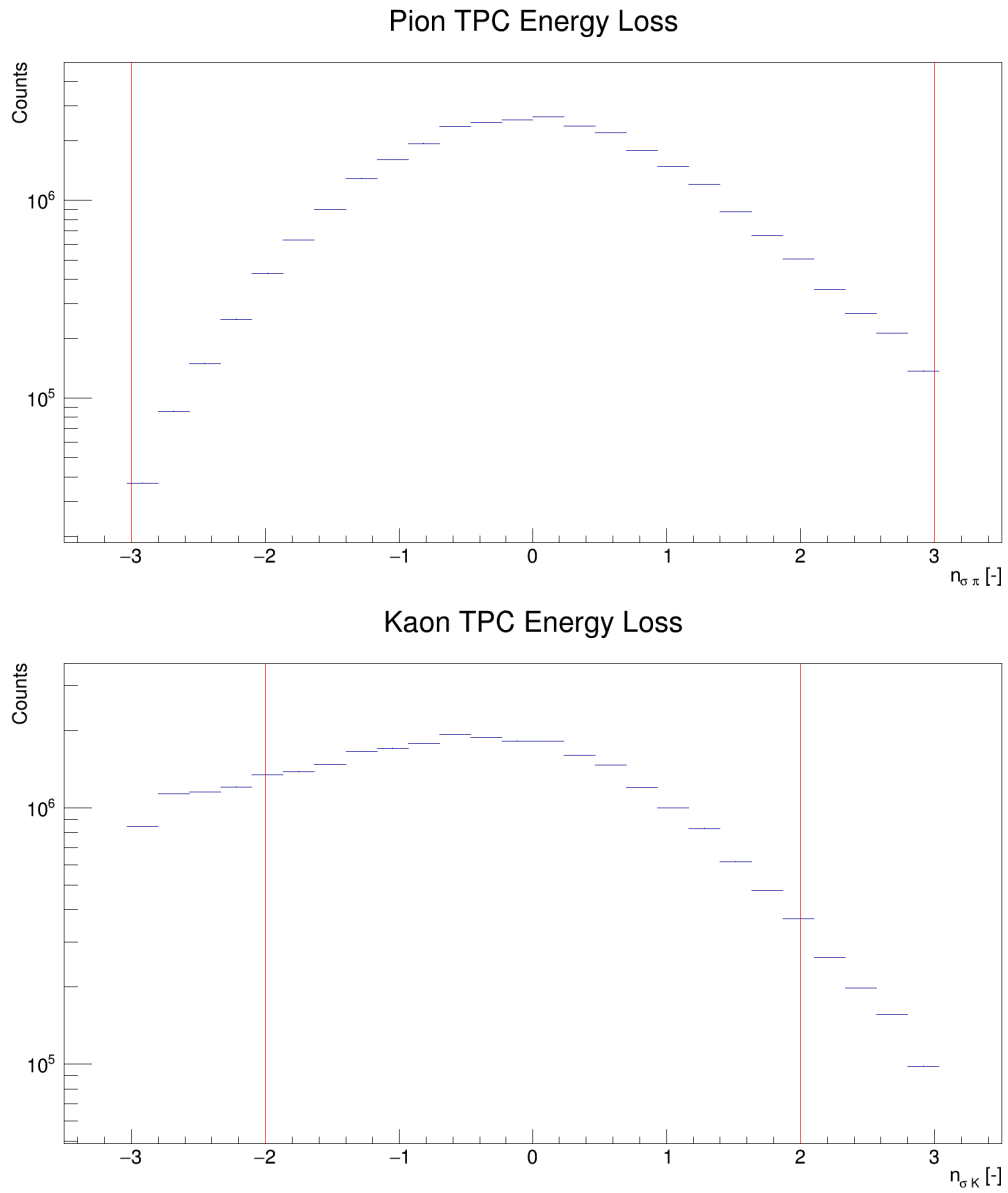


Figure A.3: Energy loss deviation distribution of pions (top) and kaons (bottom) as measured by the TPC, with red lines drawn to show the cut. Values within these lines were accepted.

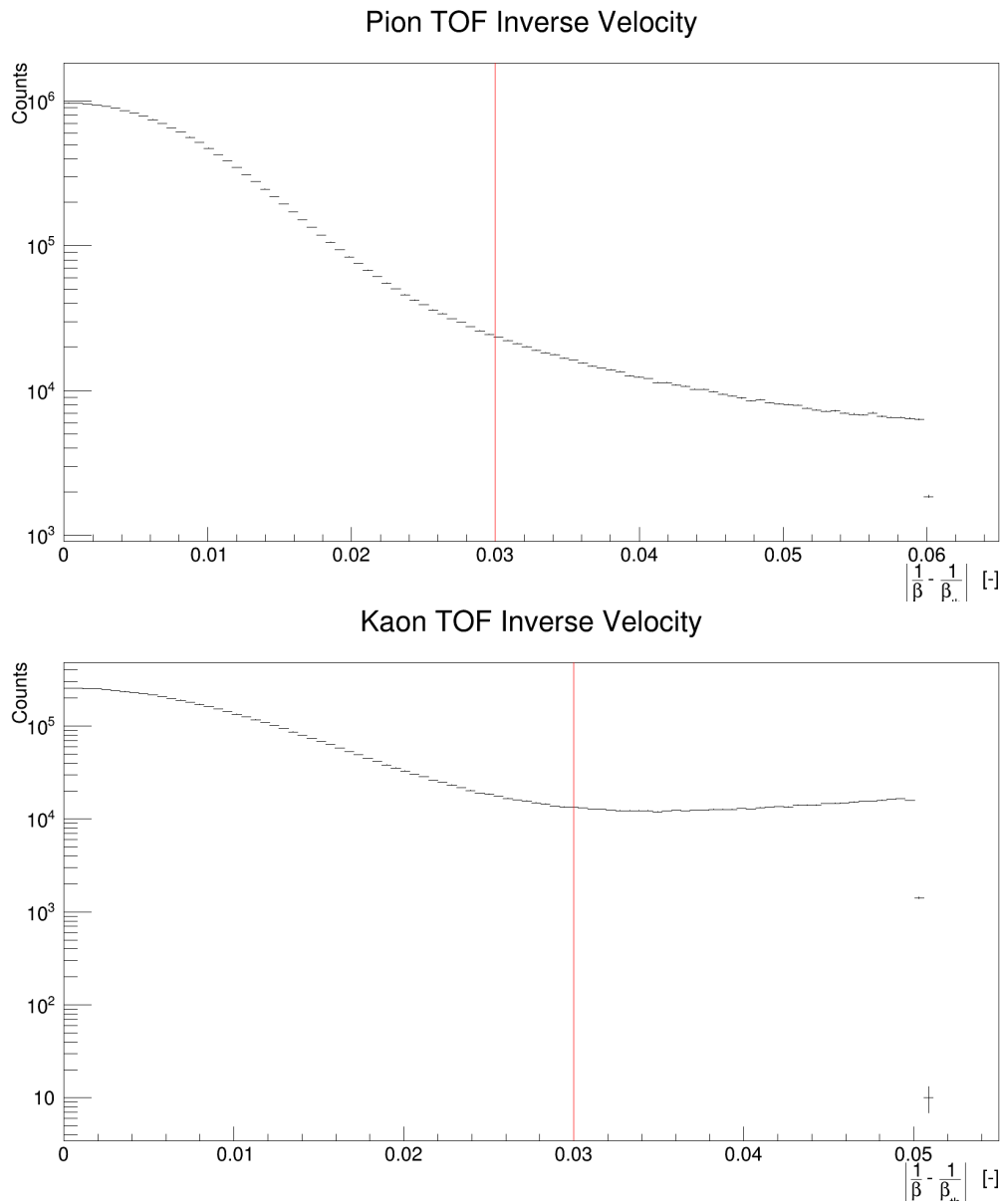


Figure A.4: Inverse velocity deviation distribution of pions (top) and kaons (bottom) as measured by the ToF detector. Values before the red line were accepted

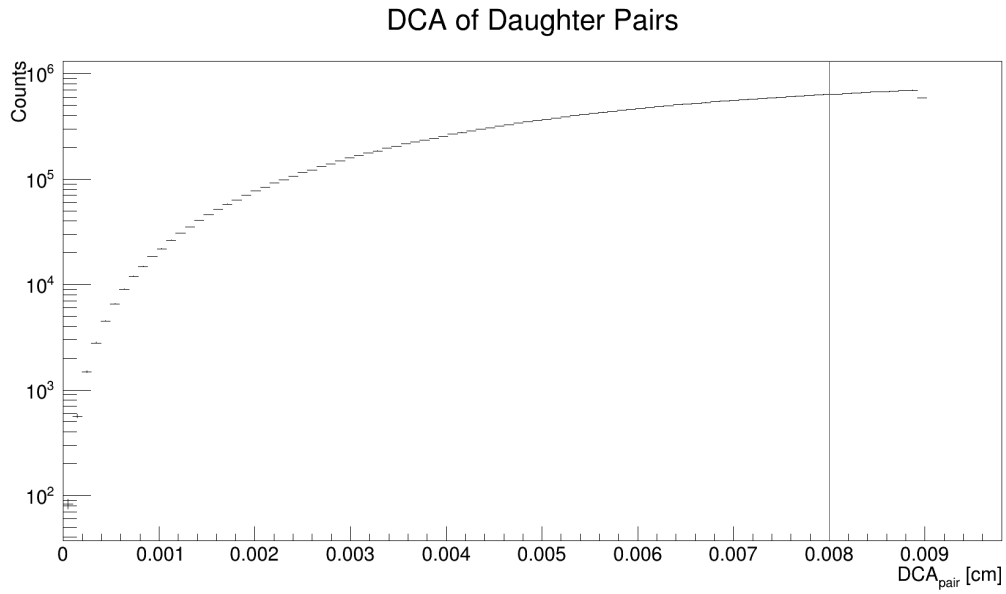


Figure A.5: Distribution of the DCA of daughter pairs. Values to the left of the red line were accepted.

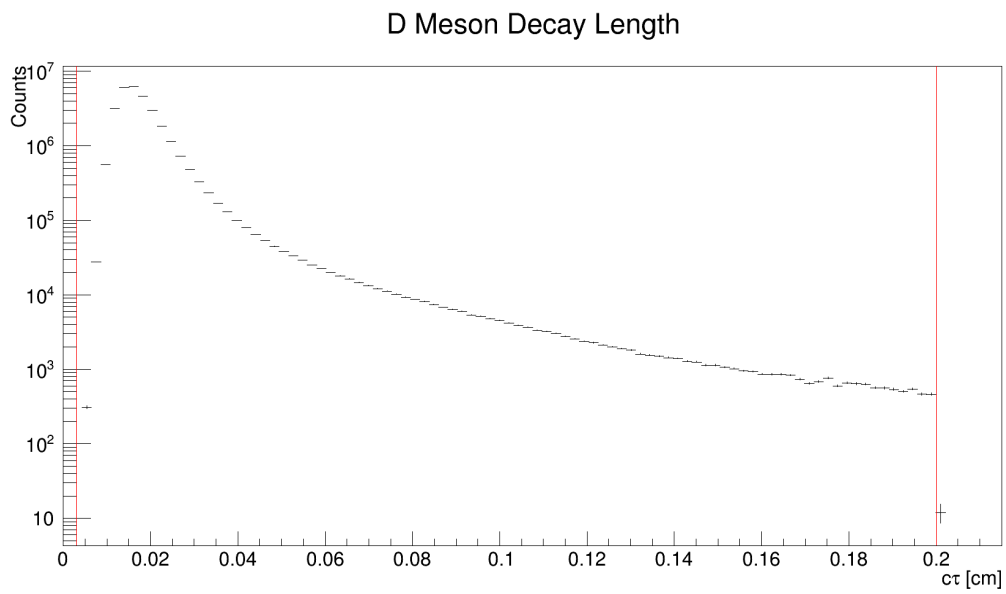


Figure A.6: Distribution of the decay length of the  $D^\pm$  meson. Values within the red lines were accepted.

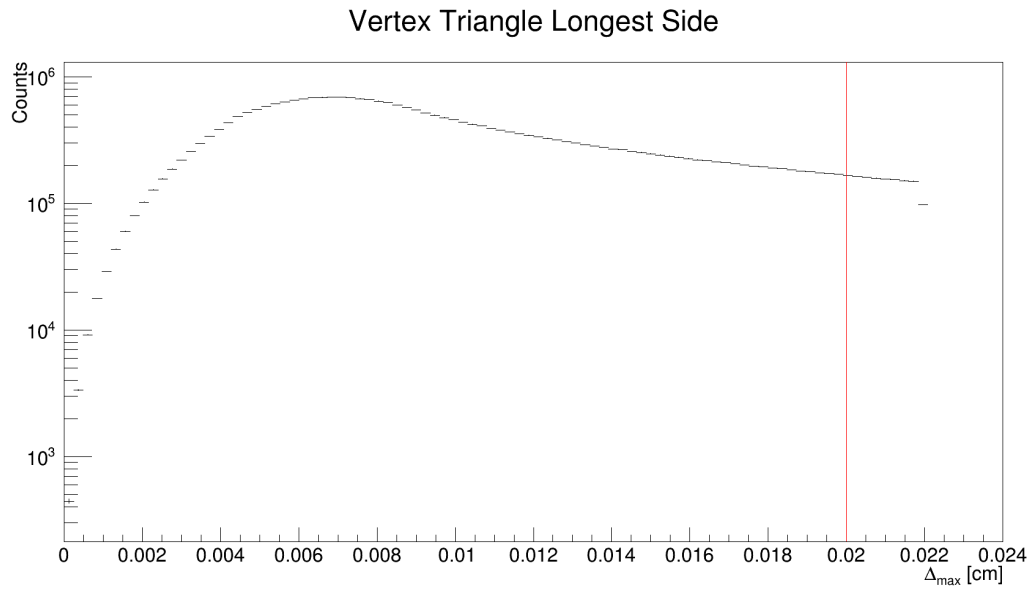


Figure A.7: Vertex triangle longest side distribution with cut shown as the red line. Values to the left of this line were accepted.

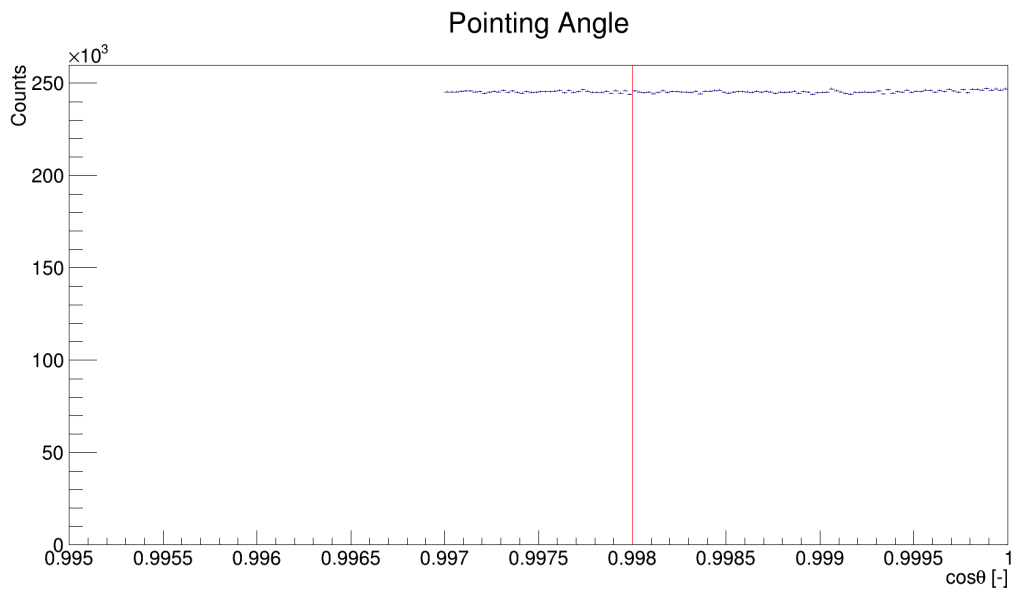


Figure A.8: The distribution of the cosine of the pointing angle beyond the cut value.

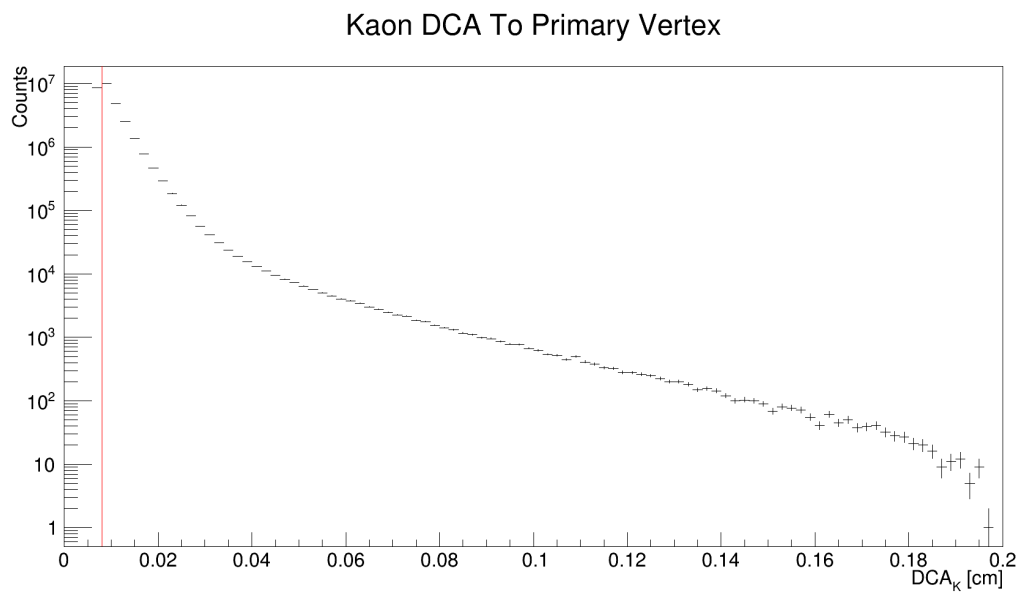
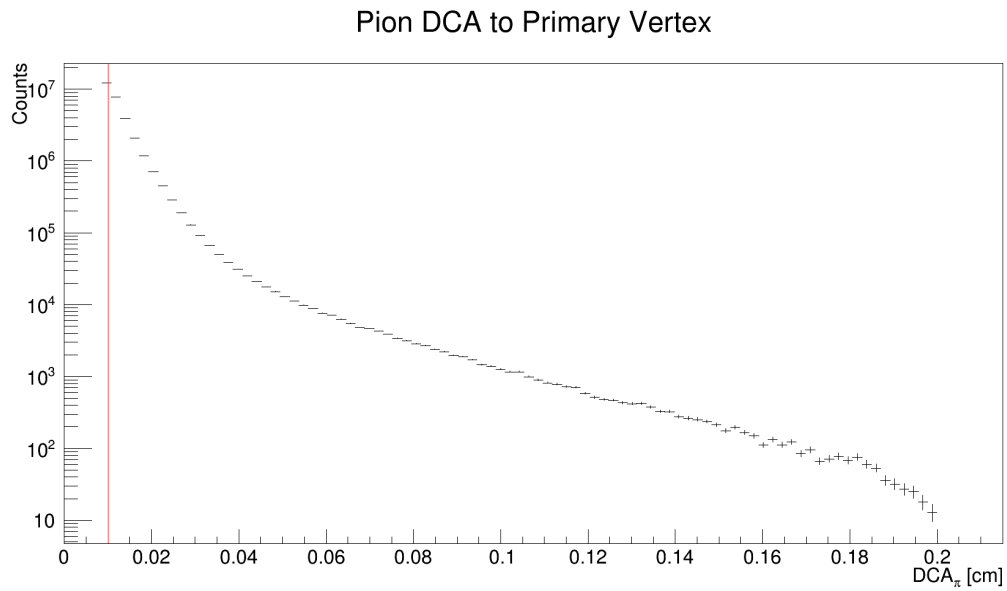


Figure A.9: DCA to the primary vertex distribution of pions (top) and kaons (bottom) with red line drawn to show the cut. Values beyond this line were accepted.

# Appendix B

## Invariant Mass Distributions

The invariant mass distributions for  $K\pi\pi$  triplets in 4 centrality and 12 transverse momentum bins are shown in figures B.1 - B.12. These distributions were obtained during the process of raw yield extraction described in Sec. 4.3. The correct-sign distributions are fitted with a sum of a Gaussian and a first order polynomial function. The wrong-sign combinations are shown already scaled with the correct-sign-to-background ratio. The signal distributions are fitted with a Gaussian function and contain information about calculated raw yield and the peak significance. Peaks with significance lower than 3 were considered insignificant. The peaks are clearly visible in vast majority of the bins, showing high precision of the reconstruction.

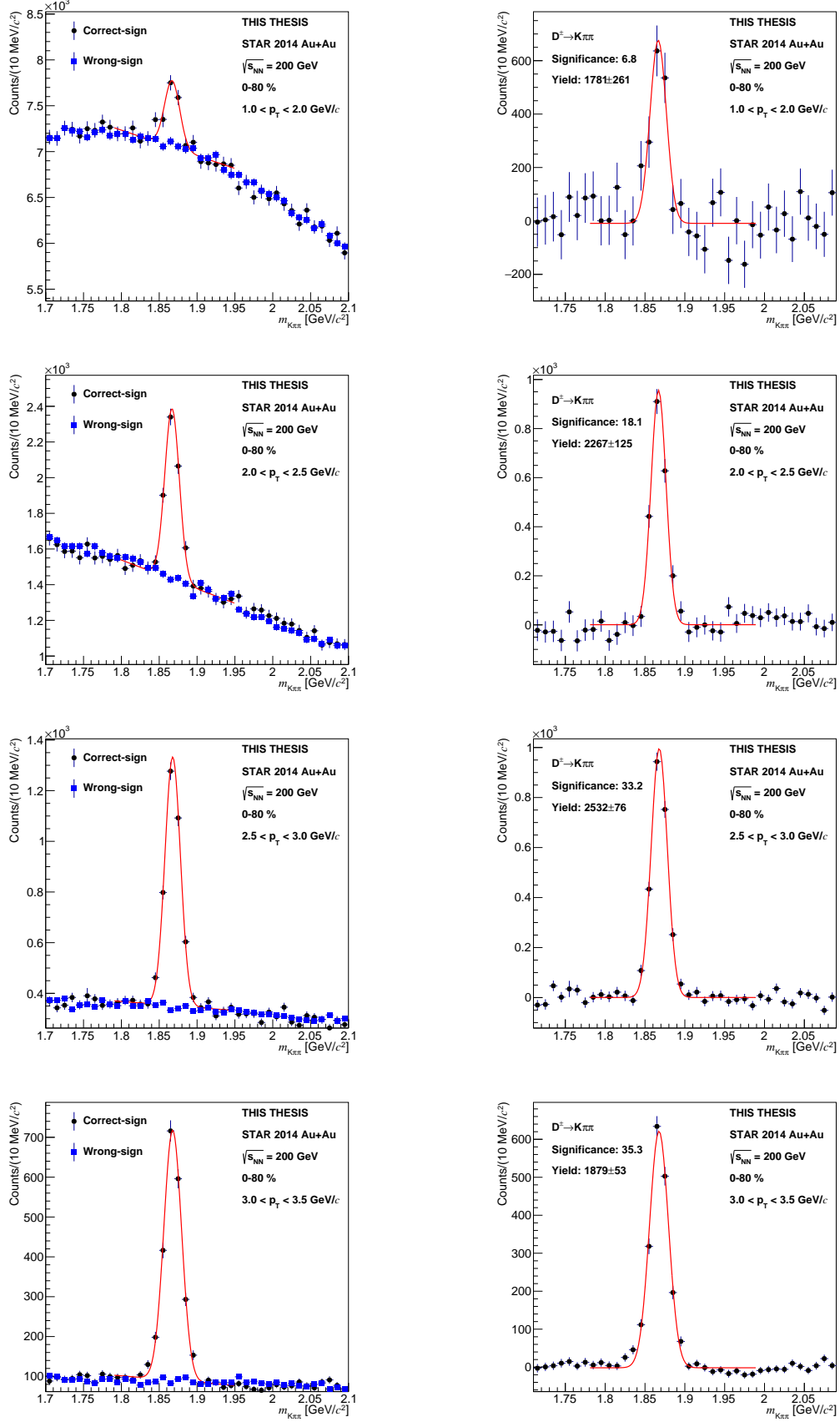


Figure B.1: Invariant mass distribution of  $K\pi\pi$  triplets before (left panel) and after (right panel) background subtraction for the 0-80 % centrality range and  $p_T$  bins: 1-2, 2-2.5, 2.5-3 and 3-3.5  $\text{GeV}/c$ .

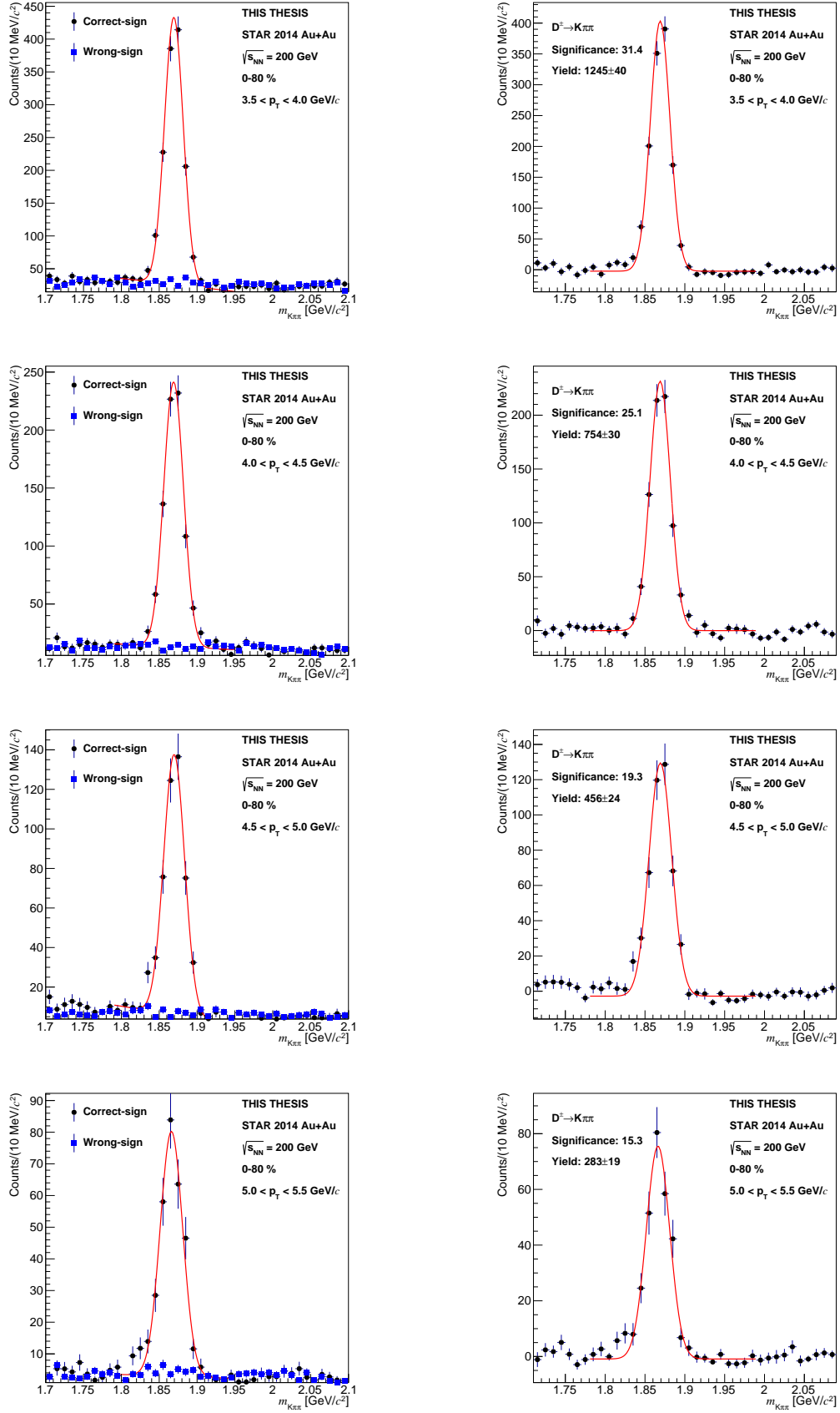


Figure B.2: Invariant mass distribution of  $K\pi\pi$  triplets before (left panel) and after (right panel) background subtraction for the 0-80 % centrality range and  $p_T$  bins: 3.5-4, 4-4.5, 4.5-5 and 5-5.5  $\text{GeV}/c$ .

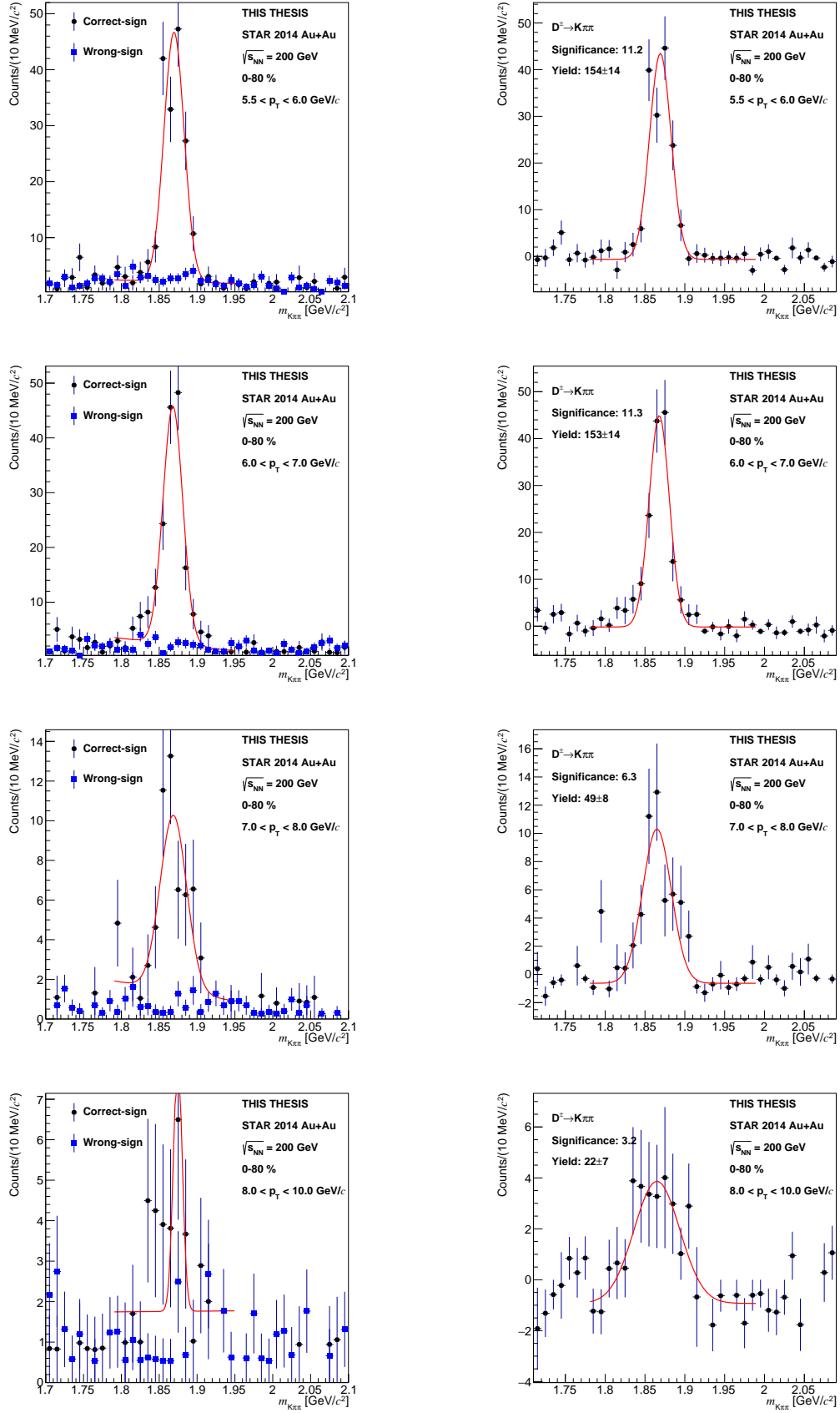


Figure B.3: Invariant mass distribution of  $K\pi\pi$  triplets before (left panel) and after (right panel) background subtraction for the 0-80 % centrality range and  $p_T$  bins: 5.5-6, 6-7, 7-8 and 8-10  $\text{GeV}/c$ .

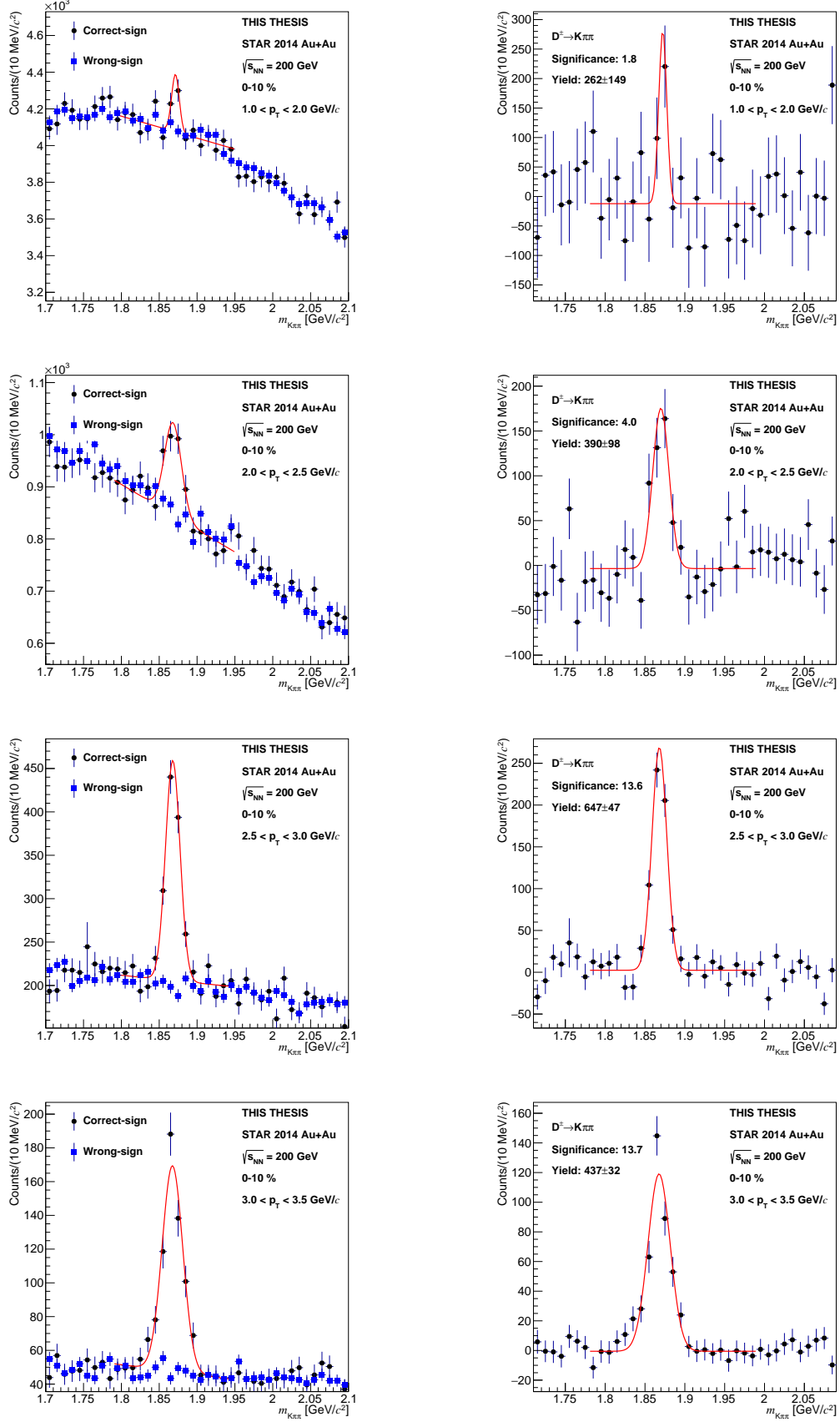


Figure B.4: Invariant mass distribution of  $K\pi\pi$  triplets before (left panel) and after (right panel) background subtraction for the 0-10 % centrality range and  $p_T$  bins: 1-2, 2-2.5, 2.5-3 and 3-3.5  $\text{GeV}/c$ .

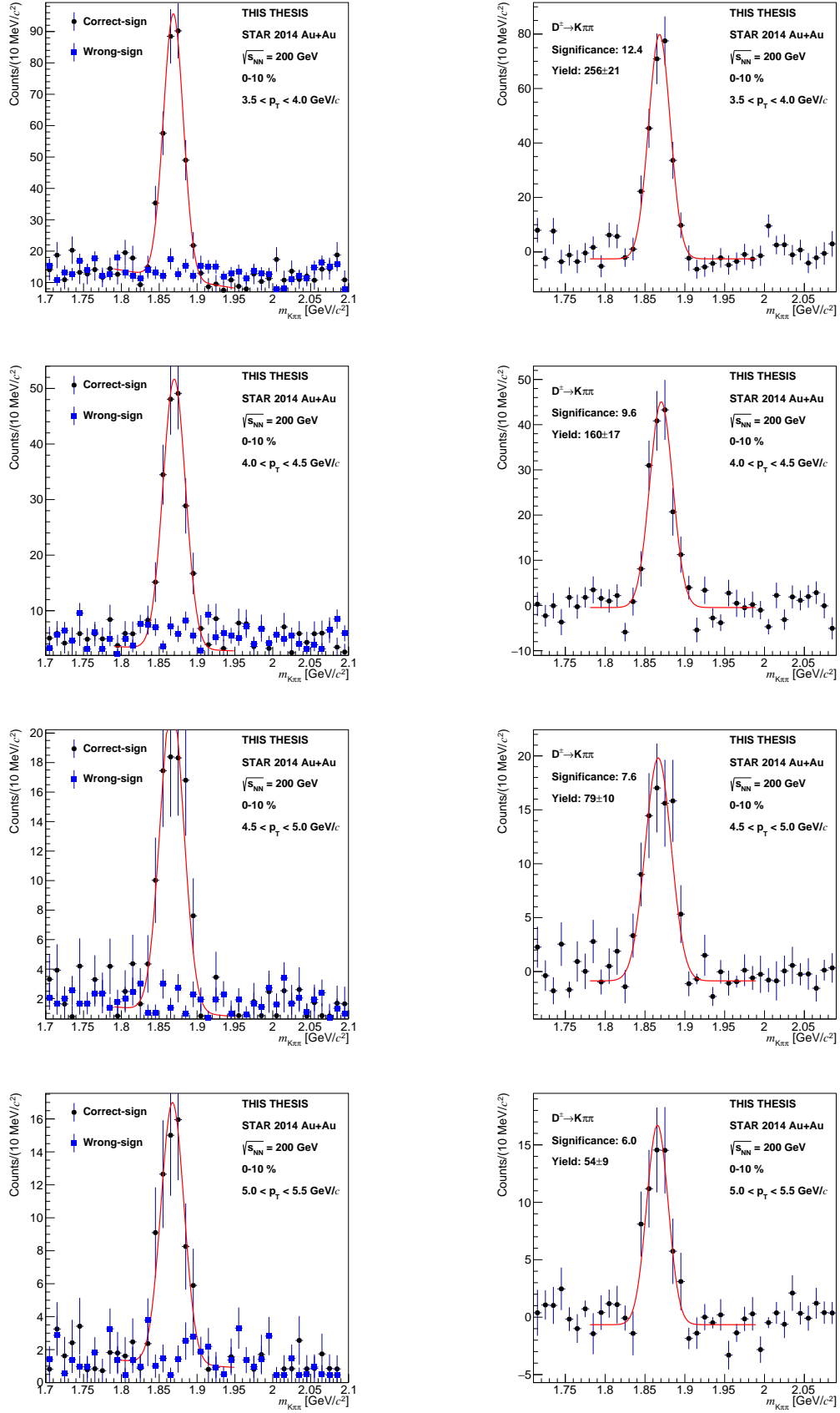


Figure B.5: Invariant mass distribution of  $K\pi\pi$  triplets before (left panel) and after (right panel) background subtraction for the 0-10 % centrality range and  $p_T$  bins: 3.5-4, 4-4.5, 4.5-5 and 5-5.5  $\text{GeV}/c$ .

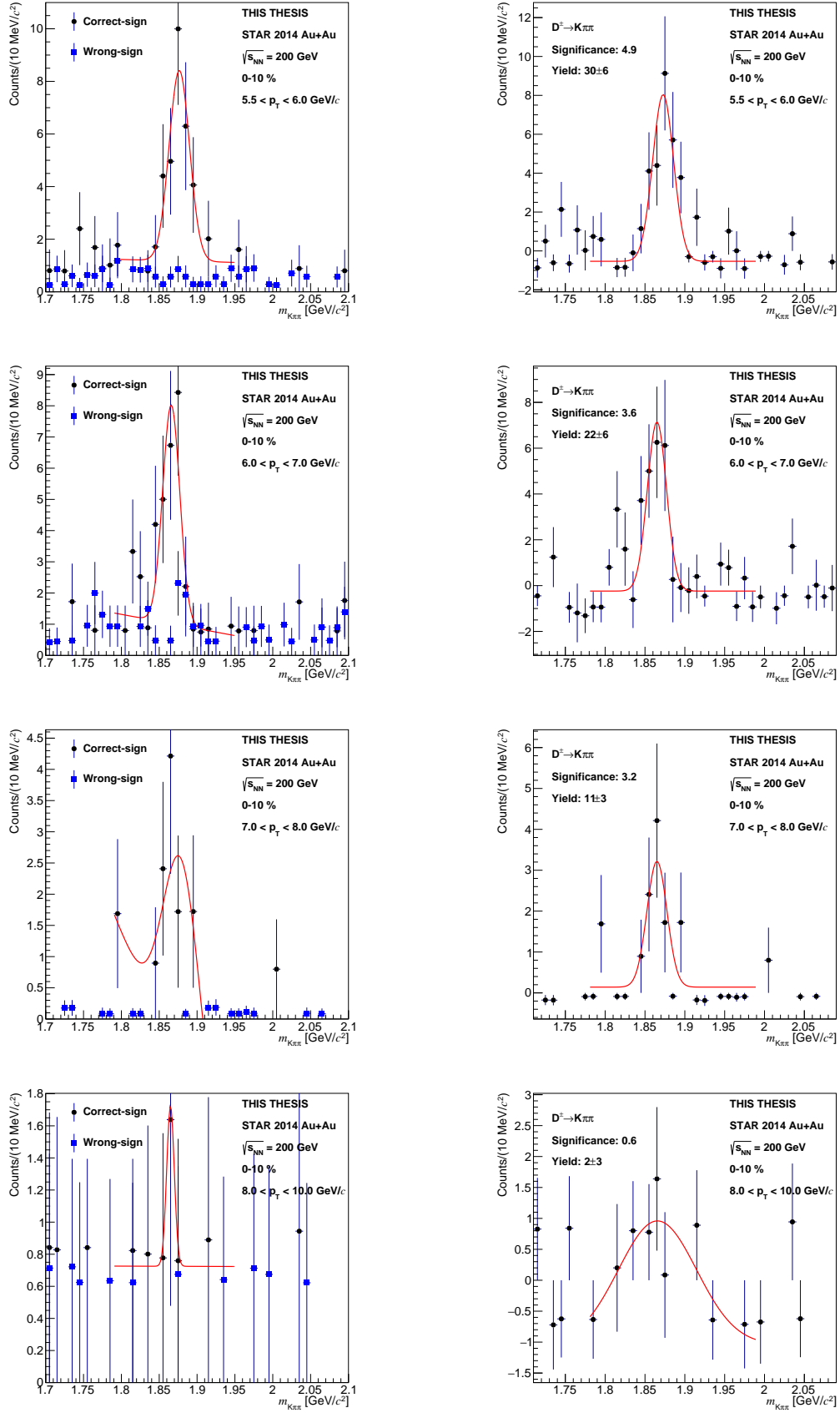


Figure B.6: Invariant mass distribution of  $K\pi\pi$  triplets before (left panel) and after (right panel) background subtraction for the 0-10 % centrality range and  $p_T$  bins: 5.5-6, 6-7, 7-8 and 8-10 GeV/c.

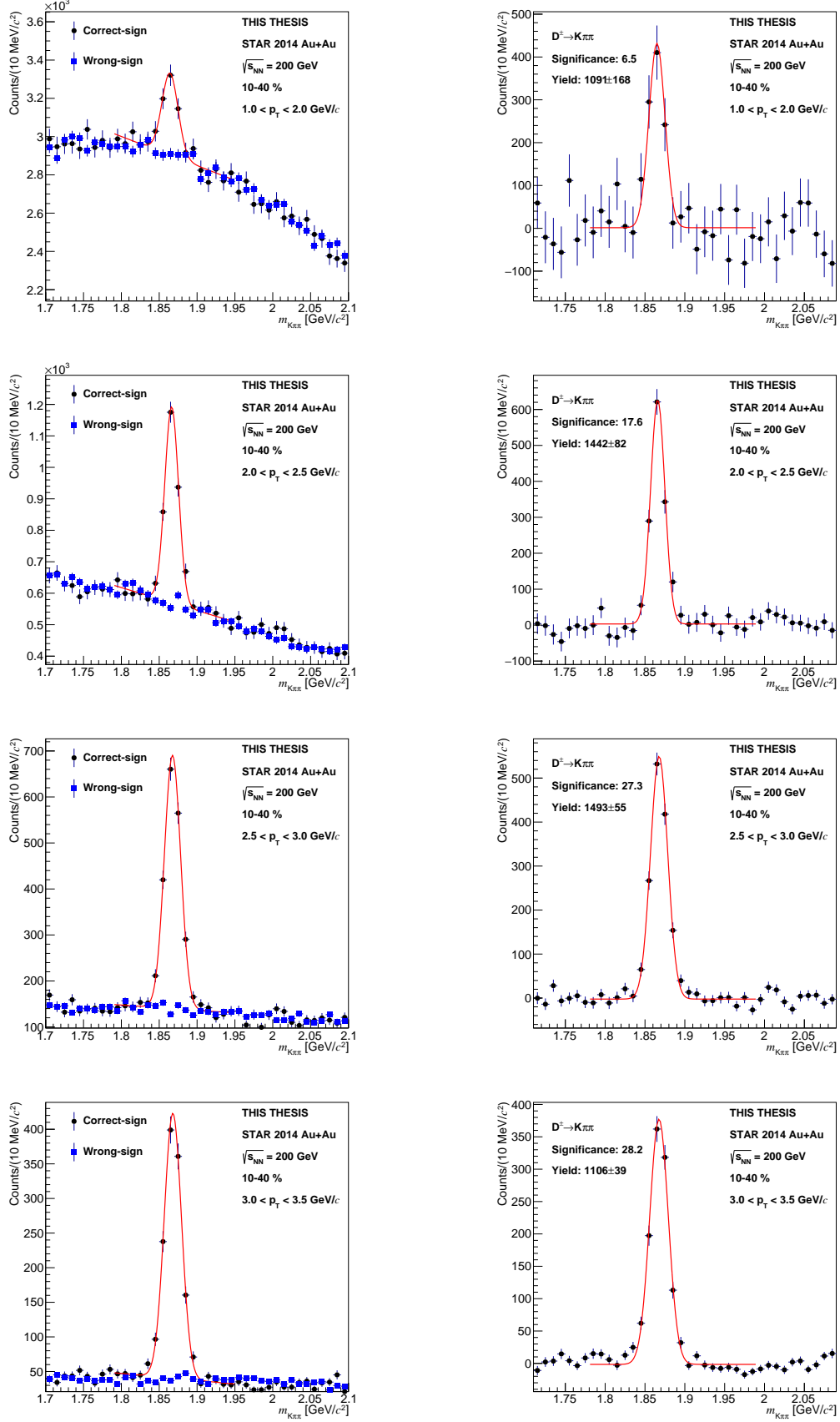


Figure B.7: Invariant mass distribution of  $K\pi\pi$  triplets before (left panel) and after (right panel) background subtraction for the 10-40 % centrality range and  $p_T$  bins: 1-2, 2-2.5, 2.5-3 and 3-3.5  $\text{GeV}/c$ .

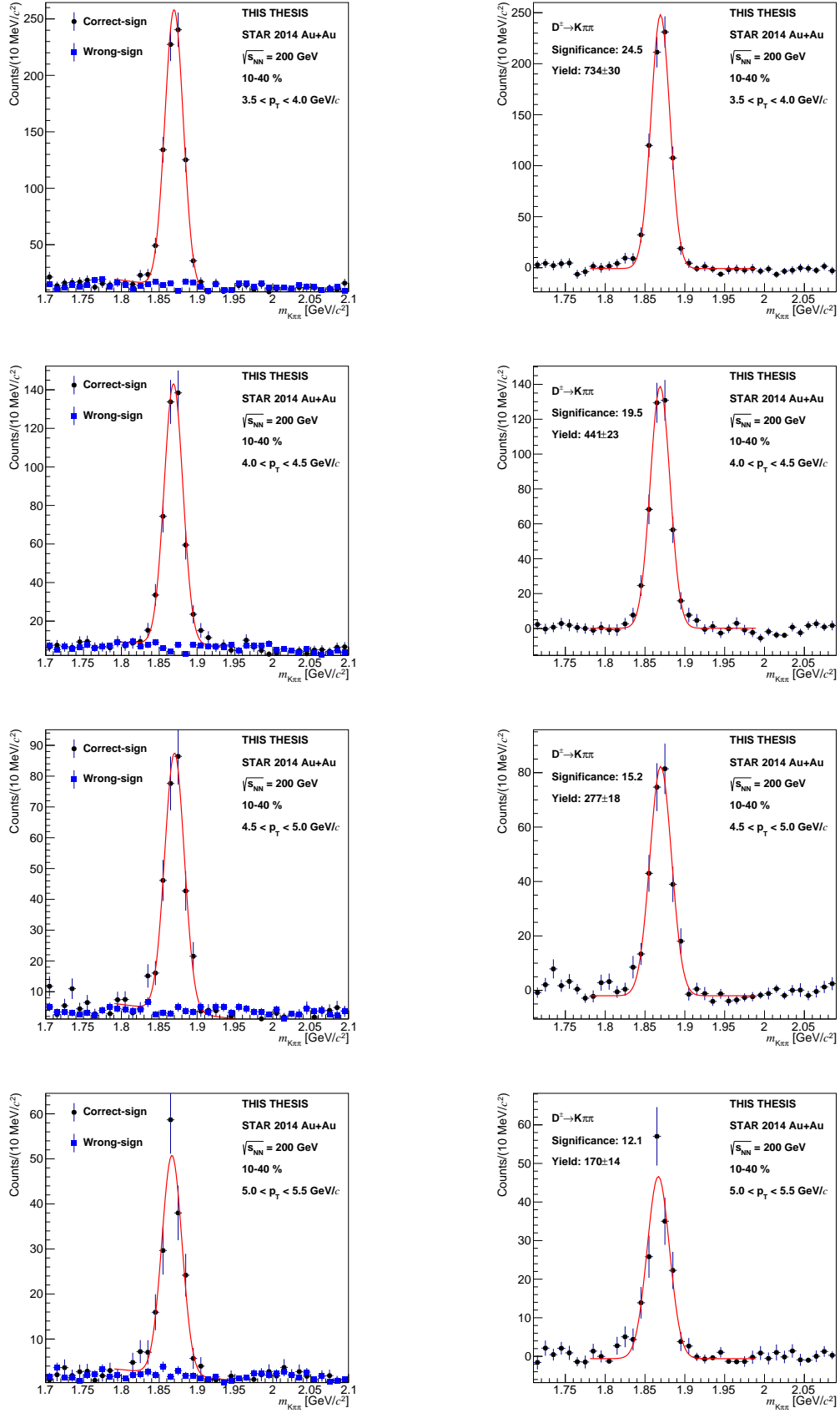


Figure B.8: Invariant mass distribution of  $K\pi\pi$  triplets before (left panel) and after (right panel) background subtraction for the 10-40 % centrality range and  $p_T$  bins: 3.5-4, 4-4.5, 4.5-5 and 5-5.5 GeV/c.

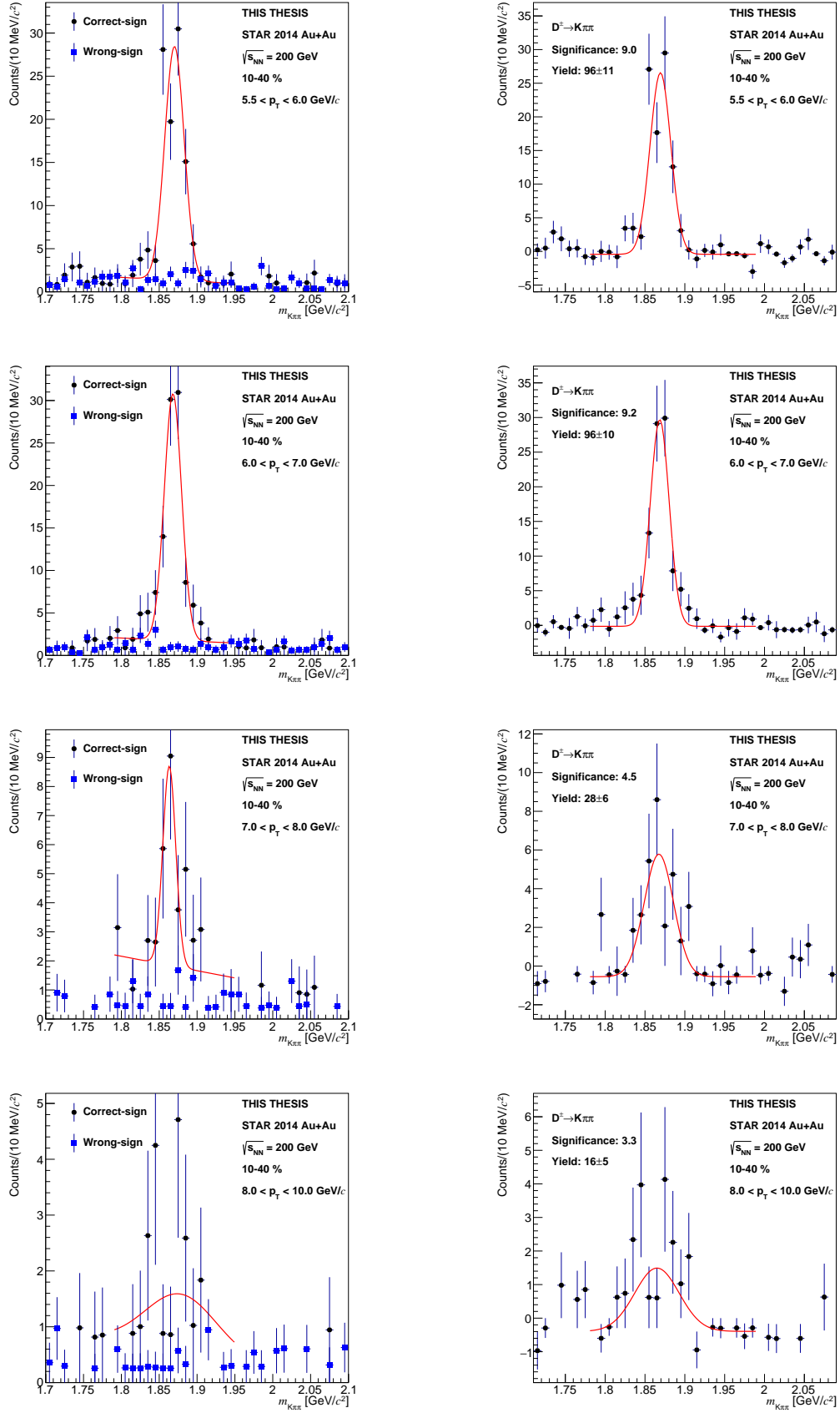


Figure B.9: Invariant mass distribution of  $K\pi\pi$  triplets before (left panel) and after (right panel) background subtraction for the 10-40 % centrality range and  $p_T$  bins: 5.5-6, 6-7, 7-8 and 8-10  $\text{GeV}/c$ .

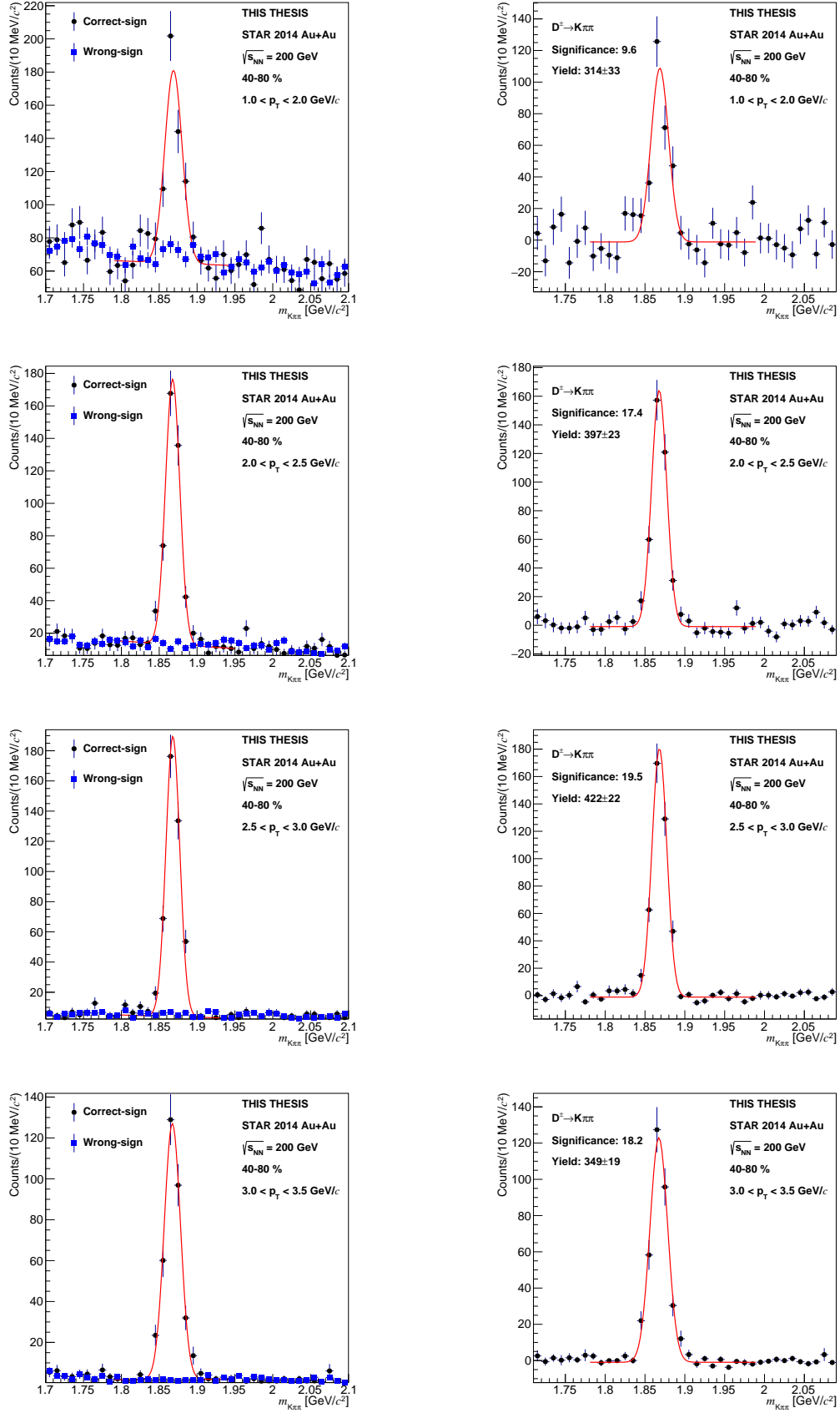


Figure B.10: Invariant mass distribution of  $K\pi\pi$  triplets before (left panel) and after (right panel) background subtraction for the 40-80 % centrality range and  $p_T$  bins: 1-2, 2-2.5, 2.5-3 and 3-3.5  $\text{GeV}/c$ .

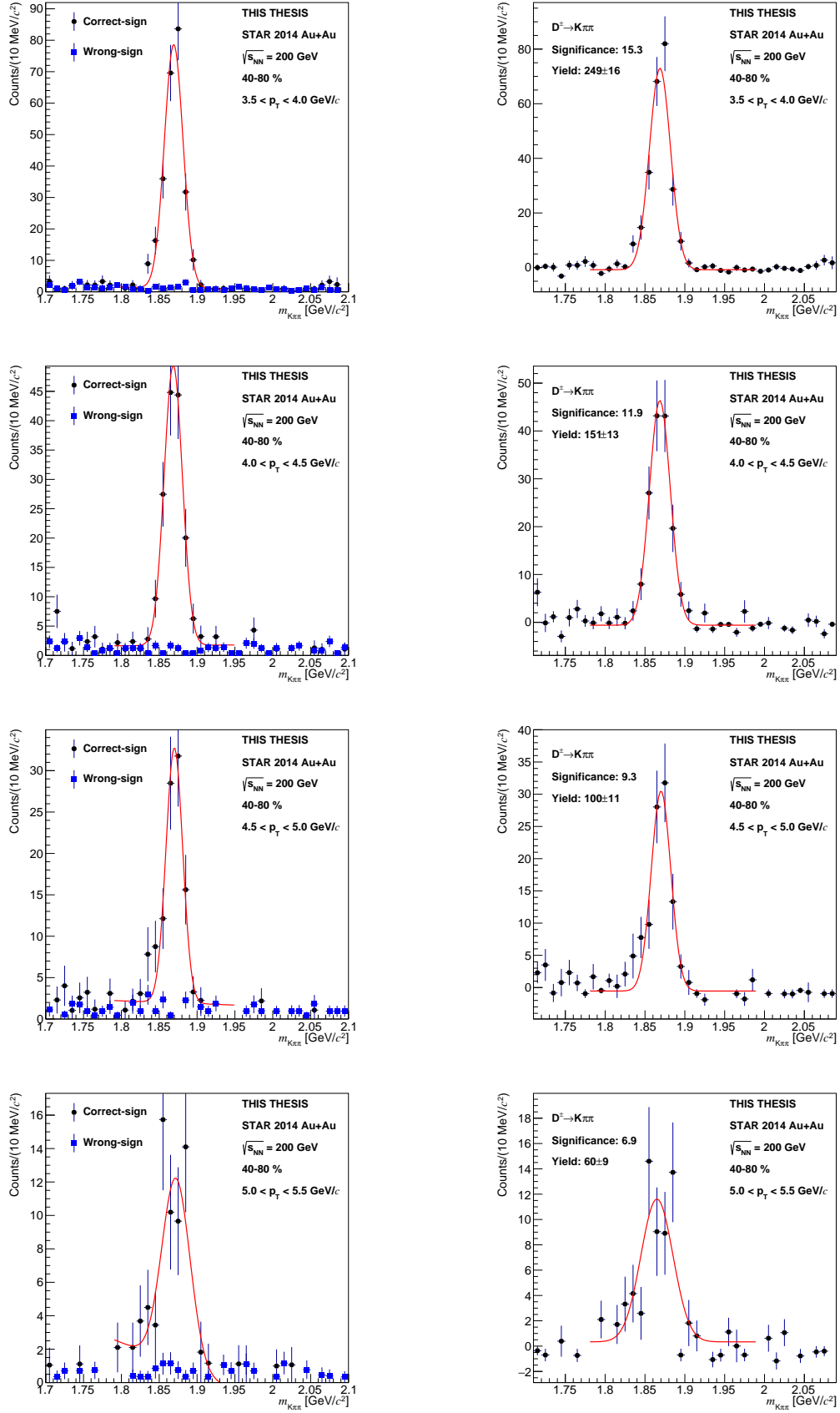


Figure B.11: Invariant mass distribution of  $K\pi\pi$  triplets before (left panel) and after (right panel) background subtraction for the 40-80 % centrality range and  $p_T$  bins: 3.5-4, 4-4.5, 4.5-5 and 5-5.5  $\text{GeV}/c$ .

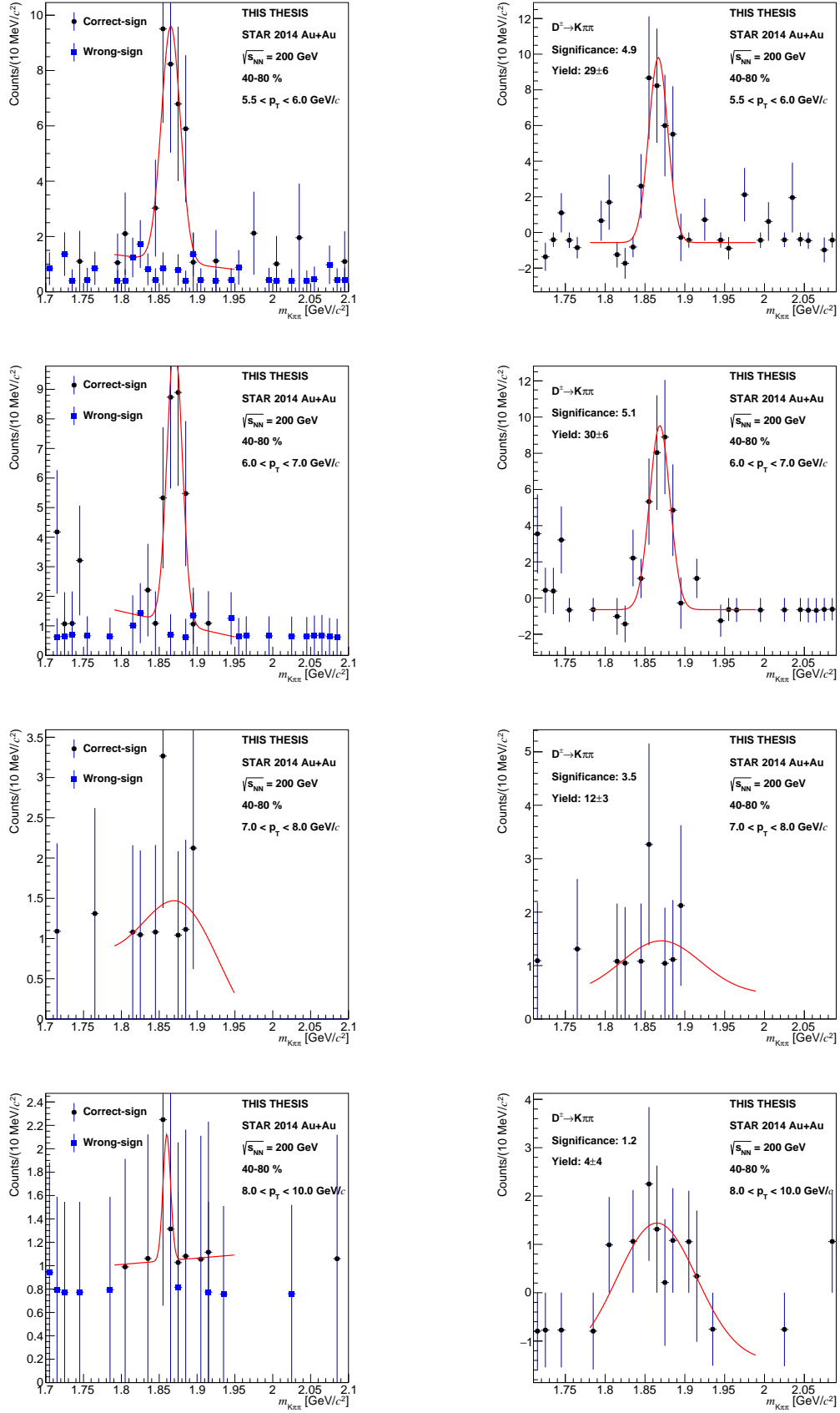


Figure B.12: Invariant mass distribution of  $K\pi\pi$  triplets before (left panel) and after (right panel) background subtraction for the 40-80 % centrality range and  $p_T$  bins: 5.5-6, 6-7, 7-8 and 8-10  $\text{GeV}/c$ .